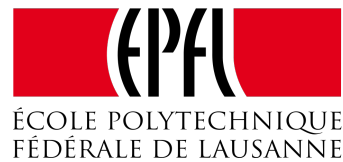




THE UNIVERSITY OF TOKYO



ÉCOLE POLYTECHNIQUE
FÉDÉRALE DE LAUSANNE

Haptic Feedback Controller Palm Pressurization by Series Elastic Actuators in a Handheld Device

Master Thesis

Author:

Roman OECHSLIN

Department:

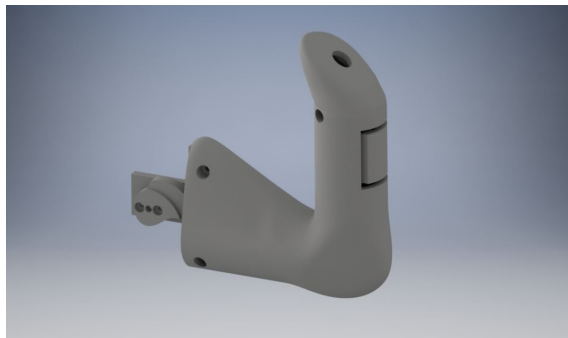
MICROENGINEERING

Director of project:

Prof. Hannes BLEULER

Supervising professor:

Prof. Akio YAMAMOTO



August 17, 2018

Haptic Feedback Controller – Palm Pressurization by Series Elastic Actuators in a Handheld Device

Roman Oechslin, Section Microtechnique

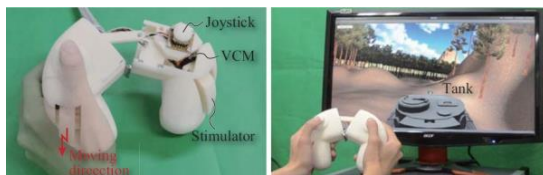
Assistant:

Professeurs: Bleuler Hannes et Yamamoto Akio

Ce projet est basé sur une recherche à l'université de Tokyo, proposant un appareil haptique, avec lequel l'utilisateur peut piloter un robot mobile. Ce contrôleur renvoie l'orientation d'un robot (2ddl) à l'utilisateur, permettant une perception intuitive de l'état du robot. La nouveauté de cette recherche est, que les forces du feedback haptique sont substituées par une pression dans les paumes.

Dans ce travail, le but était de remplacer les moteurs à bobines mobiles par des actionneurs élastiques séries (AES). Ceux-ci permettent d'augmenter considérablement la force finale. De plus, les éléments élastiques sont capables de stocker de l'énergie, ce qui résout le problème de dissipation d'énergie et de chauffage dans l'ancien design. Comme désavantage, la réaction de ces systèmes est très lente, dû aux éléments mécaniques.

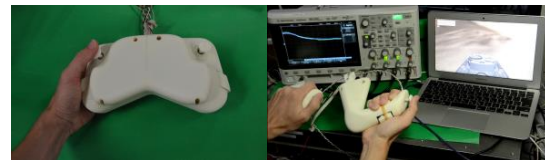
Dans cet œuvre deux nouvelles conceptions d'appareils portables ont été étudiées et testées, pour prouver la fonctionnalité des AES dans des applications haptiques.



Contrôleur proposé par [Nakamura, et al. 2016]

Le premier prototype a été inspiré par des contrôleurs conventionnels. Après avoir dessiné et imprimé ce prototype, les paramètres majeurs ont été identifiés, analysés et documentés. Ces paramètres étaient en effet la force maximale, la latence de la réponse mécanique par rapport à la

référence, la stabilité et la transparence. Basé sur ces résultats, un deuxième contrôleur inspiré par un manche de pilotage d'un avion a été conçu.



Les deux contrôleurs utilisant des AES

Les contrôleurs proposés ont été testés non seulement dans la simulation, mais aussi en utilisant un vrai robot. Pour faire cela, une application avec une interface graphique a été conçue. Elle traite les messages de communication entre le robot et l'ordinateur.

Les résultats ont confirmé, qu'en fonction de l'application, l'implémentation d'un système d'actionnement utilisant des éléments élastiques ne risque pas la transparence.

	Requis	Type 1	Type 2
Force [N]	>10	10.8	18
Latence [ms]	<160	50	90
Taille [mm ³]	<200x 150x 100	220x 110x70	155x 155x50
Poids [kg]	<0.6	0.55	0.5

Tableau de résultats

Pour soutenir ces résultats, un modèle mathématique a été créé. Celui-ci permet de simuler l'appareil et d'effectuer une recherche dans le domaine des paramètres.

Master Thesis - Summer 2018	
Title:	Haptic Feedback Controller - Palm Pressurization by Series Elastic Actuators in a Handheld Device
Candidate:	Roman Oechslin
Professor:	Hannes Bleuler
Supervisor:	Akio Yamamoto
Department:	Microengineering

Short Introduction

In 2016 a handheld haptic feedback controller has been designed at the University of Tokyo, which uses voice coil motors to actuate two stimulators. These stimulators create a pressure in the user's palms, which substitutes the kinesthetic sensation of forces. Using this controller, one can navigate a tank in a Unity based simulation. The feedback law was based on the roll and pitch angles, giving the user an intuitive feeling of the robot's orientation within the simulation. Even though the current application is the navigation of a mobile robot, the target application shall not be specified at this point, to ensure a certain flexibility.

The voice coil motors (VCMs) can only produce a low output force and create a lot of extra heat when maintaining a certain force. Therefore, a new research project aims at replacing this actuation system by a novel design based on the principle of series elastic actuators (SEAs). These SEAs have the advantage of high output forces and simple control.

Project Objectives and Requirements

In the scope of this project, several controllers implementing SEAs shall be designed, prototyped and tested. Important design-related parameters shall be identified and reported, such that the suggestions can be used as a guideline for future projects.

It is expected that the output force of the controller designs is bigger than 2N, the maximum of the VCMs. The control speed of the actuation system shall be fast enough to ensure a smooth and intuitive feeling, subjective to the user. The weight of the controller does not have to be optimized, but the new designs should not exceed 0.6kg, which is the weight of the previous device.

The controllers shall be tested in the virtual environment and on a real robot. This requires a certain controller modularity to be able to use it for any kind of robot controllable with 2 input-josticks. The size of this robot is not specified.

Abstract

This master thesis is based on Nakamura, et al.'s work [1] and further investigates the research in haptic feedback in handheld devices. The previous work has focused on providing a solution for limited information about a remotely controlled robot, for example in a search-and-rescue mission or a hazardous inspection site. The controller provided haptic feedback using palm pressurization as a pseudo-force to the operator. The force is proportional to the robot's orientation, such that the operator can intuitively feel obstacles, bumps or slopes as a pressure in the palms. The controller used voice coil motors which could only provide very low output forces. Furthermore, a constant current had to be delivered to maintain a target force. This resulted in high energy dissipation and heated up the system.

In this thesis, an alternative actuation system, based on series elastic actuators, has been studied. Several designs have been proposed and extensively tested. An underlying mathematical model has been created, which helped identifying friction and damping coefficient in the system. To complement the limited sources of literature in this field of study, design suggestions based on the parameter testing have been made.

The requirements of higher output forces (10N) with acceptable control speed (reaction time of 50ms) could successfully be met. The common haptics-related issues of stability and transparency could be overcome.

This work shows that, depending on the target application, an implementation of series elastic actuators can significantly increase the output force while not limiting the control speed or reaction time. This design can not only be used for remotely operated vehicles (robots and drones) but also handheld manufacturing tools or manipulation setups, where haptic feedback can immensely increase the performance.

Acknowledgements

This project would not have been feasible without the help of various people. At this point, I would like to speak out my gratitude towards them.

I would first like to thank my thesis supervisors Prof. Akio Yamamoto and Prof. Hannes Bleuler. I am thankful for the friendship between the two professors which has made it possible for me to gain this valuable experience in Japan.

The project supervision from Prof. Yamamoto and the constructive feedback and ideas that he has provided were particularly helpful. This project could only be realized thanks to the fruitful discussions with him and his inputs.

I would also like to thank Prof. Bleuler who has helped me before coming to Japan in matters of preparation and organization, as well as for his correspondence with the Ecole Polytechnique Federale de Lausanne.

I would also like to thank the secretary Mariko Kawamura who has helped immensely in all organizational affairs, such as filling out immigration and residence forms.

Lastly, I would like to thank all the members of the advanced mechatronics laboratory, who have taught me the language and cultural aspects. They have welcomed me warmly in their circle and even though this was an exchange program, I almost felt at home. Thank you.

Preface

Between February and August in 2018, I was given the chance to go on an exchange program to the University of Tokyo. Sent by Prof. Hannes Bleuler, I had the opportunity to join the advanced mechatronics laboratory led by Prof. Akio Yamamoto, to work on an applied haptics project. The University of Tokyo provided a language course throughout the semester, to facilitate the cultural exchange and living in Japan. I was very happy to have come here, not only to learn about the culture, traditions and habits in Japan, but also to gain valuable experience in my domain of expertise.

I first started reading into the previous project and current literature in this field of study. Then a thorough brainstorming session about device designs was followed by the actual 3D-design and 3D-printing phase. With extensive testing I could improve the design and analyze the important parameters.

Then I wrote a small software in Processing to handle the messages and communicate with the robot. Furthermore, the Arduino had to be programmed to read out the input commands and handle data. To finalize the connections, I had to design and solder small circuits and implement electric filters.

A thorough frequency response analysis was conducted for two different devices and their results have been used to create a mathematical model. The data has been analyzed and represented writing python scripts. The mathematical model could be used to simulate the setup and identify parameters in Simulink.

On the control part, a PID control structure was implemented and their gains have been fine-tuned to meet the performance requirements. Then the devices have been put to a test with a real robot, as well as a simulated environment. The performance has been evaluated and reported in this thesis.

For future research, a brief section of suggestions has been written, which can be used as a guideline for similar projects.

A major challenge was the fact that the robot's user manual and documentation was written in Japanese. Hardware-related issues were mainly encountered with the robot's battery that had to be removed and an alternative power supply had to be used.

In this project I gained valuable experience in all aspects of robotics. Working individually and autonomously, I could improve my practical skills and technical knowledge. Furthermore, the organized lab-internal presentation meetings helped me in presenting my work to a group of fellow researchers and communicate encountered problems. All in all, I had a lot of fun with an interesting project and great laboratory students, creating a healthy work environment, while at the same time, discovering a wonderful country.

Contents

1	Introduction	1
1.1	Haptics	1
1.2	Major Issues in Haptics	1
1.3	Project Description and Status Quo of Previous Projects	2
1.4	Target Application	3
1.5	Psychological Aspects	3
1.6	Project Outline	4
1.7	Performance Requirements	4
1.8	Approach and Expected Challenges	5
1.9	Literature Review	5
1.10	Thesis Delineate	7
2	Design Phase of the First Controller	8
2.1	Principle of Series Elastic Actuators (SEA)	8
2.2	Discarded Designs	8
2.2.1	Car-Jack	8
2.2.2	Linear Actuator	9
2.2.3	Toothed Bar	9
2.2.4	Wedge	9
2.2.5	Hydraulic or Pneumatic	10
2.3	Accepted Designs	10
2.3.1	Centric Shaft	10
2.3.2	Cam-follower with Eccentric Shaft	11
2.4	Inspiration of the Design	11
2.5	Implementation	11
2.6	Design and Prototyping	11
2.7	Electrical Components	12
2.7.1	Motors	13
2.7.2	Joysticks	13
2.7.3	Photoreceptors	13
2.8	Mechanical Components	15
2.8.1	Springs	15
2.8.2	Linear Guideway	15
2.8.3	Coupling	15
2.8.4	Clamp Link	16
2.9	Printed Version	16
3	Mathematical Model of the Game Controller	17
3.1	Assumptions	17
3.2	Spring Constant and Damping Coefficient of the Operator's Hands	18
3.3	Identification of the Spring Damping Coefficient	18
3.4	Expected Transfer Functions	18
3.4.1	PID Transfer Function	18
3.4.2	Motor Equations	19
3.5	Analytical Inertia Identification	19
3.6	Experimental Inertia Identification	20
3.7	Relating ΔX to θ	20
3.7.1	Motor and Spring Transfer Function	20
3.8	Main Equations for Analytical Transfer Function	20
3.9	Analytical Results	21
3.9.1	Comparison of Results - P-Controller and Experimental Data	22

3.9.2 Comparison of Results - PID-Controller and Experimental Data	22
3.10 Analytical PID Gain Domain Study	24
4 Robot and Environment	27
4.1 About the Robot	27
4.2 Hardware Setup	28
4.3 GUI in Processing	28
4.3.1 Message Handling	28
4.4 Control Scheme	29
4.5 Electrical low-pass Filter	30
4.6 Amplifiers	30
4.7 Feedback Laws	30
5 Testing of the Game Controller	31
5.1 Frequency Response Function	31
5.2 Test Setup	31
5.3 Control Scheme	31
5.4 Tracking Behavior of the P-Controller	31
5.5 Step Response	32
5.6 Sine Tracking	32
5.7 Sine Wave Fitting	33
5.8 Bode Diagram	33
5.9 Discussion of the P-Tracking	34
5.10 Motor Comparison	36
5.11 Experimental PID Tuning	37
5.12 Tracking Behavior of the PID-Controller	37
5.13 Discussion of the PID-Tracking	37
5.14 Performance Evaluation	39
5.14.1 Latency	39
5.14.2 Transparency and Intuitiveness	41
5.14.3 Stability	41
5.14.4 General Performance	41
5.15 Unity Simulation	42
5.15.1 Latency	43
5.15.2 Unity Performance Evaluation	43
5.16 Overall Evaluation of the Game Controller	45
6 Design Suggestions	46
6.1 Software and Control Choices	46
6.2 Mechanical Parameters	46
6.3 Electrical Parameters	47
7 Design Phase of the Yoke Controller	48
7.1 Working Principle	48
7.2 Design and Parameters	48
7.3 Printed Version	49
8 Testing of the Yoke Controller	52
8.1 Test Setup	52
8.2 Tracking Behavior of the P-Controller	52
8.3 Bode Diagram	52
8.4 Discussion of P-Tracking	54
8.5 Hysteresis Effect	55

8.6	Other Non-Linearities	56
8.7	Motor Choice	57
8.8	Performance Evaluation	57
8.8.1	Latency	57
8.8.2	Transparency and Intuitiveness	58
8.8.3	Stability	58
8.8.4	General Performance	58
8.9	Unity Simulation	59
8.9.1	Latency	59
8.9.2	C-Clamp-Blocked Unity Test	60
8.9.3	Unity Performance Evaluation	60
8.10	Overall Evaluation of the Yoke Controller	61
9	Discussion	62
9.1	Game Controller	62
9.2	Theoretical Model	62
9.3	Yoke Controller	62
9.4	Identified Potential and Applications	63
10	Conclusion	64

1 Introduction

1.1 Haptics

The Oxford Dictionaries define haptics as

”Relating to the sense of touch, in particular relating to the perception and manipulation of objects using the senses of touch and proprioception.” [2]

It dates the term back to the late 19th century and states its origin from the Greek words *haptikos* meaning ’able to touch or grasp’ and *haptein*, ’fasten’.

In engineering, the research in the haptic field has started to emerge in late nineteen-eighties [3]. With Thomson Reuters’ *Web of Science*¹, one can find the number of papers published, containing the keywords ’*haptic feedback*’. The graph can be seen in figure 2 and clearly shows the increase in popularity of this research topic.

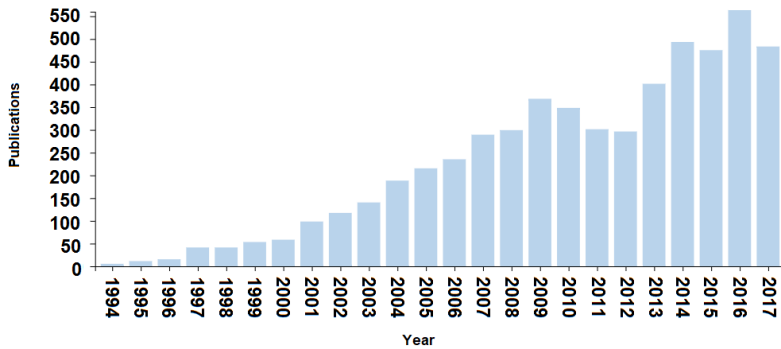


Figure 2: Trend of published papers containing the keywords ’*haptic feedback*’.

Before that, man-machine interaction was mainly limited to keyboard and mouse input, which is rather unidirectional and passive and it soon has become clear that this requires a rather skilled user for all kinds of operations. This directly leads to limitations in performance. Haptics can extend this unilateral interaction by providing tactile or kinesthetic information. This combination can overcome the user’s limitations and improve performances of high-precision tasks or high-force tasks drastically.

In [4] it is stated that, even though the research in the haptic domain has significantly increased in the past ten years, further investigations are necessary for the ”quest for realism”, especially in medical telesurgery applications where realism is key to performance. Other application domains include but are not limited to space operations, manufacturing, physical rehabilitation, arts or simply entertainment related devices.

The critical elements for stability of haptic setups, mainly focusing on haptic simulations are discussed in [5]. It also motivates exploration of alternative control techniques due to the unpredictability of the human operator and the environment model.

1.2 Major Issues in Haptics

In general, the issues in haptic devices are related to the stability and the transparency. On one hand, high transparency is desired, on the other hand however, this can only be achieved by jeopardizing the system’s stability[6].

In literature ([7], [8], [9]) the importance of stability and transparency is often emphasized, stating

¹accessed (2018, July 26th), https://apps.webofknowledge.com/WOS_GeneralSearch_input.do?product=WOS&search_mode=GeneralSearch&SID=C3bYefMpEMD84LZwaAU&preferencesSaved=

that they are the main problems related to haptics and haptic teleoperation applications. For conventional master slave operation systems Salcudean explains transparency as

[...] the master should feel to the operator as if the task were being manipulated directly.[7]

Even though the controller does not meet the definition of a conventional master-slave teleoperation setup, the problem settings of stability and transparency still apply. Often, the stability issues arise from master-slave mass mismatch and stiffness of the environment. Furthermore, high inertia poses problems for higher frequencies. In this research however, the masses and frequencies are relatively low.

The stability of the controller designed in this work is not only affected by the control scheme and the mechanical setup, but also by the operator, whose grasp can render a system stable or unstable [9]. Additionally, communication delays can also cause instability.

Another common issue in haptic applications is the fact that counteracting forces are created. In conventional designs, these forces are dealt with, by using grounded devices. If the device is handheld however, the counteracting forces will also affect the user and their effects need to be taken into consideration.

The previous research aimed at developing a new design of haptic feedback systems that can overcome these issues. In the handheld device, the reaction forces are transmitted to the user. However, the research group has presented a method to deal with those reaction forces, such that the operator's perception of the target forces is not distorted. Furthermore, the problem of stability is overcome by decoupling the input and output elements, which yields a stable open-loop system. A detailed explanation of the previous research is given in the following paragraph.

1.3 Project Description and Status Quo of Previous Projects

Research on a handheld controller has been conducted at Yamamoto's lab in 2016 and 2017 ([1], [10], [11]). This controller is capable of giving a feedback to the user about the state of a remote-controlled robot. As stated in the papers, the feedback law is based on the roll and pitch angle of the robot. Therefore, the operator intuitively feels the orientation of the robot. For the feedback two voice coil motors (VCMs) have been used. As shown in figure 3, the stimulators are the movable parts in contact with the palms, controlled by the VCMs. The disadvantage of the voice coil motors is that a constant current has to be applied to maintain a constant output force. This leads to an energy-inefficient system and produces a lot of extra heat. Furthermore, the motors were rated at 13.6V with 2N/A. The output force of each palm stimulator was exactly 2N. Due to the magnets in the VCMs the controller was rather heavy, which could fatigue the operator if used for too long.

The advantage of these motors however, was the speed at which they were able to feed the force back to the operator. Due to the fact that the output force of the voice coil motors depends on the current, the speed of this system is governed by the amplifiers that convert the reference voltage to a target current.

The testing environment for this controller consisted in a Unity program that let the user control a tank with crawlers in an artificial landscape. When driving over the hills and smaller bumps, the user feels the magnitude of the tilt (roll and pitch orientation angles) as a pressure in the palms. It has already been shown in the previous work that this pressure successfully substitutes the force and is perceived as a pseudo-force.

In figure 3 one can see the final controller and its testing environment. The joysticks are used for navigation. In this case, the tank's crawlers can be controlled individually in both directions and the speed is linear to the joystick's position. The simulation renders the robot in a hilly environment, including reaction and gravitation forces. From the orientation (pitch and roll) the desired feedback

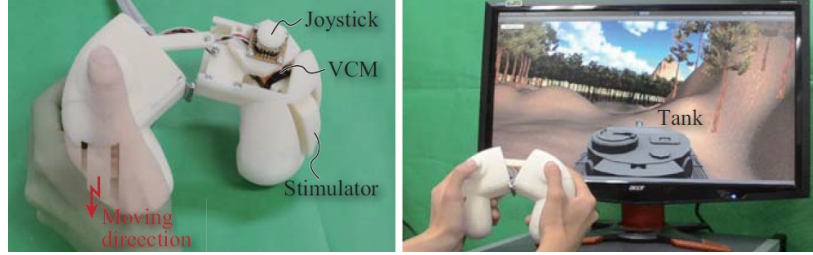


Figure 3: Developed controller in previous research[11].

(the forces that should be felt by the operator) are calculated and sent to the controller. The law is such that if one is driving over an obstacle on the right-hand side, one can feel a higher force on that side.

The feedback is read out by an Arduino (not shown in the figure) and controls the voice coil motors with the help of an amplifier (not shown in the figure). These motors will move the stimulator back and forth, in a uni-lateral direction. This direction can be fine-adjusted by the hinge in the middle of the controller. The stimulators are in direct contact with the operator, creating a pressure in the palms. They are henceforth also referred to as the palm pads.

1.4 Target Application

The Fukushima Daiichi nuclear disaster in 2011 was a shock for the whole world. Even 7 years after the incident, the radioactive environment still leaves a wide area inaccessible. However, an on-site inspection can give important information for all kinds of research fields. These inspections have to happen using remotely controlled robots.

A common feature is to provide a visual feedback with an on-board camera, as it is used in the Inachus project², for example. However, in earthquake affected areas, the view can be obstructed due to smoke, dust and rubble[12].

Consequently, the feedback controller designed in this lab can be used for facilitating navigation in such environments. The intuitive and straightforward feedback method yields higher performance with no trade-off.

1.5 Psychological Aspects

The device that has been developed in the previous research[11] feeds back a force to the user. However, according to Newton's third law, every action force induces an equal reaction force. This means that the user should feel a pushing force on the palms, directed towards the user, as well as a pulling force on the fingers, away from the user. This effect can be seen in figure 4. The research with this device has shown however, that this reaction force is felt much less by the user due to the non-linear force sensation characteristics of humans.

Due to the fact that the reaction force is spread over the whole area of the fingers in contact with the controller, the pressure is much lower, even though the magnitude of the forces stay the same. This means that the user only believes to perceive a pushing force, which allows to give a more intuitive experience. Thus, the ubiquitous problem in all haptic applications of dealing with the reaction forces can be overcome. Therefore, the device does not have to be grounded in order to dissipate the reaction force, but can be used as a handheld device.

²accessed (2018, August 8th), <https://www.inachus.eu/>

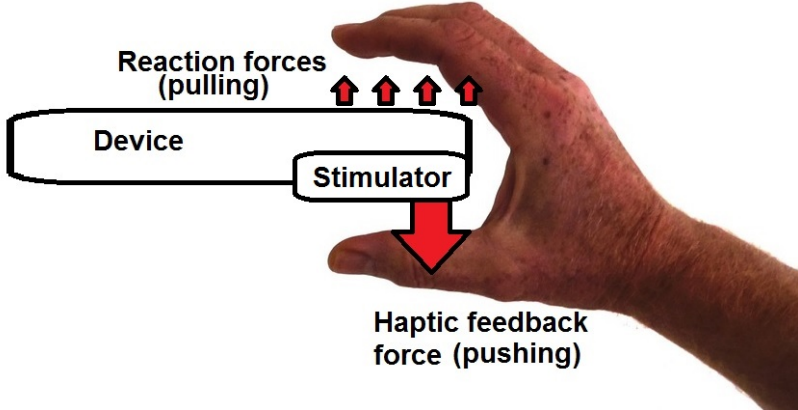


Figure 4: Target feedback force and reaction force indicated in user's palm.

1.6 Project Outline

In order to overcome the weaknesses and disadvantages of the voice coil motors, a novel actuation system shall be investigated. In the scope of this project, several haptic feedback controllers shall be designed, implementing series elastic actuators (SEAs). These controllers shall be prototyped and tested in the Unity simulation, as well as on a real robot. The tests of the controller shall be made on the commercially available crawler robot developed by Topy³ using two tracks as means of transportation. In addition, different springs and spring arrangements shall be analyzed.

The performance of the controller is expected to have a higher output force than the one from the previous research, which implemented voice coil motors. It is namely 2N per palm pad. It shall be shown, whether or not the series elastic actuation principle is the bottleneck of its implementation in terms of control speed and therefore transparency and real-feel.

The controller shall be capable of providing intuitive feedback (defined in section 1.9) to the user. The weight does not have to be optimized, but it shall not exceed the weight of the current controller (ie. 0.6kg).

From the results a design parameter guidance in form of suggestions shall be written, that future research can use as a reference and guideline.

The given time for this project was from February until August 2018, a total of 25 weeks.

1.7 Performance Requirements

Here, the performance requirements from the previous paragraph are summed up and a rough reference value is calculated. It seemed reasonable to have an output force of 10N, a value five times higher than in the VCM-based controller. This corresponds roughly to 1kg against gravity.

The control delay was based on the research of [13], which suggested a maximum arm movement frequency of 6Hz. With the target application of an inspection robot in mind, the low operating speed justifies the comparably small delay time.

The maximum size of the controller has been calculated as 110% of the size of the controller from the previous research.

A quantitative requirement on transparency cannot be given at this point, however an intuitive feeling related to the transparency is expected. Furthermore, the stability of the controller has to be guaranteed.

³accessed (2018, May 25th), <http://www.topy.co.jp>

Designator	Value	Unit
Output force	10	[N]
Control speed	no requirement	[full stroke/s]
Response delay	160	[ms]
Maximum size	200 × 150 × 100	[mm × mm × mm]
Maximum weight	0.6	[kg]

Table 1: Performance requirements of the controller.

1.8 Approach and Expected Challenges

As an initial approach and to be consistent with the previous research in this area [1], the robot's orientation (pitch and roll angles) have been taken as state of interest and are fed back to a handheld controlling device. As an alternative measure, the current in the two crawler motors can be fed back to the user, to have a rough idea of the used energy. With feedback on the current consumption it is also detectable if the robot is stuck or being blocked somewhere.

Note at this point, that in this work *feedback* is referring to the force that is determined by the robot's state and created by the controller, acting on the operator. The term feedback is generally avoided when talking about the closing of the control loop that is necessary to achieve or maintain the aforementioned force or control variable, for that matter.

Current literature and research projects show little to no guidance on how to build an SEA-based haptic feedback device. Furthermore, the human hand acting as environment, has uncertain mechanical parameters. Due to this, the design of the controller and the implementation of the SEA system tend to be rather iterative processes. Furthermore, the design of the previous controller cannot be recycled, since the actuation system differs completely.

In addition to that, a lot of parameters are present in the controller. These include but are not limited to the mechanical parameters, such as the springs and spring constants, the motors, feedback direction and the software and electrical parameters, such as filters, control scheme and control frequency.

The performance evaluation of such a controller can be manifold. Depending on the target application, one might favor low-latency and fast feedback over high output force, or vice versa. Therefore, it is important to keep the performance specifications of the target application in mind when deciding on design of the controller and when evaluating. Concerning the stability issues (detailed explanation in section 1.2), it is not always possible to fully classify a given controller and setup into stable and non-stable, since it might also depend on the user's perception and handling. However, it can generally be assumed that the proposed controllers are stable due to the open-loop between input and output. If one assumes that the environment behaves predictable, then the joysticks can seen as completely decoupled from the stimulators.

Finally, an assessment of the intuitiveness and transparency can only be done subjectively.

1.9 Literature Review

The major applications for haptic feedback devices can be found in (minimally invasive) surgical tele-operated medical systems ([9], [14], [15], [16]), mobile augmented reality ([17], [18]) and teleoperated robotic systems (for example in space) [8]. However this research project focuses on implementing a feedback on a handheld controller for a non-specified group of grounded wheeled robots. The controller uses pressurization feedback as a substitution for force feedback to give an intuitive feeling about the intrinsic state of the robot. In [19], intuitiveness is said to be achieved when the user immediately knows what the system's intentions are.

The medical domain with its minimal invasive surgery (MIS) and teleoperated system with haptic feedback is a common research field. The research group in [9] states, that the absence of haptic feedback is the reason that impedes further spread of surgical robots. They give a broad overview of

current research in this field, focusing not only on different haptic feedback methods and interface types, but also on control schemes and the device types.

The aspects of minimal invasive surgery are also explained in [14]. Furthermore, it proposes the design of the master and slave in such a teleoperated setup. It uses force feedback and is dealing with a high degree of freedom (ie. $DOF = 5$). The device is a handheld pen that is connected to a robotic operator, which can change the pen's orientation.

Research on haptic feedback in handheld devices has been conducted not only with force feedback ([20], [21]), but also with pressure stimulation ([10], [11]), [22] or vibrotactile feedback ([22], [23]). [20] investigated the substitution of kinesthetic and cutaneous force feedback by cutaneous feedback only. They used a wearable finger stretching device for the task of needle insertion. In [21] however, a vibrotactile force feedback system was designed and evaluated. Its application domain is in minimal invasive surgery (MIS), where feedback can facilitate surgical operations. The output device sends vibration signals to the operator's foot.

A custom-made pressure cuff was designed in [22] that could give feedback when manipulating an object with a prosthetic hand. Again, the feedback device is decoupled from the main interaction device which can be seen as a disadvantage. In addition to the pressure feedback, the SoftHand uses vibrotactile feedback to inform the user about the surface properties.

In the work of [23], the research group mainly focused on having an intuitive feedback in a game controller for a flight simulator. The intentions were to be low-cost and versatile. The vibrotactile feedback is coming from the controller itself, which should make the users feel as if they have become the aircraft itself. The device is called the haptic glove, again in the domain of wearable haptics. An evaluation and usability study of this device has not been conducted.

In [24] a wearable haptic display is proposed, using the principle of deforming and stretching the fingers' skin. It can generate vertical and shearing stress to the finger to give the impression of holding an object with a certain mass and to give perception of a pseudo grip force.

In the domain of series elastic actuators, [25] suggests using an elastic element in a conventional actuation system. It states its advantages for robots performing natural tasks and presents a control system for force or impedance control. Among the advantages are the low-pass filtering of shock loads, facilitation of force control, the increased achievability of stability and possibility of energy storage.

The principle of SEA is integrated in a legged robot and explained in [26]. The paper suggests to implement this actuation system in cases where little is known about the environment, such as with legged robotic walking, wearable exoskeletons and also haptic interfaces. Then it introduces other research projects where series elastic actuators have enabled legged robots to walk.

In the research of [27], an electric series actuator is compared with a hydraulic SEA. The target application is a four-legged walking robot. The paper also provides a detailed analysis of the dynamics of the actuator, taking into account the motor parameters as well as the mechanical setup. The results are purely theoretical, where different frequency responses are compared. It shows a cut-off frequency around 30Hz for the investigated actuation design.

A variant of the SEA is the rotary elastic actuator. The impedance control of such an actuator is discussed in [28]. Again, the frequency response function has been used for performance analysis.

The joint topics of haptics that implement the series elastic actuators show only little research. For one, there is the implementation of SEA in a laparoscopic haptic device from [29]. The device has 4 degrees of freedom. In the frequency response analysis both, the experimental and analytical data show a force bandwidth of around 12Hz. They considered damping coefficients up to 1Ns/m for the springs.

In the work of [30], they address the control challenges of a rehabilitation robot based on SEAs. The conditions guaranteeing stability and passivity of such a haptic device are investigated in their paper. The analysis is applied to parallel robot structures with added elastic elements.

In [31] an educational SEA based robot (a haptic paddle) is studied, for understanding human robot interaction under specific conditions. It is used to teach students about closed-loop force control. The paper shows the dynamic model of the setup and analyzes it. The cut-off frequency is around 12Hz.

From this literature review it can be seen that a lot of research has been done for haptic minimal invasive surgery devices. Also, the domain of wearable haptics seems to be very popular. However, research in handheld haptic feedback devices where the device itself is producing the feedback are more scarce. Even more so, when the feedback method is a pressure based force substitution. Coupled with the implementation of the series elastic actuators, this work becomes a novelty in both research fields combined.

1.10 Thesis Delineate

This thesis sums up and represents the methods and results of the work during one semester. The thesis' structure is kept in chronological order, where it makes sense. Due to the high innovation factor of the research and the fact that there is only little research from literature that can be used as base knowledge, the work turned out to be very practice oriented and iterative. For this reason, the first controller prototype was built and analyzed before a mathematical model could be created. Chapter 2 explains the working principle of SEAs and the general design phase of the first controller. Discarded and elected controller designs are introduced. Electrical and mechanical components of vital importance are explained.

Following this design introduction, and to keep this thesis' structure consistent with general research papers, the mathematical model is presented. The mathematical analysis has mainly been applied to the first controller but can be extended to be used as a tool for identification of general controller design parameters. This chapter shows the equations of motion that have been used to create the model and show the implementation in Simulink for the analytical results. For reasons of completeness and simplicity, the experimental results of the first controller are also shown in the same chapter.

Chapter 4 introduces the robot that has been used for testing and explains the environment for the test setups.

The next chapter talks about how the controller has been tested and depicts the performance. It explains major decisions that influenced the design of the second controller and discusses the results to some extent.

Chapter 6 is discussing design suggestions, based on the results of the design and testing of the first controller. The results of the second controller have also been considered, albeit to a smaller degree. The next two chapters (7 and 8) discuss the design phase and testing of the second controller, respectively. The design choices are based on the findings of the performance about the first controller. The testing was conducted in the same manner as with the first controller for the sake of direct comparison.

The discussion of the project and all results can be found in chapter 9, and a final conclusion is given in chapter 10.

2 Design Phase of the First Controller

2.1 Principle of Series Elastic Actuators (SEA)

The principle of series elastic actuators is relatively simple. The concept is explained in [25] which also mentions a more accurate and stable force control and the possibility of energy storage. An SEA is a normal actuation setup with an integrated elastic element. For this purpose, a simple spring or a set of springs can be used. As it can be seen in figure 5 the control scheme is reduced to a simple distance-based control, while the output remains an equivalent force, given by Hooke's law.

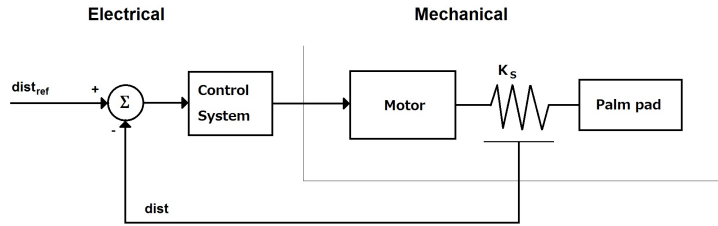


Figure 5: Control scheme for the haptic feedback system.

An additional advantage is, that the elastic element is shock-absorbent and stable for different environments. This means that the controller can be stable even when used with different grip stiffnesses.

A thorough study of an SEA design and its analysis has been made in [27], stating that the most important parameter in the system is the spring constant. Therefore, springs with several different spring constants have been used for the analysis of this research project.

2.2 Discarded Designs

Before the first controller could be designed, a suitable implementation of this actuation system had to be thought of. The principle is based on transforming a rotary motion from the DC motor to a linear motion of the stimulators. This shall be done in a compact fashion to keep the controller's size minimal. For this purpose, a brainstorming for actuation methods has been done. Then the individual design suggestions were analyzed and carefully evaluated, with minor calculations for speed and output force. The discarded designs can be seen in the following sections.

2.2.1 Car-Jack

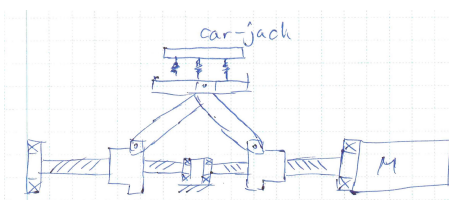


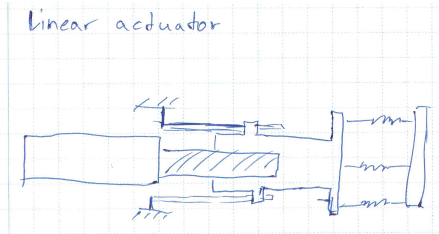
Figure 6: Discarded idea: Car-jack.

In the lab there was a controller from a previous project that used the screw nut actuation principle.

The previous work has shown that using voice coil motors, this shape for a handheld controller is appropriate, albeit with a low output force. The continuation of that project was that the VCMs have been replaced by an SEA system. The results showed that the controller was too slow to provide an intuitive feedback, due to the small pitch of the screw.

Even though it has been proven to work, due to its large size and slow response, this idea has been discarded.

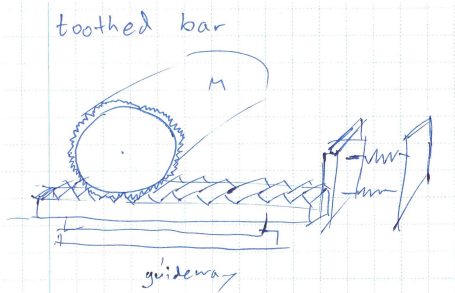
2.2.2 Linear Actuator



This is a rather straightforward approach that uses the same principle as a bench vice. The advantage is its simplicity. However, this system might turn out to be too large, especially if one considers a perpendicular feedback force towards the user.

Figure 7: Discarded idea: Linear actuator.

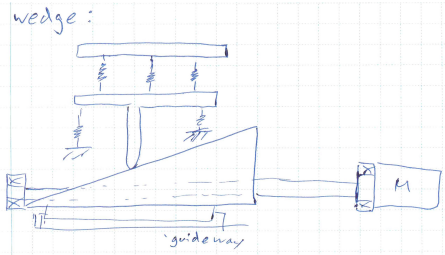
2.2.3 Toothed Bar



Here the principle is a rack and pinion approach where the rack is seen as a carriage in a guideway. The advantages are the orthogonal actuation, that can solve eventual space issues. Furthermore, the speed can be adjusted easily by choosing a different set of rack and pinion up to the point, where only few rotations are needed for the full desired stroke. The disadvantage is the eventual pre-load that is needed.

Figure 8: Discarded idea: Toothed bar.

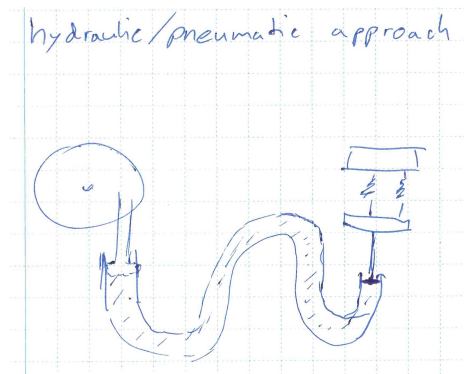
2.2.4 Wedge



The wedge system is similar to a cam-follower. Here the carriage is a wedge that simply pushes the palm pad out of its way. On the downside, there is a lot of friction involved and a pre-load is required. Even though the angle of the wedge varies the speed of the system, the achievable stroke was calculated to be too small. Furthermore, a guideway for the wedge and a guiding system for the actuated element would have been needed.

Figure 9: Discarded idea: Wedge.

2.2.5 Hydraulic or Pneumatic



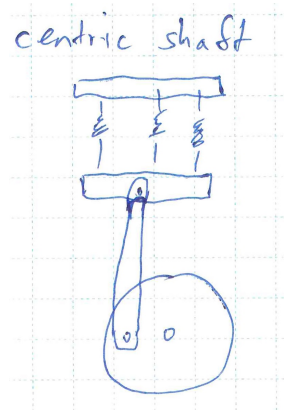
This idea was mainly for completeness of the suggestions. The disadvantages are the difficulty in control and the hassle of handling the hydraulic or pneumatic issues. Even though it can be implemented in practically any volume and shape, it seemed too difficult to further investigate.

Figure 10: Discarded idea: Hydraulic or pneumatic.

2.3 Accepted Designs

After some calculations and evaluation of the proposed designs, the following designs have been opted for.

2.3.1 Centric Shaft

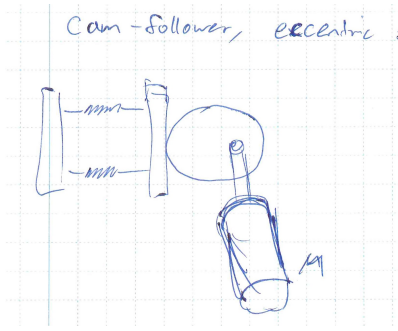


In this design, the motor is attached to a rotary disc or rotary lever, that pushes a carriage in its guideway (not depicted). This solution seemed relatively easy, even if it involves an element that corrects the parasitic movements.

The motor can be assembled orthogonal to the feedback direction, which can be advantageous for solving space issues. The speed and output force can be varied easily by changing the length of the lever. Due to the singularities in the system, the motor shaft has to turn less than 180° . With this, the whole system can be considerably fast.

Figure 11: Accepted idea: Centric shaft.

2.3.2 Cam-follower with Eccentric Shaft



This design is based on a conventional cam-follower principle, but with an eccentric shaft. The main disadvantages of this implementation is the high friction involved and the required torque being rather high. Since the motors have already been chosen, there was no margin on that aspect. The advantages are however, that only very small movements are necessary and the system would be rather fast. The space occupation and volume of this system was to be further investigated.

Figure 12: Accepted idea: Cam follower with eccentric shaft.

2.4 Inspiration of the Design

It is not far-fetched to search for inspiration in the domain of entertainment, if a user-friendly handheld controller is needed. The probably most famous controller is the one designed by PlayStation⁴, which can be used for a variety of applications. Due to this flexibility and the simple but elegant design, this work has opted for a similar design and used the PlayStation controller, as well as the design of the previous research as models. From now on, this controller design will be referred to as the game controller.

2.5 Implementation

After evaluating these designs, the centric shaft design has been tackled at first. It was designed as a clamp link based linear guideway controller (see figure 13), since it seemed to fit best into the casing designs from the previous work. Also, the calculated force of 14N was promising. The singularities in the design restrict the movement of the clamp link to 90° and it was furthermore calculated, that the maximum stroke could be achieved within 100ms.

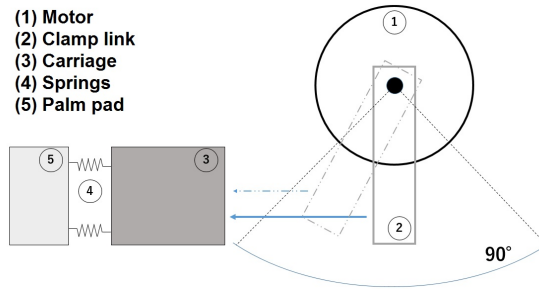


Figure 13: Initial schematic of the actuation design.

2.6 Design and Prototyping

The 3D design of the PS controller can be seen in figure 14.

This design of the controller aims at having a natural position for the hands, such that the user can hold the controller for a long time without having the hands in an awkward position. The palm

⁴accessed (2018, July 23rd), <https://www.playstation.com/en-us/>

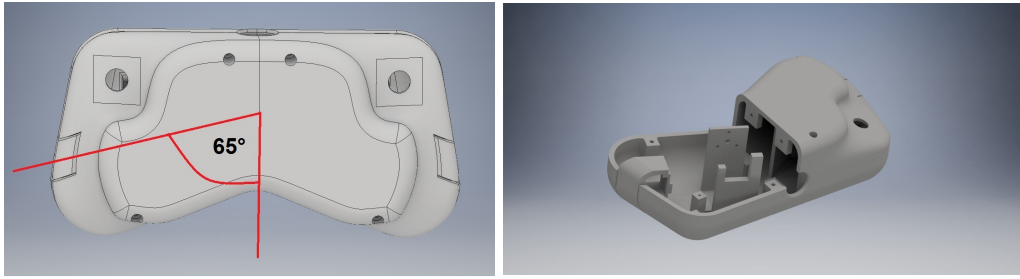
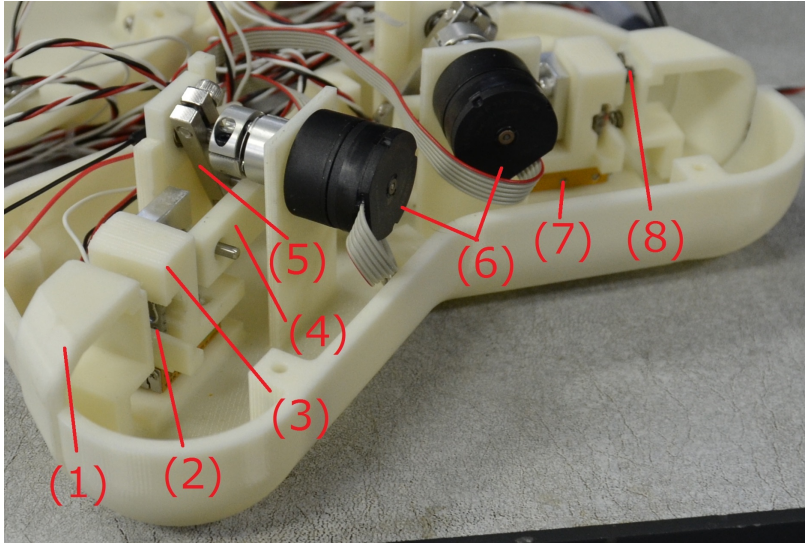


Figure 14: 3D model and rendering of the game controller.

pads that transmit the feedback pressure to the palms are not directed perpendicularly towards the user, but rather outwards at a certain angle (refer to figure 14). This can be seen as a drawback, since the user is expected to have the most intuitive feeling with a feedback opposing the driving direction (ie. perpendicular).

The dimensions of the controller are 220mm in length, 110mm in width and 70mm in height. The controller is unusually thick due to the feedback actuation design. The assembled actuation system can be seen in figure 15. The motor shaft is rotating a clamp link which is attached to a 3D-printed part, called connecting link. This 3D-printed part is attached to the carriage, also a 3D-printed part called L-plate, and is screwed to the linear guideway. The L-plate is connected via a set of springs (different spring constants have been tested) to the palm pad, thus making it an SEA. The linear guideway keeps the palm pad in a linear motion. The input joysticks' for navigation are not shown in the figure.



- (1) : Palm pad
- (2) : Photoreceptor
- (3) : L-plate
- (4) : Connecting link
- (5) : Clamp link
- (6) : Motors
- (7) : Linear guideway
- (8) : Springs

Figure 15: Actuation system with legend (and top cover removed).

2.7 Electrical Components

To have a functional controller, several requirements had to be met. First of all, an actuator was necessary to provide the feedback. In addition to that, the user shall be able to navigate the robot, which has been realized with potentiometer-based joysticks. To close the loop and create the desired force output, it was furthermore necessary to measure the compression of the springs. This has been

realized with a simple photoreceptor as a distance sensor.

2.7.1 Motors

The motors play an important role on the output force of the controller, as well as the achievable control speed. There were motors with two different reduction gear ratios available in the laboratory. They stem from Faulhaber's series called **2619 024 SR IE2-16** and their reduction ratios were 33:1 and 112:1. The maximum intermittent output torques are 100mNm and 180mNm respectively. Due to the reduction stages, the efficiency is around 60%. The maximum applicable voltage is of 24V, for motor protection however, the motor voltage has been limited to 20V during normal operation.

2.7.2 Joysticks

The joysticks are conventional 2-axes potentiometers. The series number is **P-04048** and they have been bought at Akizukidensi store. In the implementation of these sensors, a dead-zone has been created, such that the joystick value is converted to a zero-speed command, even if it is not exactly in the middle position. This can be seen in figure 16.

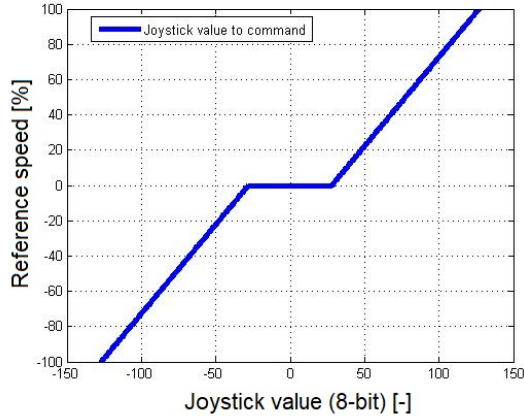


Figure 16: Joystick to command conversion with indicated dead-zone.

2.7.3 Photoreceptors

The photoreceptors are the **TPR-105** from *GENIXTEK CORP*. The circuit can be seen in figure 17. The components chosen are $R_1 = 330\Omega$ and $R_2 = 27k\Omega$.

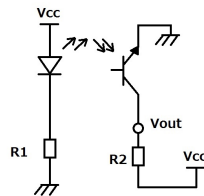


Figure 17: Photoreceptor circuit.

The photoreceptors' working principle is based on detecting the amount of reflected light. This controls the base current i_B of the transistor in the schematic. This base current then determines

the collector current i_C . Specific to this setup, the distance (and therefore the output force) controls the amount of light that is reflected on the wall of the palm pad. Therefore, we have:

$$F_{output} = k_{eq}\Delta x \propto i_B \quad (1)$$

$$i_C = h_{FE}i_B \quad (2)$$

$$V_{out} = V_{CC} - h_{FE}R_2i_B = V_{CC} - KR_2\Delta x \quad (3)$$

Where h_{FE} is the forward current gain and K is a constant given by $h_{FE}k_{eq}$. The two resistor values have been empirically found to have the highest sensitivity but not saturating the measurement. The sensitivity decreases with a smaller resistor, since at a certain point, the Arduino cannot detect a change in voltage anymore. Saturation occurs, when the value of R_2 is too high. Also, it has been opted for keeping the operational distance in the linear range of the sensing position characteristic (see datasheet in appendices).

Identification of Operational Range (Photoreceptor) To find the receptor values at maximum compression of the springs, a simple test has been made, where one time 0V has been applied to the motors, and another time 20V has been applied. The results can be seen in figure 18.

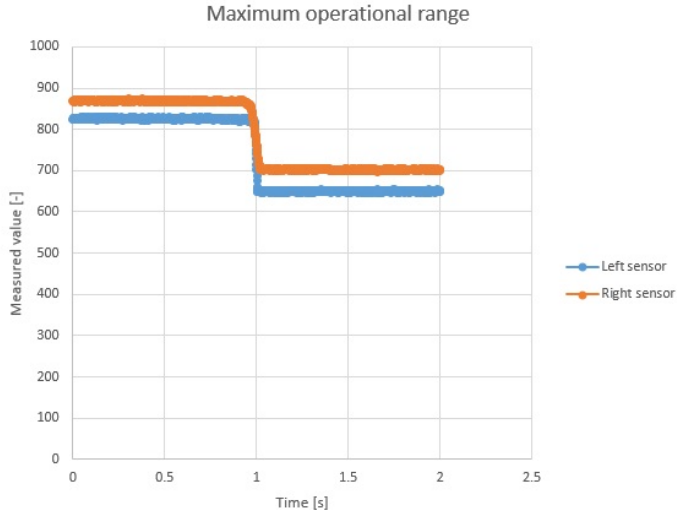


Figure 18: Operational range of photoreceptors with springs at rest and in full compression.

The values that have been found to be the limiting values are resumed in table 2.

	Sensor reading MAX (rest)	Distance (rest)	Sensor reading MIN (compression)	Distance (compression)	Max output force
Left side	830	2.35mm	650	4mm	9.9N
Right side	870	2.2mm	700	4mm	10.8N

Table 2: Identified operational range for the photoreceptors in the game controller.

Using these values, the photoreceptor measurements can be mapped to this range with an 8-bit value. This means that 0 is no compression and 255 is maximum achievable compression. In the Arduino software these values have been slightly adapted (see table 4), to ensure a natural feeling, even when the sensor has some peak values due to noise.

Voltage Interference In the test setup for the frequency response analysis (explained in section 5.3), the Arduino was directly connected to a wave generator. This had an interference with the photoreceptors, as their voltage level was strongly correlated with the input voltage. In order to uncouple the measurement from the input, and to stabilize the measured voltage, a voltage follower with unitary gain (operational amplifier, **LF-412**) has been implemented. Thence, with inactive control, no correlation between input and output has been measured.

2.8 Mechanical Components

From a mechanical point of view, the spring implementation is the most essential part. However, there are other components that have an impact on the output force, the clamp link for instance, whose length acts as a lever. Other minor but non-negligible components are the linear guideway and the coupling.

2.8.1 Springs

The springs are the most crucial part of the entire system. Not only is the output force determined by the spring constant and the compression rate, but also the length and arrangement of the springs have a major impact on the feeling of the controller. Intensive testing has shown that the arrangement has to be symmetric with preferably uniform springs. If springs with two different spring coefficients are used at the same time, the compression becomes rapidly asymmetric and the feedback feels unnatural. Also, if the springs are too long, then a bending into one direction occurs, which causes a buckling effect, felt by the user. This may even result in contact with the casing of the controller and therefore friction or blocking.

For the final controller design, a total of four springs (**WT4-5**), arranged symmetrically on the palm pad have been used. The springs have a spring constant of $k_s = 1.5\text{N/mm}$ which corresponds to an equivalent spring constant of $k_{eq} = 6\text{N/mm}$. They are distributed around the palm pad, where in their middle the distance sensor has been attached, to measure the distance between the L-plate (carriage) and the palm pad. It therefore measures the compression of the springs, which can be related to the output force by Hooke's law as:

$$F = k_{eq}x \quad (4)$$

The setup of the carriage with the springs and the palm pads can be seen in figure 19.

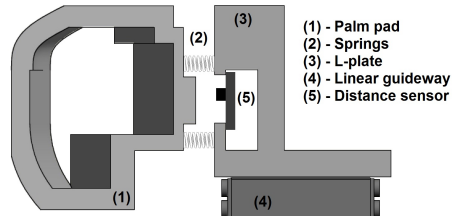


Figure 19: Schematic of the spring system setup.

2.8.2 Linear Guideway

The linear guideway is the model **LS-827** from *THK*. Its maximum stroke is 13mm, which is enough for the compression of the springs, as well as indenting the operators palms to a certain extent. This guideway restricts the movement of the carriage to a unidirectional one.

2.8.3 Coupling

The coupling (**SCPS16-3-5**) and its functionality are straightforward.

2.8.4 Clamp Link

The clamp link acts as a lever pushing the carriage in its guideway. Different lengths have been tested, but the model in the final design is **CLKWS5-3-20**. It converts the rotational motion of the motor shaft to an almost linear motion on the other end. To compensate for the parasitic motions, an additional element called connecting link (see figure 15) has been designed.

2.9 Printed Version

The printed and assembled game controller can be seen in figure 20.



Figure 20: Printed and assembled game controller.

The controller was assembled with 6 screws and nuts and contains the two motors with the complete actuation system.

Once all the design choices and parameters have been fixed, one can create a mathematical model, in order to back the experimental data from the testing phase with the theory.

3 Mathematical Model of the Game Controller

Not only is it interesting to have an underlying mathematical model of the setup for a thorough parameter search, but it can also help to identify important setup parameters that cannot really be measured, such as the operators stiffness and the skins damping coefficient.

To come up with a theoretical analysis of the transfer function, a simplified mechanical schematic has been drawn. This schematic can be seen in figure 21.

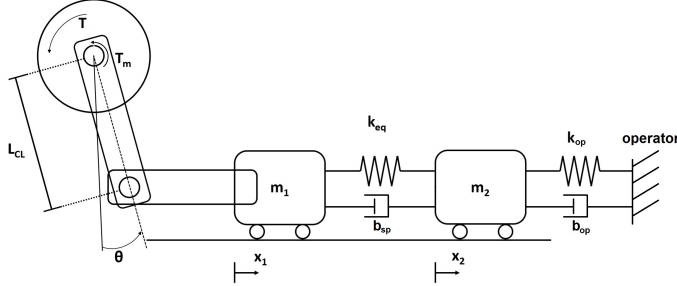


Figure 21: Simplified mechanical schematic of the actuation system with the stimulator (m_2).

The equations of motion can be formulated with the major parameters defined in the schematic. A full explanation of all parameters can be seen in table 3. The variables with subscript 1 refer to the first mass element, the carriage in its guideway, whereas variables with subscript 2 refer to the stimulator, also known as the palm pad. For the motor, the subscript m has been used.

Designator	Explanation	Unit
T_m	Motor torque	[Nm]
T	Output torque acting on the carriage	[Nm]
θ_m	Motor shaft angle (before reduction gear)	[rad]
θ	Clamp link angle	[rad]
L_{CL}	Clamp link length	[m]
m_1	Mass of the carriage in its guideway	[kg]
m_2	Mass of the stimulator	[kg]
x_1	Position of the carriage in its guideway	[m]
x_2	Position of the stimulator	[m]
k_{eq}	Equivalent spring constant	[N/m]
b_{sp}	Spring damping coefficient	[Ns/m]
n	Reduction gear ratio	[\cdot]
k_{op}	Spring constant of the operator	[N/m]
b_{op}	Damping coefficient of the operator	[Ns/m]
J_T	Total inertia of the mechanical setup	[kgm ²]

Table 3: Setup parameters.

3.1 Assumptions

First of all, it is important to mention that the transfer function is non-linear, due to the motor angle θ_m that determines the force acting on the carriage with mass m_1 . As an initial approach however, this effect has been neglected. More specifically, it is assumed that $\theta \ll 1$ and $\cos(\theta) \frac{T_m}{L_{CL}} = F_{carr}$ becomes $\frac{T_m}{L_{CL}} \simeq F_{carr}$. Here the angle θ is the angle of the lever, pushing the carriage (ie. $\theta_m = n\theta$). Furthermore, there are several types of friction in the system: the intrinsic friction within the

motor and its reduction gear, inside the bearings and the carriage in its guideway. Additionally, the springs have a non-negligible damping coefficient. In this work the overall friction and the spring damping have been merged and are represented by the friction coefficient b_{sp} . The stimulator, is not in contact with the controller's casing, but only with the operator. To model the damping of the skin of the operator and the friction between the skin and the palm pad, the damping coefficient b_{op} has been introduced. Similarly, the spring constant of the operator's skin is modeled by k_{op} .

3.2 Spring Constant and Damping Coefficient of the Operator's Hands

The order of magnitude of the two coefficients k_{op} and b_{op} are discussed in [32], [33] and [34]. They all indicate parameters varying in the same order of magnitude, namely $k_{op} \simeq 400\text{N/m}$ and $b_{op} \simeq 5\text{Ns/m}$.

3.3 Identification of the Spring Damping Coefficient

The damping coefficient of the spring b_{sp} can be found by comparing the theoretical results of the frequency response analysis with the experimental findings. In fact, for the experimental setup, the stimulator has been fully blocked and therefore the operator's spring coefficient can be seen as infinitely stiff.

By varying b_{sp} and Bode-plotting the results of the analytical transfer function, the coefficient's order of magnitude can be found. In order to do so, the analytical transfer function has to be identified.

3.4 Expected Transfer Functions

The system can be sub-structured into two major transfer functions. The block diagram including these two transfer functions is depicted in figure 22.

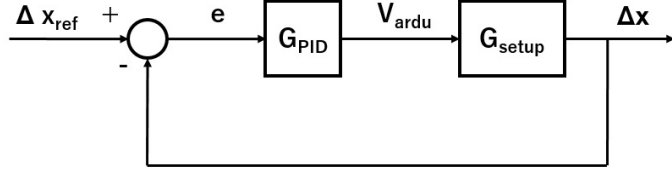


Figure 22: Block diagram with two different transfer functions.

According to this figure one can obtain a transfer function of the following form:

$$F(s) = G_{PID}(s)G_{setup}(s) = \frac{V_{ardu}}{E} \frac{\Delta X}{V_{ardu}} = \frac{\Delta X(s)}{E(s)} \quad (5)$$

where V_{ardu} is the output voltage of the Arduino for controlling the motors. Using this form, one can calculate the individual transfer functions and finally relate the compression of the springs Δx to the compression given as reference Δx_{ref} , since $\Delta X/\Delta X_{ref} = F/(1 + F)$.

3.4.1 PID Transfer Function

The transfer function given by the PID-controller is very straight-forward and can be taken out of any control theory book [35]. Since the Arduino has limited resolution, the error and reference have been converted into micrometers. To keep the gains consistent between the Arduino code and the *matlab* script for analytical analysis, the multiplication factor $K_{\mu m}$ to get from the reference

distance in meters to micrometers has been introduced. Furthermore, an offset has been added ($K_{bit_offset} = 128$) to allow for negative armature voltages (motor voltages) and lastly the PID value has been converted to the Arduino output voltage, where 255 corresponds to 5 V. The transfer function is given in equation 6.

$$G_{PID}(s) = \frac{V_{ardu}(s)}{E(s)} = (K_{\mu m}(K_P + \frac{K_I}{s} + K_D s) + K_{bit_offset})K_{PID2Var du} \quad (6)$$

Finally, there is also the gain of the amplifier in voltage mode, which converts the voltage of the Arduino into the voltage applied to the motors. This gain is $K_{ampl} = 10\text{Volt/Volt}$. To this voltage an offset voltage of $V_{offset} = -25\text{V}$ is added.

3.4.2 Motor Equations

The second transfer function relates the motor torque T_m to the Arduino voltage as well as the output Δx to T_m . Due to the back electromotive force these two parts are related and have to be treated as a whole.

The output torque T_m of the motor can be calculated using the sum of all torques and the conversion parameters intrinsic to the motor.

Similar to the setup and analysis in [27], the equations of the motor are given as:

$$L_a \frac{di_a}{dt} + R_a i_a + K_{emf} \dot{\theta}_m = V_a \quad (7)$$

where L_a is the armature inductance, R_a the armature resistance and i_a the armature current of the motor. K_{emf} is the back electromotive force constant also given by the motor. V_a is the armature voltage and θ_m is the angle of the motor shaft.

Furthermore, with Newton's second law for rotation, the sum of all torques must be zero, or:

$$J_T \ddot{\theta}_m - \frac{k_{eq} L_{CL}}{n} \Delta x - \frac{b_{sp} L_{CL}}{n} (\dot{x}_2 - \dot{x}_1) = T_m = K_\tau i_a \quad (8)$$

In equation 8 the parameter K_τ is the proportional current torque gain constant, taken from the datasheet. J_T stands for the total equivalent inertia of the motor, the clamping link and the carriage of mass m_1 . The moment of inertia can either be calculated as the sum of all inertias seen by the motor shaft, or measured in a simple test.

3.5 Analytical Inertia Identification

The total inertia of the system is determined by the inertia of the rotor and gears J_m , the inertia of the clamp link J_{CL} as well as the inertia of the carriage assembly with mass m_1 . The last one can be found by simplifying the load to a point mass at distance of the clamp link's length L_{CL} , which yields a moment of inertia of $J_{carr} = m_1 L_{CL}^2$. The gear box affects the inertia seen by the motor shaft by the square of its ratio n :

$$J_{reflected} = \frac{J_{load}}{n^2} \quad (9)$$

We therefore have a total inertia of:

$$J_T = J_m + \frac{J_{CL}}{n^2} + \frac{m_1 L_{CL}^2}{n^2} \quad (10)$$

where J_{CL} can be calculated by approximating it as a cantilever with an off-center axis of distance $L_{CL}/2$ ⁵:

⁵(2018, June 19th) retrieved from <http://www.orientalmotor.com/technology/motor-sizing-calculations.html>

$$J_{CL} = \frac{1}{12} m_{CL} (A^2 + B^2 + 12l^2) \quad (11)$$

where A and B are the width and length respectively.

The calculated total moment of inertia for the motor with a reduction ration of $n = 112$ is:

$$J_T = 6.87 \times 10^{-8} \text{ kgm}^2$$

3.6 Experimental Inertia Identification

Alternatively, one can approximate the total moment of inertia by applying a constant current on the motor and measuring the acceleration. In this case the traveled distance has been derivate twice to find the acceleration, which results in an amplification of errors. Furthermore, the constant current has been kept very low, (between 20 and 100mA), which led to a slow movement and therefore higher friction impact on the measurements. However, the results are consistent with the theoretically calculated values:

$$J_T = \frac{7.5 \times 10^{-4}}{n^2} = 5.98 \times 10^{-8} \text{ kgm}^2$$

3.7 Relating ΔX to θ

The conversion between the angle θ and the carriage's traveled distance x_1 can be found by assuming that the horizontal displacement of the carriage is given by $L_{CL} \sin(\theta) = x_1$. For small angles of θ the Taylor expansion gives:

$$L_{CL}\theta \simeq x_1 \quad (12)$$

The output Δx represents the compression of the springs and is given by $\Delta x = x_2 - x_1$. For finding x_2 the equation of motion given by Newton's second law has been considered.

$$m_2 \ddot{x}_2 = -k_{eq}(x_2 - x_1) - b_{sp}(\dot{x}_2 - \dot{x}_1) - k_{op}x_2 - b_{op}\dot{x}_2 \quad (13)$$

In the case where the stimulator has been blocked by a wall, \dot{x}_2 has been forced to zero. Using the Laplace transform and equation 13 one finds the expression of x_2 :

$$X_2 = -\frac{k_{eq} + b_{sp}s}{s^2 m_2 + b_{op}s + k_{op}} \Delta X \quad (14)$$

3.7.1 Motor and Spring Transfer Function

Combining all the equations one can find the final block diagram, which can be seen in figure 23. From this diagram and the equations mentioned above, one can obtain the transfer functions that relate the output Δx and input Δx_{ref} as introduced in equation 5, where $\Delta X(s)$ and $\Delta X_{ref}(s)$ are the Laplace transforms of the output and input functions respectively.

It is thus possible to study the frequency response by simulating this setup with the assumptions mentioned earlier.

3.8 Main Equations for Analytical Transfer Function

To sum up, the equations leading to the analytical transfer function are represented here.

$$\Delta X_{ref} - \Delta X = E \quad (15)$$

$$((K_P + K_D s + \frac{K_I}{s}) E K_{\mu m} + K_{bit-offset}) K_{PID2Var} K_{ampl} + V_{offset} = V_a \quad (16)$$

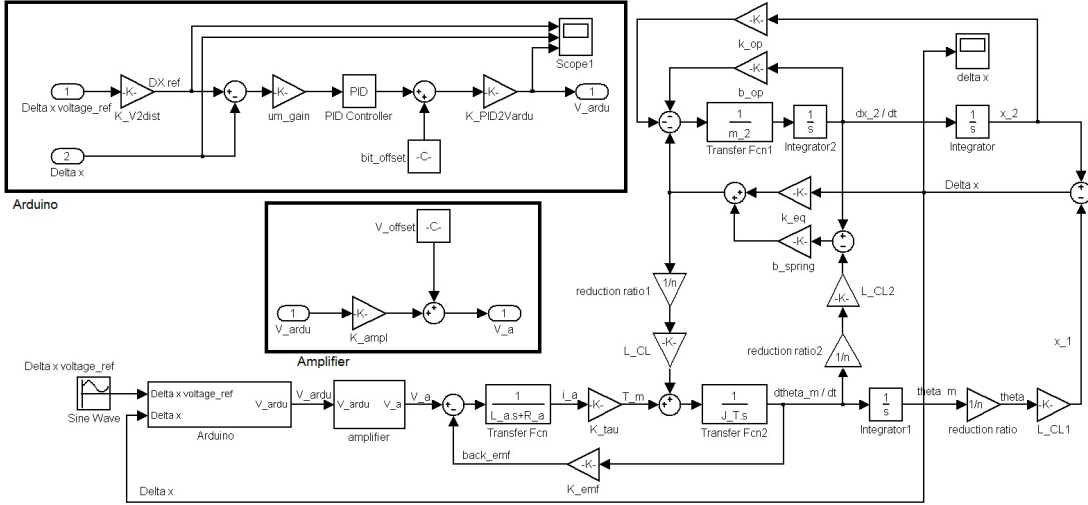


Figure 23: Complete block diagram relating the output Δx to the input Δx_{ref} .

$$\frac{V_a - K_{emf}\dot{\theta}_m}{L_a s + R_a} K_\tau + F_{coupled} = J_T \ddot{\theta}_m \quad (17)$$

$$F_{coupled} = (k_{eq} + b_{sp}s) \frac{L_{CL}}{n} \Delta X \quad (18)$$

$$\theta_m = \frac{n}{L_{CL}} X_1 = -\frac{n}{L_{CL}} \left(1 + \frac{k_{eq} + b_{sp}s}{m_2 s^2 + b_{op}s + k_{op}}\right) \Delta X \quad (19)$$

Note that the constant offsets in equation 16 are for pure symmetrical reasons and will cancel each other out, since $K_{bit_offset}K_{PID2Vardu}K_{ampl} + V_{offset} = 0$ and the equation becomes $((K_P + K_D s + \frac{K_I}{s})E K_{\mu m})K_{PID2Vardu}K_{ampl} = V_a$. This is the equivalent to a standard PID form with gains K'_P , K'_D and K'_I .

In the case of the experimental setup the palm pad has been blocked and therefore x_2 has been forced to be constant. The last equation becomes thus: $\theta_m = -\frac{n}{L_{CL}} \Delta X$.

3.9 Analytical Results

With the identified mathematical model, one can simulate the setup in *matlab*. With the assumption, that all known or directly measurable parameters have been correctly identified and that the mathematical model is correct, the unknown parameters can be studied. Simulations have been done to identify the unknown spring damping coefficient. A parameter search for this coefficient (b_{sp}) has been undergone to obtain the corresponding Bode plots. This damping coefficient also accounts for the friction in the system, since these two effects cannot be discriminated in the experiments.

Comparing the Bode plots with the experimentally gathered data, one can identify the best match and thus obtain a physical value for the equivalent spring damping coefficient. For this however, it was necessary to have fully built the controller and created an experimental frequency response analysis of it. Even though the steps taken for this are explained in the later section, the results can be seen below.

3.9.1 Comparison of Results - P-Controller and Experimental Data

The analytical transfer function has been calculated for a wide set of spring damping coefficients b_{sp} . However, only few potentially best matches are represented in these figures. The results for the uniformly spaced values between 200Ns/m and 400Ns/m are depicted in figure 24a. The gains that have been used are for a P-controller, it was namely $K'_P = 39.2\text{V/mm}$. The results correspond to the setup explained in section 5.2 and were taken after having built the controller. The simulation result that was closest to the experimental setup can be seen in figure 24b and the corresponding transfer function is:

$$\frac{\Delta X}{\Delta X_{ref}} = \frac{1.23 \times 10^3}{3.24 \times 10^{-6}s^3 + 6.67 \times 10^{-2}s^2 + 8.48s + 1.23 \times 10^3} \quad (20)$$

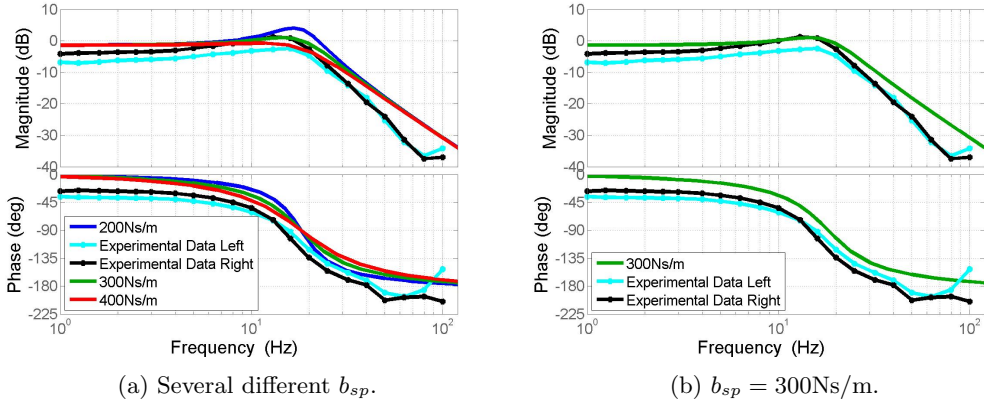


Figure 24: Bode plot comparison of experimental data of the P-controller and analytical transfer functions for different spring damping coefficients (b_{sp}).

Also in figure 24b the gain for lower frequencies of the analytical transfer function is marginally less than 0 and a slight resonance top becomes visible around 18Hz. The phase shift of the experimental data has a non-negligible offset with respect to the analytical curves. At low frequencies, the offset or phase lag is -45° and it reaches a value around -205° for the highest tested frequencies, whereas the analytical model asymptotically approaches -180° . Due to the setup constraints, the analytical results of higher frequencies have not been considered.

The identified spring damping coefficient that seems to best match the experimental data of the P-controlled setup is $b_{sp} = 300\text{Ns/m}$.

Due to this non-perfect tracking, especially for low frequencies, a better performing controller had to be studied.

3.9.2 Comparison of Results - PID-Controller and Experimental Data

With the gains stated in table 5, section 5.11, the frequency response can be calculated again. This has been done using the motor with a reduction ratio of $n = 112$. The comparison between the analytical results and the experimentally gathered data can be seen in figure 25.

This time the analytical model does not match the experimental data equally well. Even though the same resonance top is present for a spring damping coefficient of $b_{sp} = 100\text{Ns/m}$, the high frequency prediction is quite different from the actual data.

The analytical system from figure 25 still shows a second order behavior, since the phase lag will asymptotically go to -180° , but the graph has been cut at the frequency range of the test setup.

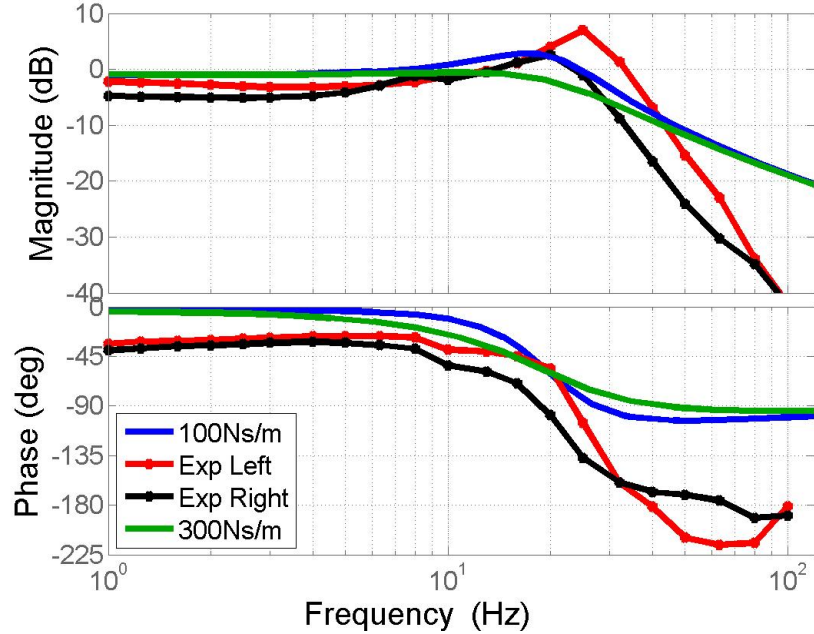


Figure 25: Bode plot comparison of experimental data of the PID-controller and analytical transfer function for $b_{sp} = 100\text{Ns/m}$ and $b_{sp} = 300\text{Ns/m}$.

Comparing the analytical and experimental data, one sees that for low frequencies the experimental data still has a rather high phase lag, ie. -45° . This constant delay seems quite big (ie. a delay of 0.125s for 1Hz) and the cause of it cannot be identified with full certainty.

An initial guess would be, that there is a static friction in the system, that needs to be overcome and therefore introduces a delay. Also, the mechanical aspects such as backlash or movable parts that should be fixed might account for this phase lag. In addition to this, mechanical misalignment can introduce stress in the system, which causes this kind of behavior. The most plausible explanation however, is the presence of a hysteresis effect (a more in-depth analysis of this can be seen in section 8.5).

The additional offset for the middle and high frequency range (compared with expected theoretical behavior) is governed by several different factors. Here the delay stems from the fact that several filters have been put in place. The first one is an electric RC-circuit that filters the PWM signals sent to the amplifiers. However, the cut-off frequency is at 330Hz and the delay should have no impact for the tested frequencies. The second filter is within the Arduino code and is used to filter the measured distance. This is a very basic digital filter explained in more detail in equation 26 in section 5.13.

This filter was necessary to reduce the impact of noise amplification in the derivative part of the PID-controller. Three different filters with cut-off frequencies from $f_1 = 1.6\text{Hz}$, $f_2 = 4.2\text{Hz}$ and $f_3 = 8.8\text{Hz}$ have been tested. These filters did not yield significantly different Bode plots compared with each other. The performance of these filters can be seen in figure 44 in section 5.13. But with such low cut-off frequencies, a non-negligible delay for low frequencies is induced which might account for the high phase lag.

Another source of this error is the fact that the discretization becomes more important in the PID-controlled setup. However, even when one tries to analytically discretize the system, the results do not match the empirical data. To improve the theoretical model, it is suggested to implement

the effects of this digital filter in the analytical transfer function.

For the sake of the argument, the derivative part has been lowered by a factor of 10% and the results can be seen in figure 26.

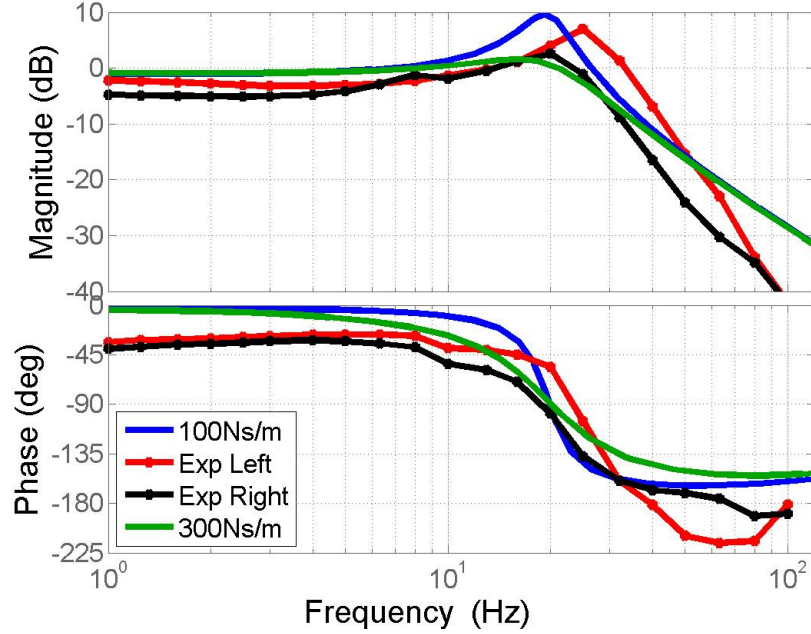


Figure 26: Bode plot comparison of experimental data of the PID-controller and analytical transfer function for $b_{sp} = 100\text{Ns}/\text{m}$ and $b_{sp} = 300\text{Ns}/\text{m}$. The derivative gain is $K_D = 24.7\text{Vs/mm}$.

Judging by figure 24a, one can also suggest a control structure without a derivative gain. In fact, the small resonance peak but steady-state offset (gain smaller than 0dB) for low frequencies suggest, that an integral action is reasonable. Therefore, the system has also been tested with a PI control scheme, where the proportional gain was $K_P = 31.7\text{V/mm}$ and the integral gain was $K_I = 0.183\text{V/mm/s}$. The results are shown in figure 27.

Note , that this test has only been done in the end of the project. For this reason, the analysis and experimentation in the following chapters is mainly based on the P- and PID-controller. For future work, it is suggested to adopt the PI control scheme.

3.10 Analytical PID Gain Domain Study

In order to understand the influence and order of magnitude of applicable gains, a theoretical analysis has been conducted, using the mathematical model. It is important to keep in mind, that the digital filter has not been modeled, which is why a strong discrepancy between experimental data and theoretical analysis will arise when focusing on the derivative gain.

When varying the proportional gain, one shifts the Bode plot in a horizontal direction. A higher gain will yield a better frequency response and therefore shifts the graphs towards the right-hand side. However, a too high gain causes saturation of the system (ie. motor voltage) or instability, which is not included in this simulation. Moreover, a higher proportional gain lifts the Bode plot on the y-axis, resulting in sharper resonance peaks. The tested proportional gain range is between

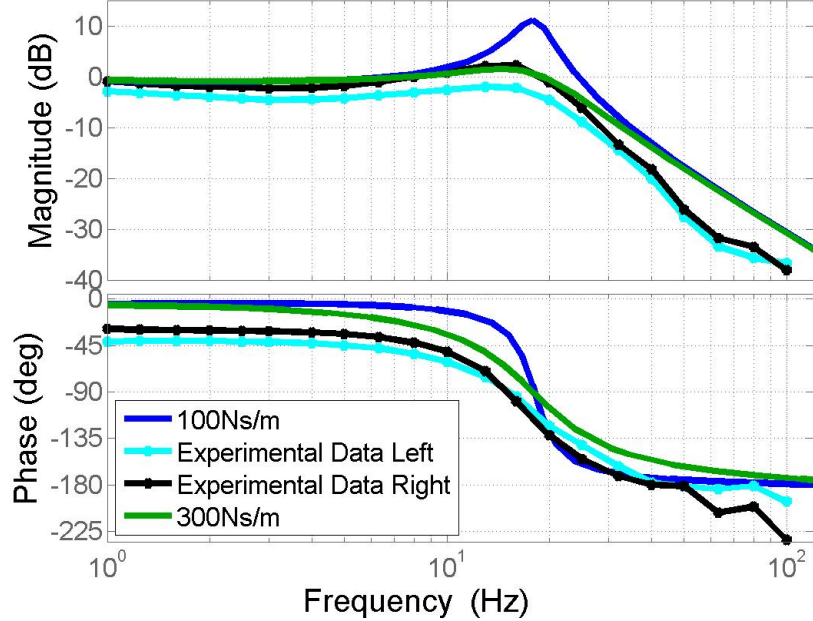


Figure 27: Bode plot comparison of experimental data of the PI-controller and analytical transfer function for $b_{sp} = 100\text{Ns/m}$ and $b_{sp} = 300\text{Ns/m}$.

39.2V/mm and 400V/mm. The upper end will yield an oscillation frequency of 55Hz and a gain of 20dB at said frequency.

A higher integral gain sharpens the resonance peak (higher value) and yields a phase plot that resembles a step-function (rectangular-shaped). The gains varied between 0.06V/mm/s and 1.2V/mm/s.

The derivative part has a very different impact for experimental and analytical data. In practice, a gain of 247Vs/mm has been chosen. The simulation using this K_D is also represented in figure 25. The system is of second order and reaches -180° at 10^5Hz . In practice however, the Bode plot looks rather different.

In general, a lower derivative gain provokes a higher resonance peak value, with almost no vertical shift of the Bode plot. The phase curve sharpens and approaches a more step-like function with lower gains. Furthermore, for too high gains (ie. 25Vs/mm), the phase starts to not directly approach -180° and swings around this value at high frequencies (between 100Hz and 10^5Hz). The tested values are between 2.5Vs/mm and 250Vs/mm. Even though a gain of 2.5Vs/mm seems reasonable according to the simulation, the finally implemented gain was of 247Vs/mm. This decision has been based on the experimental results and evaluation of the controller.

When varying the damping coefficient, one can see that a lower damping coefficient results in a bigger peak value for the resonance top. On the phase plot, the curve for a lower damping coefficient becomes sharper.

The final parameter that has been tested in the analytical simulation is the spring coefficient itself. Figure 28 shows the different results when varying the spring constant for the identified P-controller. A stiffer spring leads to a weaker magnitude value, but shifts the magnitude plot towards higher

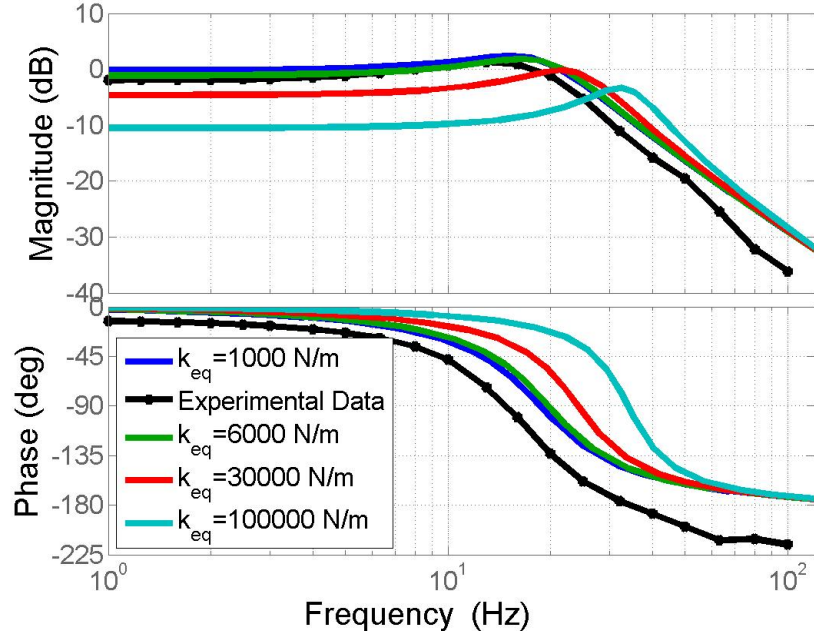


Figure 28: Bode plot comparison of experimental data of the P-controller and analytical transfer function for different spring coefficients (k_{eq}).

frequencies. The phase curve is only affected to a small extent, where the major change is in a horizontal shift as well. The oscillation frequency for 1N/mm is around 17Hz, whereas the oscillation frequency for 100N/mm lies at 35Hz. The damping coefficient that has been used in this case was of 300Ns/m.

4 Robot and Environment

To test the controller, a robot developed by Topy was at disposal (see figure 29).

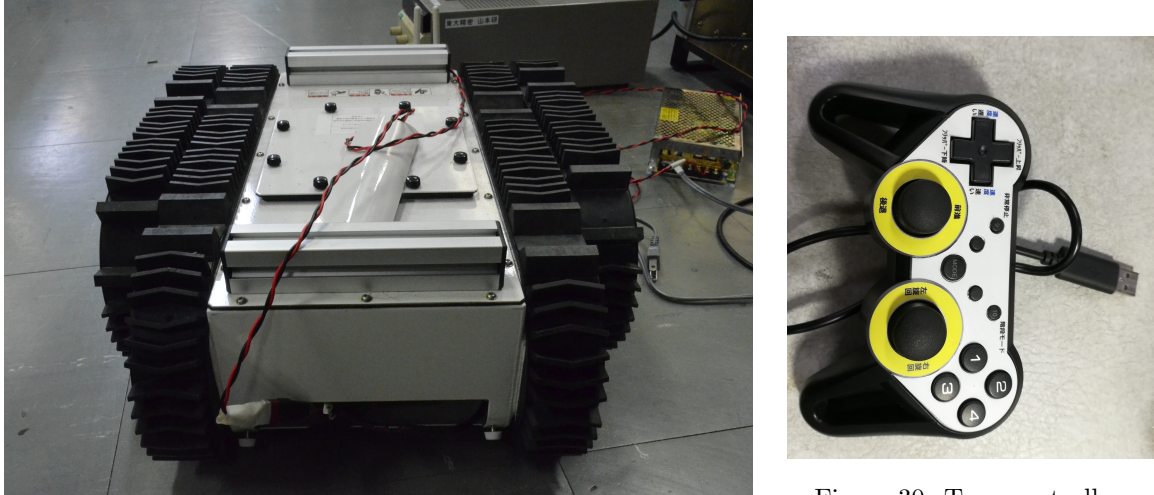


Figure 29: Topy robot for real-world controller test setup.

Figure 30: Topy controller.

This is a commercially available robot with its own controller. In order to replace this controller with the haptic feedback controller from this project, it was necessary to write a properly working environment. The Topy robot is communicating via a wireless serial link. It has a prespecified communication message that consists in 70 bytes for sending from the robot to the PC and 44 bytes for the message to receive. These messages include the bytes reserved for proper starting and ending as well as the checksum. The full documentation of the messages and robot usage can be seen in the Topy manual (translated from Japanese) in the appendices.

It was thus necessary to write an application that reads out the position of the two joysticks and construct a message including these joystick values as speed reference for the robot. Then the message has to be sent over the wireless serial link to the robot and the answer has to be received. The important sensor readings (inclination, current in the crawlers, passed time and battery level) have to be read out and a voltage command for the desired feedback according to the chosen feedback law has to be sent to the motors.

For this purpose, the programming language Processing [36] has been used to create a graphical user interface and to establish the serial connection. For low-level motor control purposes, an Arduino Uno has been used. The parameters that can be set for testing purposes can be seen in table 4.

4.1 About the Robot

The robot is an all-terrain, multi-purpose robot, capable of driving over obstacles and slopes with its main crawlers. Attached to the crawlers it has two flippers that also allow to overcome bigger obstacles or even climb stairs.

The robot measures 45cm in length, 37cm in width and 17cm in height. It weighs around 13kg and has a 10Ah Li-Fe battery rated at 13.2V on board. However, this battery was not in its best condition and had to be replaced with an alternative power source. Furthermore, the robot is equipped with a WiFi transceiver that can establish a serial connection to the computer, such that it can be operated by the controller plugged into the computer.

Due to the all-terrain accessibility of the robot, it seemed a perfect target to develop an intuitive haptic feedback controller for it, to gain more insight over the obstacles the robot is driving over.

Setting	Value	Units
Baud rate for robot serial link	250000	[bps]
Baud rate for Arduino serial link	250000	[bps]
Update rate of the Processing GUI	5	[Hz]
Robot-controller communication frequency	5	[Hz]
Update rate of the Arduino motor controller	1000	[Hz]
Max voltage for motor	20	[V]
PWM frequency	31372.55	[Hz]
Proportional motor gain	47.6	[V/mm]
Integral motor gain	0.124	[V/mm/s]
Derivative motor gain	247	[Vs/mm]
Left photoreceptor MIN value	640	[‐]
Left photoreceptor MAX value	840	[‐]
Right photoreceptor MIN value	700	[‐]
Right photoreceptor MAX value	880	[‐]

Table 4: Software parameters.

4.2 Hardware Setup

The hardware schematic is shown in figure 31. The main connections are the serial link cable between the Arduino and the computer, the wireless serial link between the computer and the robot, as well as the power lines from the amplifiers to the built-in motors in the haptic controller.

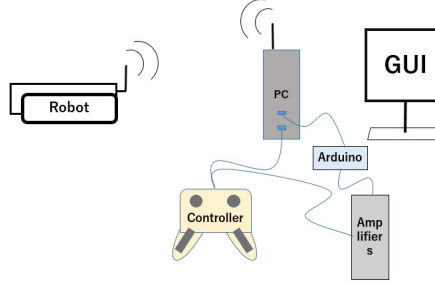


Figure 31: Hardware connection schematic.

4.3 GUI in Processing

The graphical user interface shows the current feedback method as well as the magnitude. It also indicates which driving direction (forward, backward or halt) is sent to the robot. Since there is no control of the battery charge on-board, the robot includes battery information in its message to the PC. The Processing program reads out the charge of the battery and warns the user if it is low. It stops the program, if the battery state is critical. The feedback method can be changed by a mouse-click anywhere in the window. The GUI can be seen in figure 32.

4.3.1 Message Handling

This application handles the messages sent to and from the robot. The communication between the GUI and the Arduino takes place over the serial cable with a fixed baud rate (see table 4). The same baud rate has been used for the communication between the GUI and the real robot. The latter communication frequency is of 5Hz, which has been suggested by the Topy user manual.

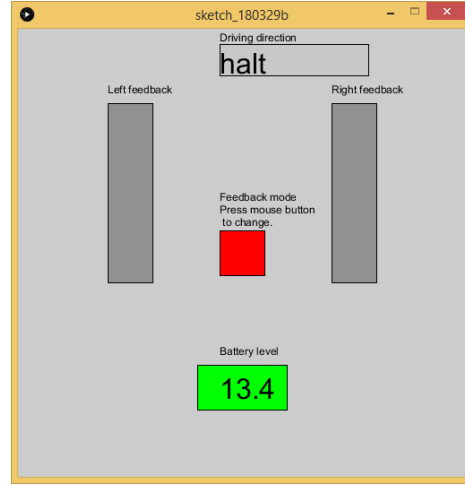


Figure 32: Graphical user interface written in Processing.

The message description from the manual and its translation can be seen in the appendices. The message size for sending is 70 bytes long, while the message from the robot is of 44 bytes.

4.4 Control Scheme

At a first state, the control scheme is based on a simple proportional controller. The full scheme can be seen in figure 33 which implements the part of the control scheme that was already shown in figure 5. In the test setup (see section 5, figure 34) the reference signal $dist_{ref}$ is given by the sinusoidal function generator. This reference signal is directly treated as desired feedback. In the operational mode, this corresponds to the target output force, also called the haptic feedback force that should be felt by the user. Ideally, this shall be a function of orientation (roll and pitch) as well as the current in the two crawlers.

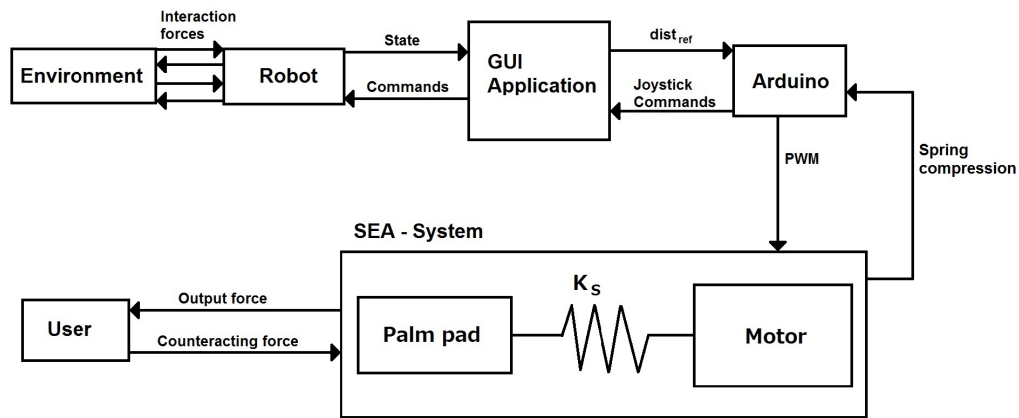


Figure 33: Complete system scheme of the robot in its environment and the user.

4.5 Electrical low-pass Filter

Before the PWM signal from the Arduino is sent to the amplifiers, where it is amplified to control the motors, it has been filtered with a simple RC low-pass filter. The resistor has a value of $3.9\text{ k}\Omega$ and the capacitor of $0.1\text{ }\mu\text{F}$. This smooths out the PWM signal and has been implemented in order to prevent the amplifier from trying to follow the Arduino signal with unwanted precision, eventually causing too much heat. The cut-off frequency is 204Hz .

4.6 Amplifiers

The amplifiers that have been used are the **BPS120-5** and **BWS60-5**. In operation, the amplifiers were set to voltage to voltage amplification mode with a gain of 10V/V for both amplifiers. The operation mode was set to amplification and an offset of -20V has been added.

4.7 Feedback Laws

The previous research in this project suggested to use a feedback law, that couples both the roll and pitch orientation of the robot. The underlying law of this idea is given in equation 21, where θ_p and θ_r are the pitch and roll angles of the tank in the Unity simulation respectively.

$$F = K_1(\sin \theta_p \pm \sin \theta_r) \quad (21)$$

In the Processing application (GUI) the feedback of the robot is extracted from the received message. By simply clicking somewhere in the window, the user can switch between three feedback laws. The first one is the same as in the previous paper, with the difference that the operator \pm has been replaced by a simple $+$ which results in uniform feedback for both sides. The second and third feedback laws are indicated in equation 22 and 23. In the latter, i_{cl} and i_{cr} are the currents in the left and right crawler respectively. For testing, mainly the last law has been used, since there were not so many obstacles to overcome in the testing environment and therefore the orientation did not change much.

$$F = K_2(\sin \theta_p \sin \theta_r) \quad (22)$$

$$F = K_3(i_{cl} + i_{cr}) \quad (23)$$

5 Testing of the Game Controller

5.1 Frequency Response Function

For an in-depth performance analysis and evaluation of the controller a series of experiments has been conducted. A standard approach is to measure the frequency response function of the controller. In order to find this frequency response, one should consider the amplitude correlation between the input signal and the output signal, as given in the following equation:

$$H = \frac{F^*(j\omega)}{F(j\omega)} \quad (24)$$

Where $F^*(j\omega)$ is the transfer function of the output signal and $F(j\omega)$ of the input signal.

The results of this testing can be plotted in a Bode-plot which is a standard representation. This not only shows for which frequencies the reference signal can be tracked nicely, but it also indicates any potential oscillation frequencies. In addition, one can read out the order of the system when looking at the phase plot of the frequency response function. In the phase plot the phase lag between the reference signal and the output signal is represented. Furthermore, the Bode plots allow for a direct cross-platform comparison with other controllers and devices.

5.2 Test Setup

In this experiment a thorough frequency response analysis shall be done on the controller. On the left-hand side, the motor with a reduction ratio of 33:1 has been used, whereas for the right-hand side, the motor had a reduction ratio of 112:1.

A reference signal is fed into the Arduino, which then controls the motors to match the compression of the springs with the reference. The operational distance of the photoreceptors to the palm pads is 2 to 4mm which lies within the more sensitive region of the sensor.

5.3 Control Scheme

The reference signal is given by the Function Generator **SG-4115**. This generator has an intrinsic output impedance of 50 Ohm. This means that it expects to have a device connected to it with the same value as input impedance. If this is the case, these two elements form a simple voltage divider and only half of the voltage is applied to the target device. However, this is not the case for the Arduino, since it has a considerably higher input impedance. Therefore, the settings made on the function generator result in double the voltage on the Arduino. From this point on, this issue shall be neglected and all future voltage indications refer to the voltage level as seen by the Arduino.

The function generator produces a sine wave between 0 and 5V with a frequency ranging from 1 to 100Hz. The Arduino reads this voltage and controls the motor to have a proportional spring compression accordingly. In this case, 0V as reference signal is 0% compression and 5V corresponds to 100% compression. The control scheme of this setup can be seen in figure 34.

In this case the counteracting force from the user is perfect (ie. pseudo-infinite stiffness), since the palm pads have been blocked by a wall. Tests have also been made where the palm pads have been blocked by the operators hands, but without any significant difference. For simplicity, the wall-blocked test setup has been used for these investigations.

5.4 Tracking Behavior of the P-Controller

In order to measure the tracking performance of the controller, the Arduino sent its data via serial link to the computer. This data has then been read and treated in a python script and represented with the *matplotlib* library.

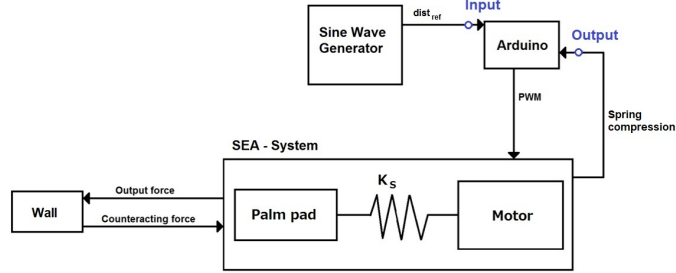


Figure 34: Control scheme for the frequency response analysis.

5.5 Step Response

In order to gain more insight in the controller's behavior and performance, a step response analysis has been done. When using the P control scheme, the performance indicated in figure 35 can be obtained.

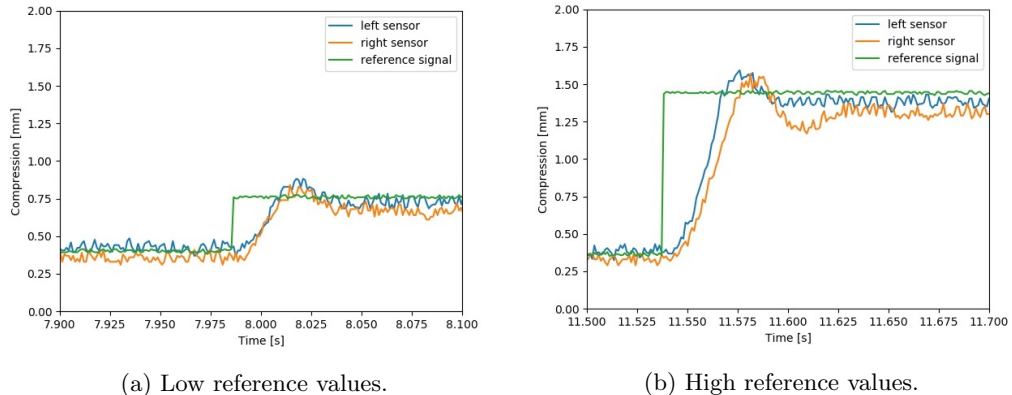


Figure 35: Tracking behavior of the P-controller for different step response input.

When comparing this result with the analytical data, one obtains the graph from figure 36. In figures 35 and 36 the response time has been calculated using the threshold values of 10% and 90% (also indicated in analytical results). This yields the response time of 10ms and 15ms for the experimental data, and 15ms for the analytical.

The same analysis has been done for a PI controlled setup, where the proportional gain was $K_P = 32V/mm$ and the integral gain was $K_I = 0.183V/mm/s$. The results can be seen in figures 37 and 38.

The delays are 12ms and 18ms for the experimental setup and 23ms from the analytical results. This time, the measured compression goes asymptotically towards the reference compression. The steady-state offset has successfully been removed. For comparison, the steady-state solution of the P-controller is represented by the dashed green line.

5.6 Sine Tracking

The tracking behavior of the P-controlled ($K_P = 39.2V/mm$) setup can be seen in the following figures.

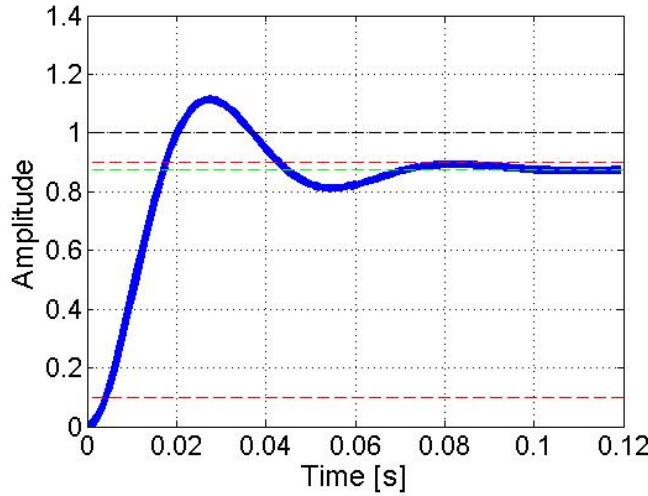


Figure 36: Analytic unit step response of the P-controller.

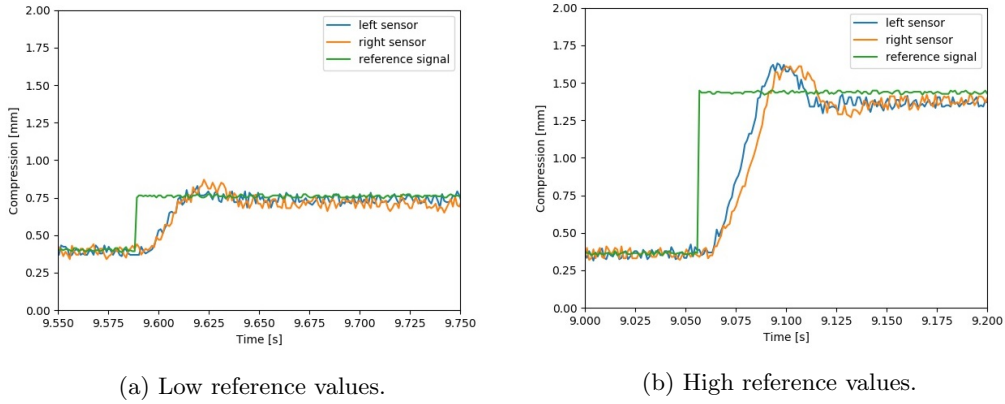


Figure 37: Tracking behavior of the PI-controller for different step response input.

5.7 Sine Wave Fitting

As described in this example[37], one can fit a sine wave with the linear least square method to the samples. For finding the amplitude, the second norm has been used. This function returns the phase, amplitude and the bias. In this case, the difference in phase between input and output, as well as the amplitude ratio is needed in order to plot a Bode diagram.

5.8 Bode Diagram

The results of the frequency response analysis are shown in figures 40a and 40b.

For the left-hand side, a resonance peak at around 30Hz can be found, with a gain of roughly -8dB for lower frequencies. At higher frequencies a slope of roughly -30dB/dec has been calculated. For doing so the values in the range of 50Hz and 100Hz have been used. The phase shifts from -35° to -210° , a total shift of roughly 175° .

For the right-hand side, the resonance peak has a lower maximum and the cut-off frequency is

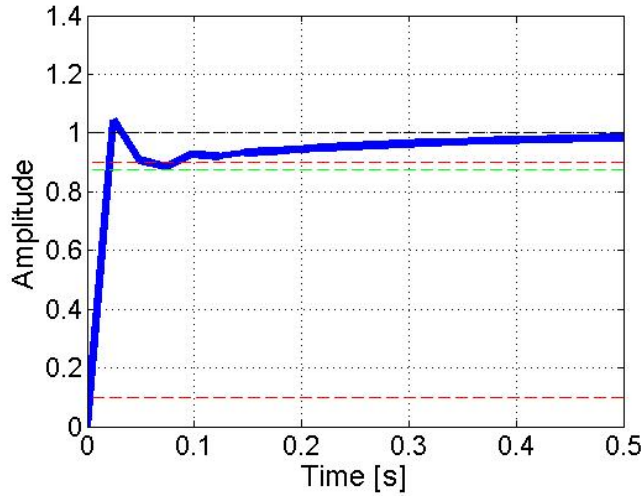
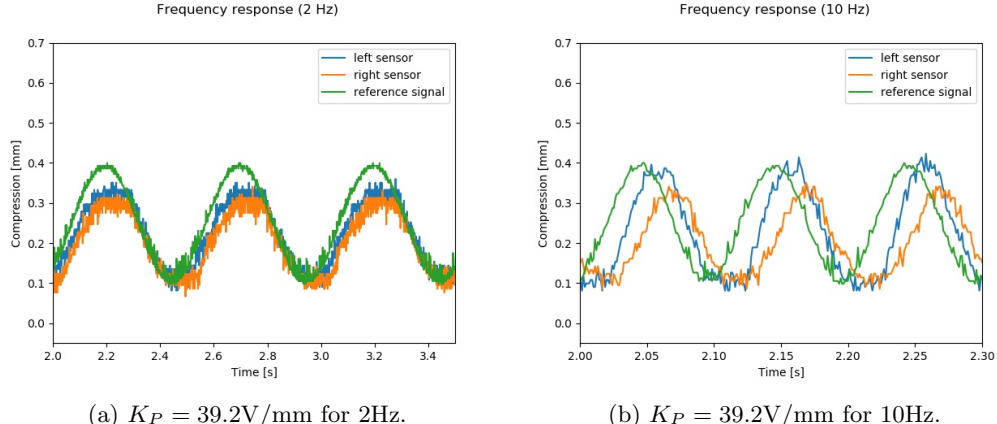


Figure 38: Analytic unit step response of the PI-controller.



(a) $K_P = 39.2\text{V/mm}$ for 2Hz.

(b) $K_P = 39.2\text{V/mm}$ for 10Hz.

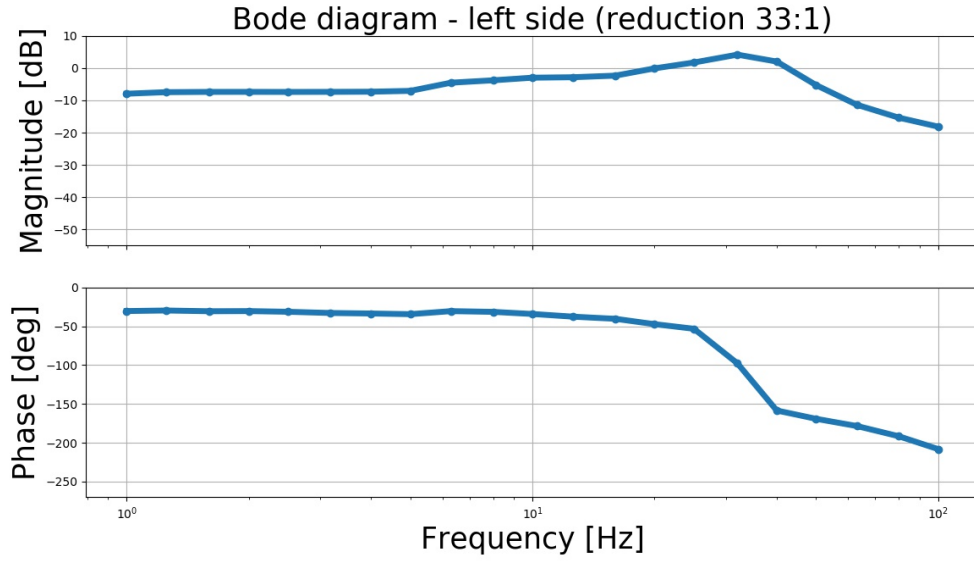
Figure 39: Tracking behavior of the P-controller for different frequencies.

around 13Hz, and a constant gain of roughly -4dB for lower frequencies can be identified. At higher frequencies the same slope of -30dB/dec has been calculated, again, using the values in the range of 50Hz and 100Hz. The phase shifts from -25° to -225° , a total shift of roughly 200° . From the phase shift one can calculate the delay for the desired frequencies. For a frequency of 1Hz, the delay is 70ms. Even though this seems like a big delay, it meets the requirements stated in section 1.7.

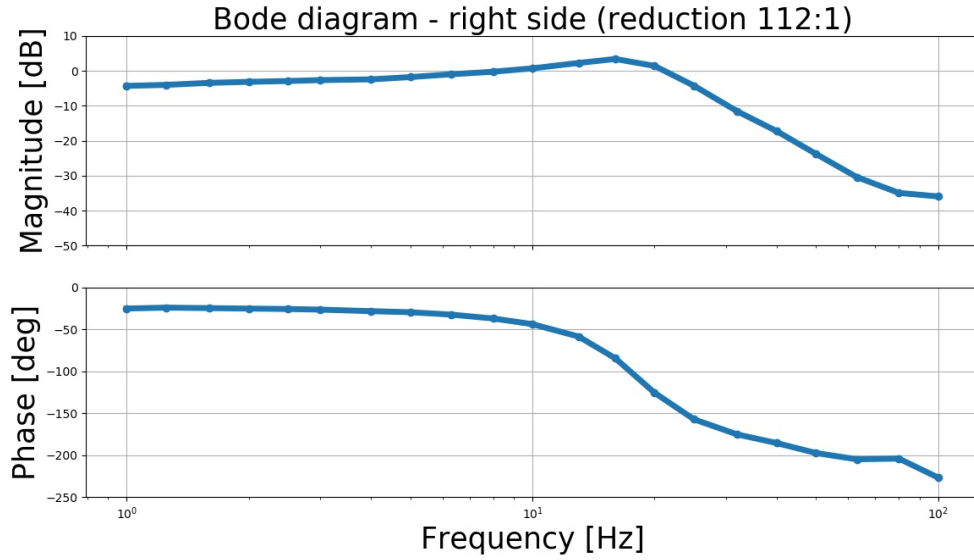
5.9 Discussion of the P-Tracking

As shown in figures 39a and 39b, the signal is not followed perfectly. For one, the magnitude ratio even at low frequencies is at roughly 0.85 for the right side. This shows that the proportional gain is too low. This would not only lift up the curve indicated in the Bode diagram, but also shift it towards higher frequencies (to the right).

From the Bode diagrams one can conclude several things. First of all, the gain magnitude at lower frequencies should be around 0dB to have perfect following of the reference signal. This can be



(a) Left-hand side, Motor reduction ratio 33:1.



(b) Right-hand side, Motor reduction ratio 112:1.

Figure 40: Bode diagrams for the two motors.

influenced by tuning the proportional value of the controller, or introducing an integral part. Second, the two motors show different characteristics. While the weaker motor (left-hand side) shows a resonance top around 30 Hertz, the stronger motor behaves differently. For the right-hand side, the first pole of the system can be found around 13 Hertz. The communication frequency between robot and graphical user interface is suggested (according to the datasheet of the robot) to be between 2Hz and 5Hz. This shows that the series elastic actuator system as it

is implemented in this experiment, is not the limiting factor in the robotic system. The controller therefore successfully meets the previously stated requirements.

When wanting to determine the order of the system, one can look at the slope at the tail of the magnitude curve in the Bode plot. In our case they are -30dB/dec for both sides. Since the slopes can only be a multiple of 20dB/dec , it can be concluded, that the $2\xi\omega_0$ term from equation 25 has a non-negligible influence on the tail of these Bode plots. The equation of a second order transfer function is as follows:

$$H(s) = \frac{\omega_0^2}{s^2 + 2\xi\omega_0 s + \omega_0^2} \quad (25)$$

Therefore one should also have a look at the phase lag diagram. The phase shift of roughly -180° suggests a second order transfer function.

5.10 Motor Comparison

When comparing the two motors at hand, one can conclude that the motor with the higher reduction ratio has a higher output force with a speed trade-off. Since one of the critical elements of the SEA system is its actuation speed, it is essential to push the boundaries as far as possible. However, the high gain frequency response in the experimental setup starts to drop at much higher frequencies than the actual operating frequency (which is given by the rather slow communication speed between the robot and the control device of $f_{op} \simeq 2 - 5\text{Hz}$).

Due to the fact that even with the stronger reduction gear motor, the springs cannot be compressed to their limits, a higher possible output force has been favored and therefore the stronger motor seemed more appropriate. From this point on, only the motor with reduction ratio of $112:1$ has been considered for this controller.

When one replaces the left motor to have two identical motors, the following Bode plot can be obtained (see figure 41). The two curves overlap nicely, except for the phase values for the highest frequency (100Hz). This is due to the noise in the photoreceptors that becomes dominant at such low gain magnitudes and has no further significance.

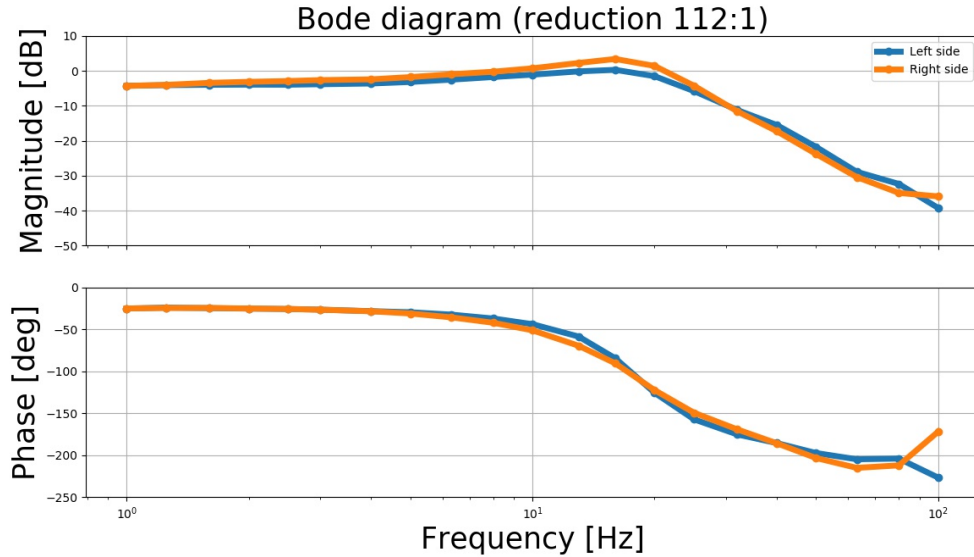


Figure 41: Bode plot for both motors with same reduction ratio, P-controlled.

5.11 Experimental PID Tuning

In order to compare the P-controller to potentially better controllers, it has been extended to a PID control scheme.

At first, the Ziegler Nichols tuning method has been used to identify the PID gains for the setup. However, due to the non-linear behaviour, these gains resulted in a rather poor tracking performance of the reference signal.

Since an educated tuning of the gains is the very core problem of all control engineering, a lot of different approaches exist to find optimal or sub-optimal gain values. Given the complexity of the setup, it seemed reasonable to opt for the simple trial and error approach, where the gains have been tuned and the tracking performance was shown in real-time. This approach led to the following gain coefficients:

Designator	Value	Unit
K'_P	47.6	[V/mm]
K'_I	0.124	[V/mm/s]
K'_D	247	[Vs/mm]

Table 5: Trial and error PID tuning.

5.12 Tracking Behavior of the PID-Controller

The tracking behavior of the PID-controlled setup can be seen in figure 42.

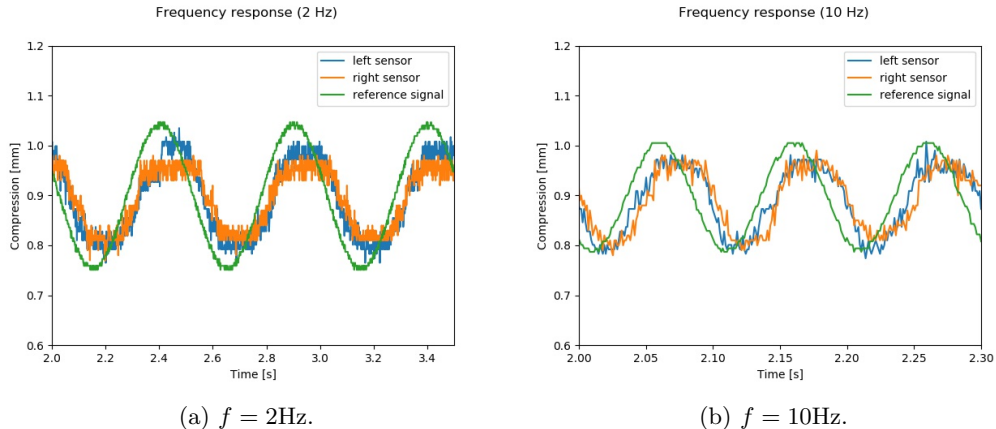


Figure 42: Tracking behavior of the PID-controller (for gains see table 5) for different frequencies.

The same experiment for measuring the frequency response function has been conducted and the Bode plot can be seen in figure 43.

5.13 Discussion of the PID-Tracking

The performance of this controller has not been improved drastically compared to the P-controller. There is still a small negative gain at lower frequencies. Opposed to the previous Bode plot in figure 41, the two sides show different characteristics in figure 43. This might be due to several asymmetries, such as the different sensor thresholds or noise values, or the fact that the gains have been kept the same for both sides.

However, this time the Bode plot has been shifted to the right and a resonance top is more clearly

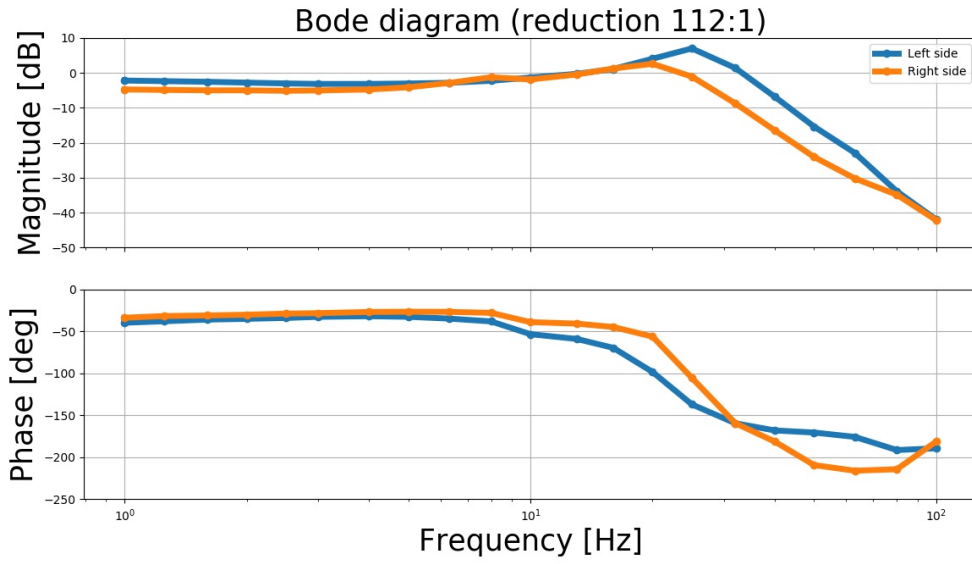


Figure 43: Bode plot for both motors with same reduction ratio, PID-controlled.

visible at 24-25Hz. Similarly, the phase lag is considerably big for low frequencies, starting at -40° , but ending around -180° for higher frequencies. This behavior is difficult to understand.

As it has been mentioned in the theoretical analysis, this might be due to a hysteresis effect. A possible source of this hysteresis is the internal friction in the motors' reduction gear ratios. When the reduction gear is not in motion, a higher force is required to overcome the static friction. However, figure 40a does not show a significantly increased performance compared to figure 40b.

Conclusively, all these Bode plots suggest, that the controller itself already has a latency per se for low frequencies. The origin of this can stem from some non-linearities in the setup, or the fact that a hysteresis curve is present between input and output. This phenomenon has been tested and explained for the second controller (see section 8.5).

The tracking behavior in figures 42a and 42b is still not perfect, which suggests further gain tuning.

A thorough case testing with several filters implemented can be seen in figure 44. The filter that has been changed here is the one that filters the error of the tracking for the derivative part, to reduce the effect of noise.

This is a simple digital filter based on the formula in equation 26, where $x[t]$ is the measured distance at time step t and $y[t]$ is the filtered measured distance.

$$y[t + 1] = \alpha x[t] + (1 - \alpha)y[t] \quad (26)$$

α determines how conservative the filter is, where the cut-off frequency can be calculated as:

$$f_c = \frac{\alpha}{(1 - \alpha)2\pi\Delta T}$$

The cut-off frequencies do not have a major impact on the tracking performance, which is why the first filter has been implemented ($f_c = 1.6\text{Hz}$). This digital filter has a slightly weaker performance than a general first order lag of the form $H(s) = \frac{1}{1+\tau s}$.

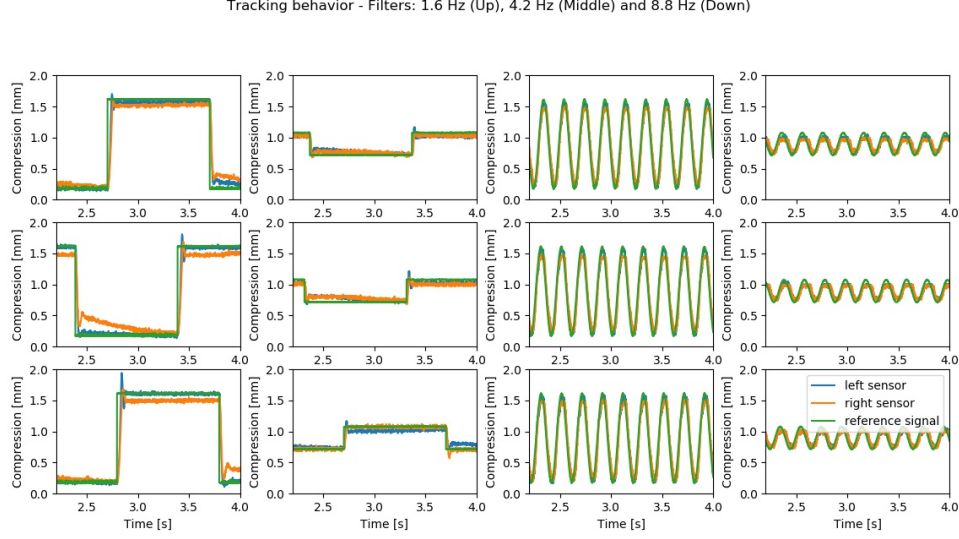


Figure 44: Tracking performance of PID game controller with different derivative filters.

5.14 Performance Evaluation

After having found gains that seem to work well enough for the desired application, the game controller setup was put to the test. At first, the controller was connected to the computer to communicate with the Topy robot.

5.14.1 Latency

The controller was successfully able to navigate the robot, albeit with a delay of roughly 700ms. The commercial controller, that was developed for the Topy robot, also had a certain delay of almost 500ms. This delay is the difference between the instant when the joystick is pushed forward, and the moment when the robot starts moving. The feedback methods that have been tested varied between a sum of pitch and roll feedback, a combined pitch and roll feedback, and a current consumption feedback law (see section 4.7).

The effect and magnitude of the command latency, but also of the feedback latency can be seen in figures 45 and 46.

In these figures, several interesting things have to be mentioned. First of all, the delay between sending the commands and receiving the consumed current value, which is then used as feedback value, is roughly 700ms. The delay between the received feedback value (reference) and the response of the distance sensor is much smaller and depends on the situation of the robot. When the robot starts to move, it takes some time until the current has built up, and the latency between the reference compression and actual compression is roughly 130ms for the P-controlled, and 430ms for the PID-controlled setup (see first red vertical lines). However, when the robot is stopped, the latency is 20 - 30ms (second and third red lines).

This latency is the actual controller's response latency and shows repeatedly, that the controller with its actuation implementation is not the bottleneck of the system.

In the first green lines, an external force has been applied to the robot, simulating an obstacle, which increased the consumed current and therefore also increased the desired feedback value. Again, the latency (between reference compression and actual compression) was of roughly 30ms. The second green lines indicate where the external force has been removed and the current abruptly dropped back to its normal value. The latency here was below 10ms.

Also indicated in figures 45 and 46, one can see that the feedback has been turned off when driving

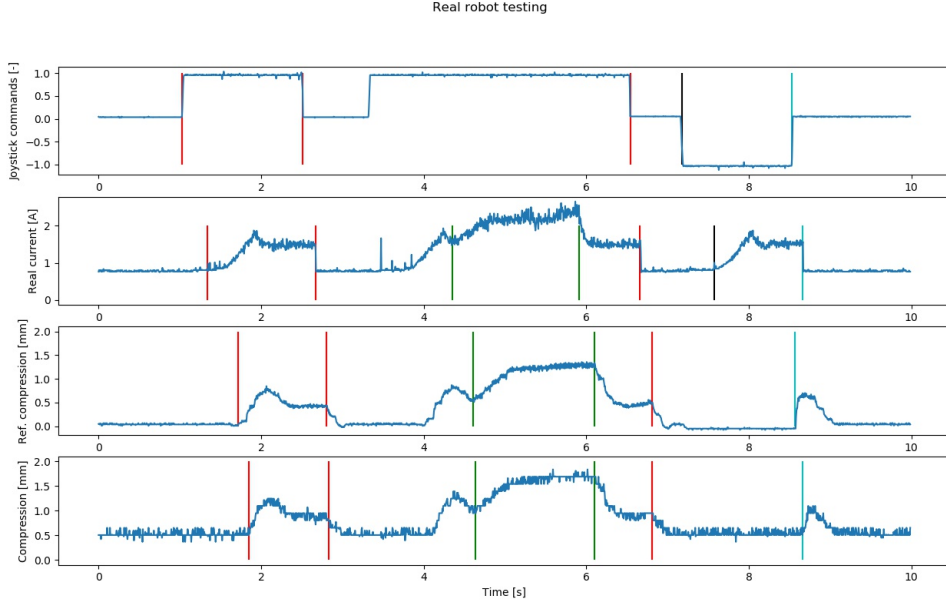


Figure 45: Command and behavior of Topy robot with P-controlled game controller.

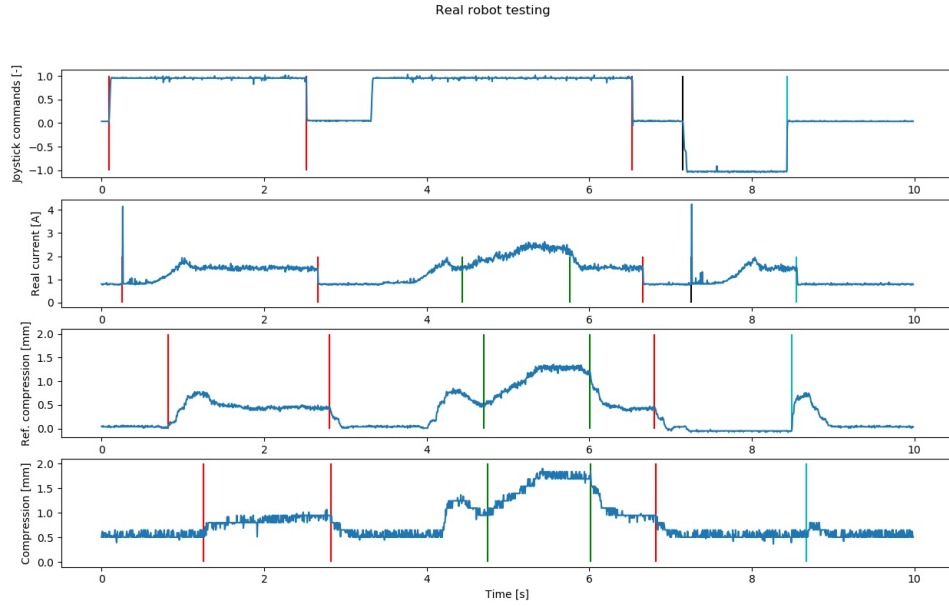


Figure 46: Command and behavior of Topy robot with PID-controlled game controller.

backwards (black lines). However, in this scenario the feedback has been activated when standing still, ie. sending 0 as driving speed. Since the robot is only sending the magnitude but not the direction of the current in the crawlers, the remaining current from the backward motion is fed back. This mode can easily be turned off, so that no feedback is felt when the robot is halting. For the sake of completeness however, this has not been turned off and it is interesting to note, that the time between switching the command values and the reception of the feedback value has been

reduced to roughly 50ms.

From these experiments one can conclude that the robot takes a long time to start driving, mainly due to internal implementation of the crawler control scheme. This is completely decoupled from the controller and cannot be changed in this work.

The total delay for this initial start-up is 820ms for the P-controlled and 1160ms for the PID-controlled version. The communication delay (joystick command and robot's reaction) is 210ms on average. The time between sending the joysticks commands and feeling the feedback is 240ms (P) and 280ms (PID), when excluding the initial start command. The full data has been gathered with an oscilloscope and can be seen in table 6.

	Start	Stop	Ext. force	No force	Stop	Back	Stop	Control
Joy-stick commands sent	1.03	2.51	-	-	6.54	7.18	8.53	P
Measured current in robot	1.34	2.67	4.35	5.91	6.66	7.57	8.66	P
Desired compression	1.72	2.80	4.61	6.10	6.81	-	8.57	P
Measured compression	1.85	2.83	4.64	6.10	6.81	-	8.66	P
Joy-stick commands sent	0.09	2.52	-	-	6.53	7.15	8.43	PID
Measured current in robot	0.26	2.66	4.44	5.76	6.66	7.26	8.55	PID
Desired compression	0.82	2.80	4.70	6.01	6.80	-	8.49	PID
Measured compression	1.25	2.83	4.75	6.02	6.82	-	8.67	PID

Table 6: Latency table for sending joystick commands, current measured on the real robot, desired compression and measured compression. All values indicated in [s].

5.14.2 Transparency and Intuitiveness

Despite the command delay, the feedback from the robot can be felt almost instantly in the user's palms. For example, as soon as the robot is moving forward, one can feel the current building up in the current consumption feedback mode.

The difference between the PID and P-controlled controllers is small, but can still be felt. In the PID-control scheme, one can feel an asymmetry between the left and right palms. This is due to the distance sensors that have different threshold values and the fact that the PID gains have been tuned for one side only. To avoid this asymmetry, it is recommended to identify different gains for the two sides or use sensors with more similar threshold values.

The proportional control scheme is already capable of giving an intuitive feedback of the robot's state. Especially since the feedback value is continuous and does not change much over time for all feedback modes. For these reasons, it seems appropriate to leave the controller P-controlled only. Complementarily, one can also test a PI-controlled setup.

5.14.3 Stability

Both control schemes are stable for various grips and feedback values, but in some cases one can feel and hear a slight oscillatory behavior in the PID-controlled setup. This suggests that the gains are not optimal and that they can further be tuned in future research. However, it is not possible to render the setup unstable even when the user is deliberately trying to do so, acting as a non-passive element. This has to do with the fact that the input using the joysticks is completely decoupled from the output (palm pads).

5.14.4 General Performance

The overall performance evaluation of this controller is rather subjective. The output force of the SEA setup is much bigger than for the voice coil implementation, as it has been anticipated in the

design phase. Since the output force is distributed over the whole area of contact of the stimulators, the user technically feels a pressure instead of the force itself. However, one can call the feedback a pseudo-force as demonstrated in the previous research of this project [10]. One important psychological aspect is the area of the stimulators. If they are too big, the pressure is much weaker and the pseudo-force is below the perception threshold. If the area is too small, the feedback becomes punctual and the edges distort the feeling of the feedback, making it uncomfortable to use and counterintuitive. In this controller design the stimulators have the right ratio between output force and area of contact.

Another psychological aspect is the direction of the feedback. This controller has an angle of roughly 115° with respect to the operator's orientation. During operation the forces tend to push the palms outwards which is not entirely intuitive if one is expecting a force opposing the movement of the robot (180°). This however depends strongly on the target application and the controller design can be well-suited for other environments.

However, the overall feeling is rather good and the performances have shown that the controller was able to successfully meet all design requirements from section 1.7.

Having said that, the biggest issue in this test setup though, is the delay of the command messages. In order to get an idea of the delay of the mechanical setup (the SEA implementation), the controller has also been tested in a purely simulated environment. This eliminates (almost) all potential delays in communication between robot and controller and the results and evaluation can be seen in the next section.

5.15 Unity Simulation

In the previous research, a controller testing environment has been created. It consists of several different landscapes, that include a crawler-based tank, which can be navigated in its world. The feedback is purely based on the roll and pitch angle of the tank.

The environment that has been used for testing is a dune-like desert with small hills to overcome. The feedback that is sent to the controller is different on each side, in order to increase the intuitiveness when driving with a tilt (roll angle). This allows for easy detection of obstacles, even when no visual feedback is given.

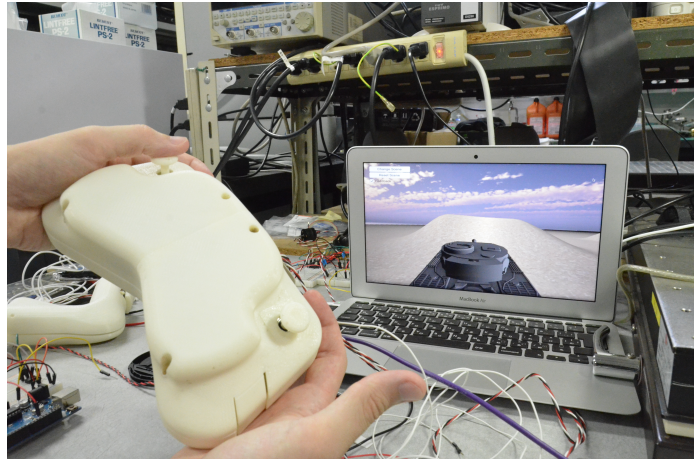


Figure 47: Unity simulation test setup.

For testing the controller in the simulated world, the Unity program from the previous research of this project has been used. With minor modifications of the control software, the controller could

be tested with different feedback for the two stimulators. This time, only the combined roll-pitch feedback law has been used.

5.15.1 Latency

Similarly to the real-world testing of the controller, one can analyze the reaction time of the feedback with respect to the desired output. This time however, the current of the tank has not been measured, instead the vehicle's orientation was used.

In figure 48 one can see the tracking performance for the P-controller ($K_p = 39.2\text{V/mm}$).

The oscillations are tracked relatively nicely, with a high force fidelity. The compression changes smoothly and no friction induced step-wise change can be observed. The plateau has a steady-state offset and the measured compression changes slightly over time. This is due to the non-constant grip of the operator.

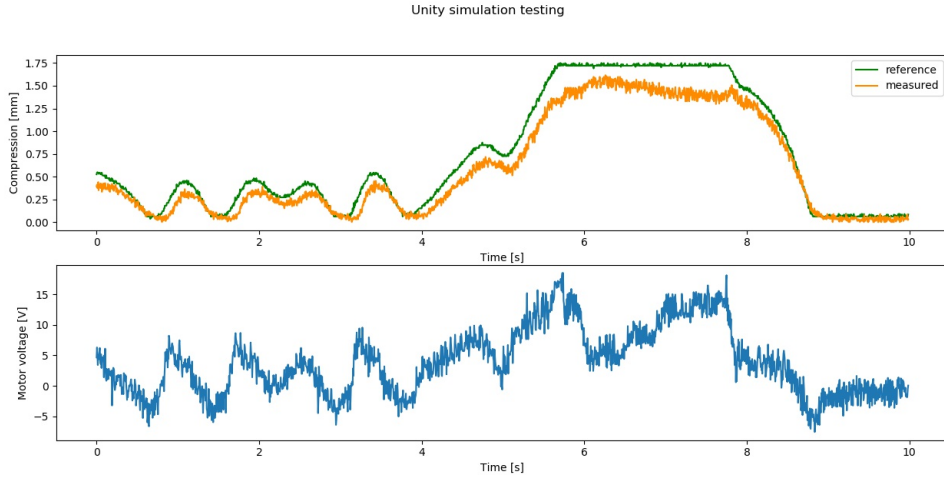


Figure 48: Command and feedback in Unity with P-controlled game controller (handheld).

Since the user cannot provide a constant counteracting force, the controller has also been tested when being blocked by a wall. The results can be seen in figure 49. This time, the plateau is tracked with a constant compression, which confirms that stated hypothesis.

In order to remove the steady-state offset however, the PID (gains stated in section 5.11) control scheme has been tested as well. The results for the handheld and wall-blocked environment can be seen in figures 50 and 51.

With the integral part, the steady-state offset between the target compression and measured compression is removed after a short while and the two curves are almost overlapping. Overall, one can observe a small latency (50ms) when compressing the springs, while practically no latency is present in the decompression phase.

5.15.2 Unity Performance Evaluation

In the Unity simulation all hardware latencies have been eliminated and the simulated tank reacted almost instantly to the environment. Only the serial link cable is left as bottleneck of the speed and latency performances. Even though the serial cable is capable of communicating with a baud rate of 250000 bits per second, this might slow down the system, if a lot of messages are being sent back and forth. The overhead reduces the achievable control frequency of 4kHz (calculated for sending 8 bytes per communication frame) and the error rate increases with higher frequencies. For comparison, the message size with the real robot is 115 bytes, not counting the overhead (maximum

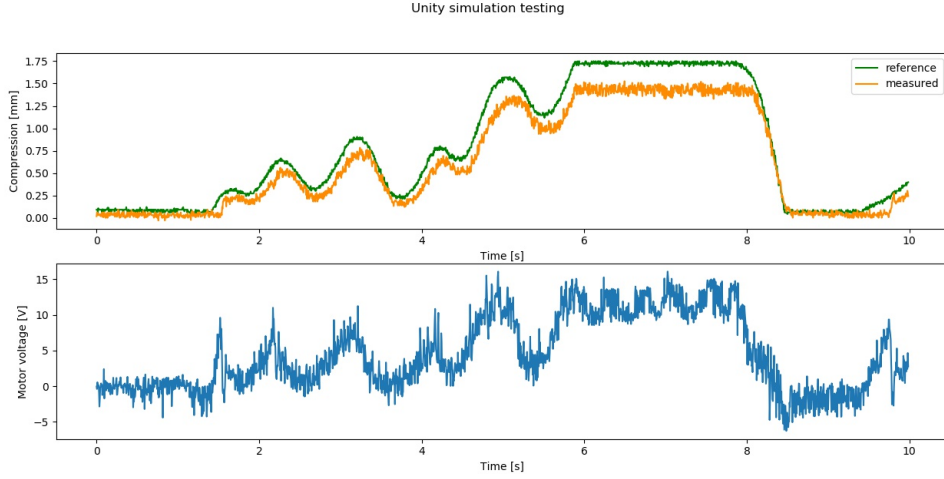


Figure 49: Command and feedback in Unity with P-controlled game controller (wall-blocked).

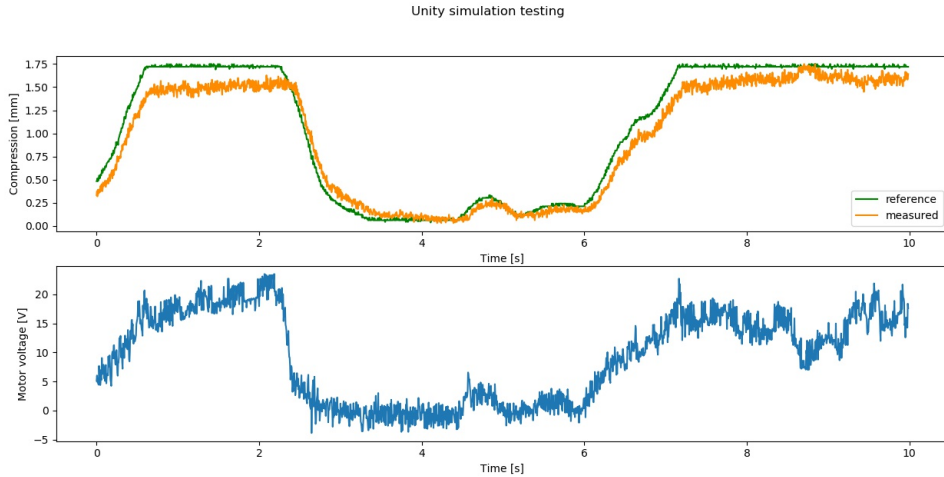


Figure 50: Command and feedback in Unity with PID-controlled game controller (handheld).

communication frequency of 250Hz).

However, there is no latency perceptible, neither when sending the commands, nor when receiving the feedback. This simulation-only test shows that the latency reported in the previous section does not stem from the implementation of the series elastic actuators and justifies the choice of this actuation system.

The tracking performance is good for both P and PID control schemes and the feedback feels intuitive. The transparency of the controller is better than in the experiment with the real robot and even the maximum output force could be achieved when driving over the steep slopes of the environment. The range of the output force is appropriate for the desired feedback. Since there is practically no friction in the setup, a very high force fidelity can be achieved. Obstacles or slopes can be felt individually and intuitively on both sides.

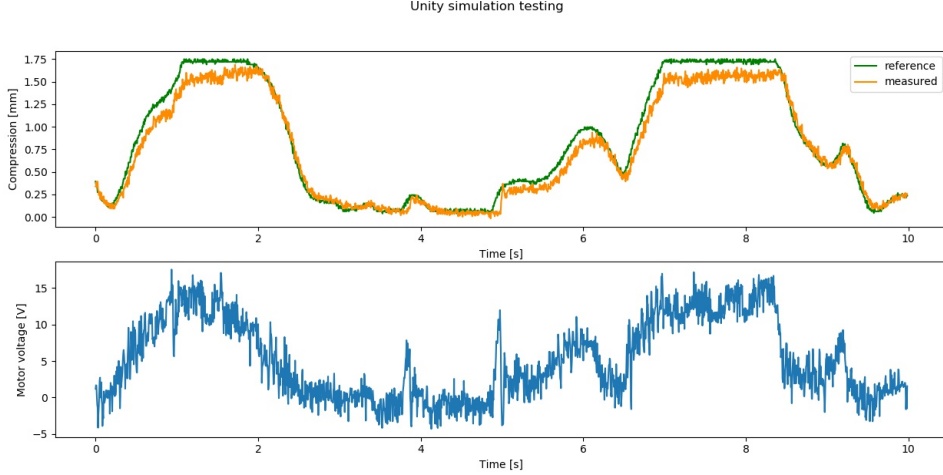


Figure 51: Command and feedback in Unity with PID-controlled game controller (wall-blocked).

5.16 Overall Evaluation of the Game Controller

Overall, one can say that the controller has achieved the performance requirements stated in the beginning of the project (section 1.7).

The advantages of using SEAs are mostly the increased maximum output force and the decreased weight (VCMs tend to be very heavy due to the magnets). A drawback however is the size of the controller. The controller has been designed with several margins for dimensions and distances, leading to this bulky setup. If necessary, the design can be optimized in future work, which would result in a much smaller controller.

Both control schemes (SEA and VCM) are straightforward and the output force can be controlled easily.

The generic disadvantages of SEA implementations are the control speed and reaction time of the mechanical setup. However, as it has been shown in both testing environments, the mechanical response time is not the bottleneck for this particular application.

Designator	Requirement	Achieved	Unit
Output force	> 10	10.8	[N]
Response delay	< 160	50	[ms]
Maximum size	$< 200 \times 150 \times 100$	$220 \times 110 \times 70$	[mm \times mm \times mm]
Maximum weight	< 0.6	0.55	[kg]

Table 7: Controller performance requirements and achieved performances.

Even though the maximum output force is high enough to give a good feedback, it can be further increased. The motors that are currently used are not capable of compressing the springs to their maximal deflection. Therefore, it is enough, to switch out the motors to have a higher torque. When doing so, it should be verified, that the control speed of the motors do not affect the overall response time.

From the psychological points of view, the only shortcoming is the feedback direction, which is application-specific. For this reason, and in order to write and test the parameter choice suggestions for future research projects based on the current findings, a second controller has been designed.

6 Design Suggestions

This section provides a guideline for important design parameter choices, if one wants to design a similar haptic feedback controller based on series elastic actuators. It is mainly based on the findings from the game controller but also includes the main results of the second controller, called yoke controller.

Since the design strongly depends on the target application, it is assumed to use the controller for robots similar to the Topy robot.

6.1 Software and Control Choices

In order to introduce no latency for control commands, it is important to have a high communication speed with no delay. In the current Arduino setup, one can decrease the command delay by using interrupts for the joystick commands. For immediate feedback, one can implement a feedforward control scheme that is fed from the joysticks' positions directly to the stimulators.

The bottleneck of this setup was the fixed communication frequency of the Topy robot of maximum 5Hz. Due to the small changes of the feedback value, this operation frequency is still acceptable⁶. However, if one expects a highly fluctuating feedback, a higher communication frequency has to be opted for.

The suggested control scheme is a normal proportional controller, mainly due to the fact that it is bothersome to fine-tune the PID gains and because the PID performance benefits do not outweigh the performance of the P control scheme.

For haptic applications, it is suggested to have a motor control rate of at least 1kHz which is the limit for the Arduino. If one opts for higher control frequencies, it is recommended to switch to an *Mbed* device or similar devices.

The joystick to feedback (ie. input to output) latency is around 300ms. To reduce this latency, one can think about implementing a feedforward from the joysticks in the control algorithm. The theoretical latency has been evaluated in the Unity test environment. However, if one is looking for a in-depth analysis of the latency, a more thorough testing is suggested. Also, it seems unavoidable to alter the Unity test software in order to gain access to main parameters, such as the terrain details (ground truth inclination), reception of commands or sent feedback both on the simulated tank-side.

6.2 Mechanical Parameters

One of the first mechanical design choices is the design of the controller itself. The PlayStation-inspired controller has been chosen for consistency with the previous research, but also for the fact that most conventional controllers are based on this design. It is not required to copy this design, which is why a different approach has been chosen for the second controller design.

The feedback direction is target-application-specific and results from the design. For the desired application, it is recommended to have a direct movement-opposing force, as it is the case for the yoke controller design.

The weight only plays a minor role and any weight seems to be acceptable, as long as the operator can comfortably handle the controller.

The target point of contact with the user's palm is between the Mars and Venus region⁷. This area is sensitive enough and can have a typical indentation of 5mm which needs to be taken into account when calculating the necessary stroke of the stimulator. The palm pads' areas should measure around 5 to 10cm².

⁶This has to do with the fact that the current can only change continuously and comparably slowly in the two crawlers. For other applications this cannot always be assumed.

⁷accessed (2018, July 26th), <https://www.yourchineseastrology.com/palmistry-mounts.htm>

Based on the findings from the previous study in the same laboratory, the handheld controller can successfully overcome the issue of common haptic interfaces where the reaction forces have to be dealt with. It has been shown that the device does not have to be grounded in order to only create the feeling of being pushed and not pulled.

Another important element is the spring system. It is recommended to have a symmetric arrangement with springs of equal spring constant. In addition, one should assemble the springs with utmost precision to ensure symmetry, in order to reach linear behavior during compression. The length of the springs does not seem to be very important, as long as the compression is constrained to the perpendicular axis only. With the tested springs it has been concluded, that a length of 10mm is at the limit of the acceptable range, but shorter spring lengths are suggested. Shorter springs also result in a more compact design which is generally favorable.

Testing different deflection ratios has shown that the target stroke (not necessarily full compression) must be achievable and that it is better to have a margin if one wants to change the motors used to increase the output force.

The spring coefficients can vary and tests between 2 and 24N/mm have shown promising results⁸. The designer can choose the springs according to the desired output force and the target compression of the springs.

The motors greatly influence the performance of the controller. The reduction ratio should be high enough to guarantee the target output force, while ensuring the desired control speed. The target output torque can be used to calculate the output force approximately. However, one should keep in mind that some energy is lost in friction and efficiency of the motor and gear assembly.

Furthermore, non-backdrivability in the motors can lead to a more energy-efficient system, since the voltage level only has to be provided to load the springs and the energy is then stored in the compressed springs, being blocked by the irreversible gears of the motors.

6.3 Electrical Parameters

The electric components that have been used are mainly the potentiometer for the joysticks and the photoreceptors for distance sensing.

The photoreceptors have very different characteristics and all thresholds need to be identified individually. Furthermore, the output-to-distance function is not linear for a big range of distances and the sensitivity does not stay constant. If a high performance is expected from the controller, it is recommended to find a different solution or a better performing sensor.

Furthermore, it is advisable to filter the motor commands to convert the Arduino output PWM to a more steady voltage level, to protect the amplifiers from overfitting the signal.

Further, it was necessary to implement a voltage follower (a simple operational amplifier with unitary gain) in order to reduce interfering effects on the distance sensors. The sensors namely showed a very strong correlation with the reference signal given by the wave generator.

⁸These results stem from subjective evaluation of the output force, as well as the theoretical calculation of the transfer function.

7 Design Phase of the Yoke Controller

7.1 Working Principle

The second controller uses a cam follower principle as actuation transmission. A mechanical cam is attached to the motor shaft, which pushes a lever. This lever is directly linked to the springs and the palm pads. The SEA system stays globally the same as in the first controller, only the transmission principle has changed. In this case the motor can only provide positive forces, which leads to a compression of the springs. It cannot change the springs' decompression speed, even if a negative voltage is applied. This is because no mechanical pre-load has been applied to the springs and the follower (lever) only touches the cam with no linkage.

7.2 Design and Parameters

When designing this controller, the design of an airplane yoke has been used as a model. Therefore it is from now on referred to as the yoke controller. The first draft of the design can be seen in figure 52.

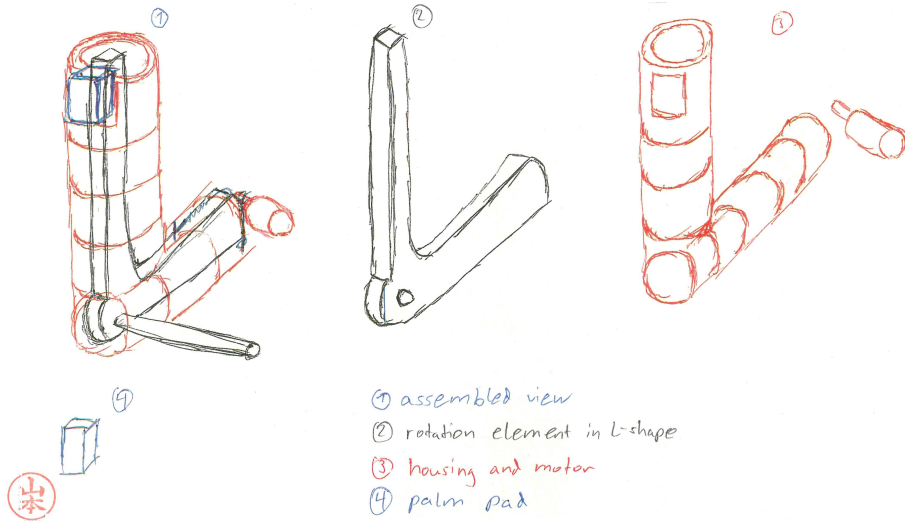


Figure 52: First draft of the yoke controller.

In order to have a nice fit to the palms, the circumference has been chosen to be close to the airplane yokes' or conventional car steering wheels' circumferences. The joystick's position is such that the stimulator touches the same area of the palm as in the previous controller and research (Venus and Mars area of the hand). This time, the feedback direction is perpendicular towards the user, which ensures a more intuitive feeling for the desired application.

The most important parameters in this system are the length of the lever and the springs. For the prototype, the lever's length has been fixed to roughly 100mm and a set of four springs with 1N/mm each have been used. Their length is 10mm and they have an allowable deflection ratio of 40%.

The stimulator's area is kept almost the same as in the previous design, namely 7.5cm².

The motors play an important role again. For this design, the motors with the reduction gear of 33:1 have been implemented.

It has been calculated that an output force of 10N can be achieved if the rotation cam has a radius of 5mm and the lever has a length of 90mm between the axis of rotation and the motor, and 60mm between the axis of rotation and the springs.

In order to achieve a bigger output force, a smaller radius of the rotation cam can be chosen.

The angle of the rotational L that was targeted is 10° for the full stroke. With the current design of

the rotation cam, the motor has to move roughly 100° to achieve the full stroke. With the motors characteristic turn speed, the palm pad control speed of 110ms for the full stroke can be calculated. This corresponds to a speed of 10cm/s.

For designing the rotational cam part, a spiral-like freeform has been drawn to keep the angle-to-distance ratio as linear as possible.

The operational distance for the photoreceptors is between 5.5 and 10mm. As before, the operational range of the photoreceptors can be identified.

	Sensor reading MAX (rest)	Distance (rest)	Sensor reading MIN (compression)	Distance (compression)	Max output force
Left side	780	10.5mm	550	5.5mm	20N
Right side	763	10mm	600	5.5mm	18N

Figure 53: Identified operational range for the photoreceptors in the yoke controller.

The 3D model of the left-hand side yoke-based controller can be seen in figure 54. To see the inside of the controller, the cover has been removed. For assembly, three sets of screws and nuts are necessary, making it easy to assemble and take apart. Moreover, this design is smaller in volume than the game controller. It is therefore more slender, lighter, cheaper and faster to manufacture.

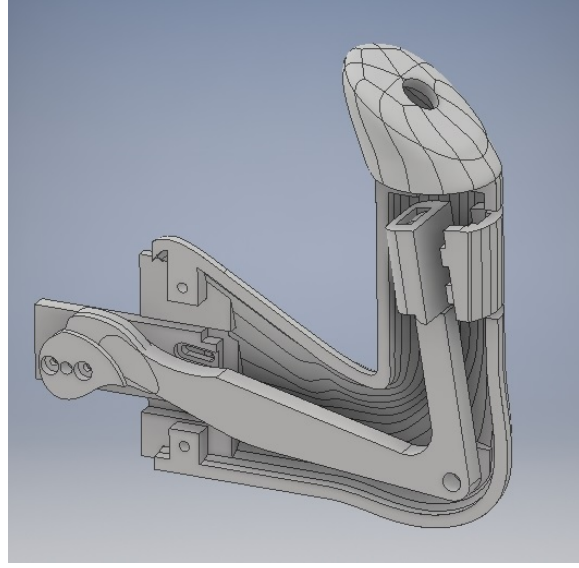


Figure 54: 3D model of the left-hand side controller with a removed cover.

In this design, the feedback motion is perpendicular towards the user and opposing the direction of motion. In fact, there is a slight angle at which the force is acting, due to the rotational design in the controller. However, due to the large lever, this effect can be neglected.

7.3 Printed Version

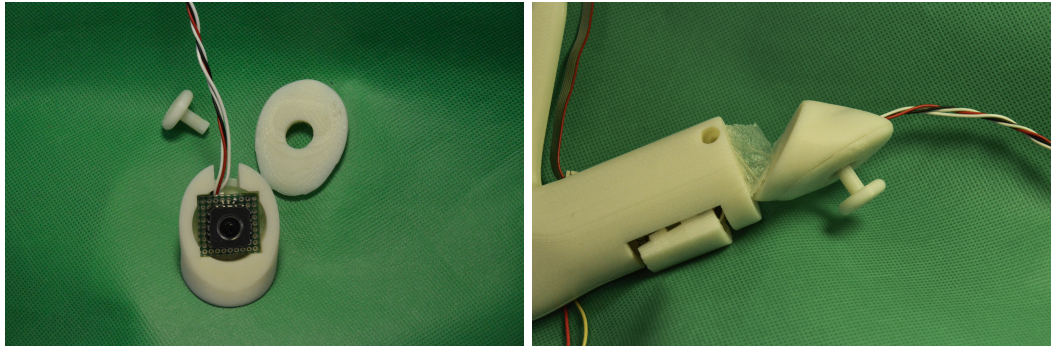
The printed version of this controller can be seen in figure 55.

As it can be seen in figure 55b, the controller consists of very few parts. For one, there is the joystick mount, which has preliminarily been taped to the cap of the casing of the controller. This can be seen in figure 56.



(a) Yoke controller front side. (b) Yoke controller opened. (c) Yoke controller back side.

Figure 55: 3D printed yoke controller assembled and with cover removed.



(a) Joystick mount disassembled. (b) Joystick mount taped to casings cap.

Figure 56: Joystick mount for the yoke controller.

Then there is the lever element, referred to as the rotational L (black part in figure 55b), to which the spring plate is attached. The springs are on one side glued to this spring plate and on the other side glued to the palm pad. A slot within the palm pad serves as a housing chamber for the photoreceptor and its circuit, thus allowing to measure the distance to the spring plate and therefore the compression of the springs.

The motor is screwed to an element called the motor plate, which is attached to one side of the controller casing. The oblong holes in this plate are used to adjust the distance of the motor with respect to the lever. Therefore the output force and control speed can be fine-adjusted.

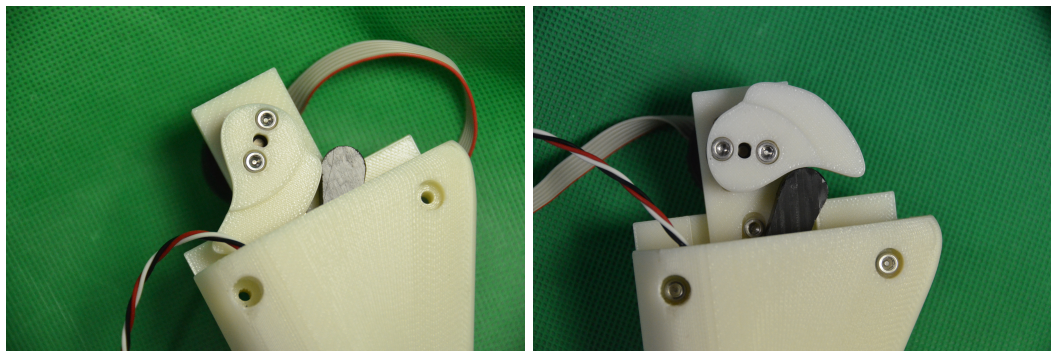
Another important element is the rotational cam. This is directly attached to a shaft collar, which is fixed to the motor shaft with two set screws.

The rotational cam actuates the rotational L by simply pushing it. This is subject to frictional effects and can have some impact in the final performance. However, this was a risk that has been accepted with the design choice.

Figure 57 shows the assembled version of the rotational cam.

As it can be seen in this figure, the rotational cam can rotate and actuate the lever until the lever is blocked by the walls of the controller itself (figure 57a). However, if a negative voltage is applied, it rotates into the other direction, which causes it to lose contact with the lever (figure 57b). Since it is only blocked by the rotational L on the other side (ie. -180° rotation of the cam), this may cause a long delay in operational mode. This phenomenon has been explained in chapter 8.8 and is termed the build-up latency.

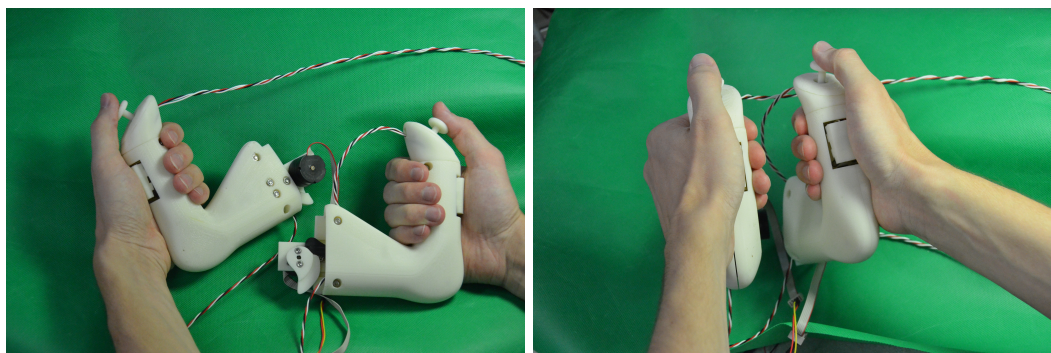
When the controller is in use, the two sides can be held individually and are not linked to each other. This allows for more flexibility and simplicity of use. Figure 58 depicts this situation. The area of



(a) Operational mode: Cam pushing the rotational L.
(b) Build-up latency: Back-rotation until blocked by rotational L.

Figure 57: The rotation cam element (black-side view).

contact with the hand, as well as the feedback direction can also be seen.



(a) Side view.
(b) Front view.

Figure 58: The pilot controller in use.

8 Testing of the Yoke Controller

8.1 Test Setup

Similar to the test setup described in section 5.3, the yoke controller has been tested. The major changes that have been made were the threshold values of the photoreceptors and the gain values. Again the Function Generator **SG-4115** has been used to create a reference signal and the same frequency range has been tested. The palm pad has been blocked by a C-clamp. Due to the fact that the controller is virtually identical on both sides, only one side has been evaluated. For the sake of the argument, we shall call the tested controller the left side.

8.2 Tracking Behavior of the P-Controller

The tracking behavior of the P-controlled ($K_P = 10V/mm$) yoke controller can be seen in figure 59.

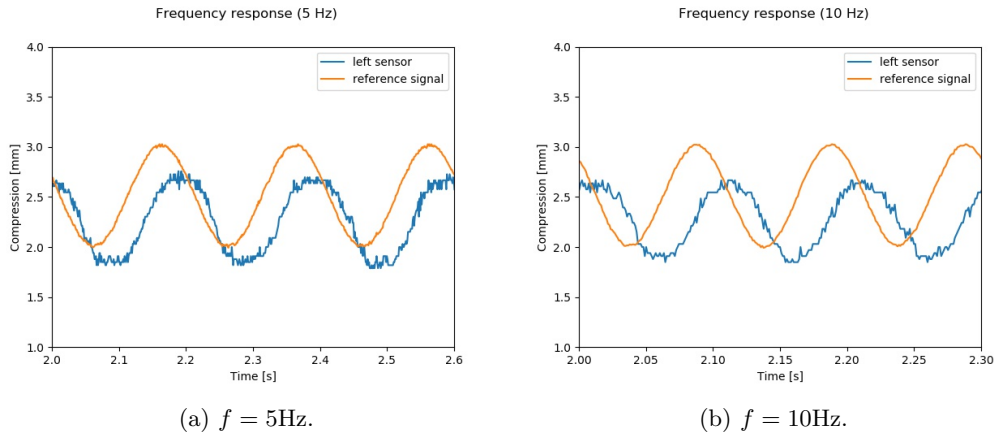


Figure 59: Tracking behavior of the P-controller ($K_P = 10V/mm$) for different frequencies.

Analogously to the previous testing, the tracking performance has been studied for different reference input. The test cases where a sine wave as well as a square wave, for both, low and high amplitude. The results can be seen in figure 60 and 61. Due to the nature of the P-controller, the low reference values cannot be tracked well enough for a low gain. This can be seen in figure 60 on the left-hand side. In order to show that the software control is not the problem, the motor voltage has been plotted as well.

This also shows that there is a non-negligible static friction in the system, since the motor voltage of up to 10V does not result in any movement of the cam.

For a higher gain, small and high reference values are tracked, albeit with a time offset. The trade-off for this parameter tuning is the speed and stability in favor of controllability of the output force.

8.3 Bode Diagram

Again, the results of the frequency response testing can be plotted in a Bode diagram. In figure 62 one can see that the tracking is acceptable for low frequencies. The gain does not fall below -4dB until it reaches the resonance frequency around 8Hz . The cut-off frequency is around 8Hz . The phase lag starts at -30° and reaches -200° for the far end of the tested frequency range. The anomaly at 100Hz can be explained with the noise in the distance sensors, that becomes non-negligible for such small displacements.

The identified phase lag at 1Hz corresponds to a delay of 80ms . This can be confirmed by the

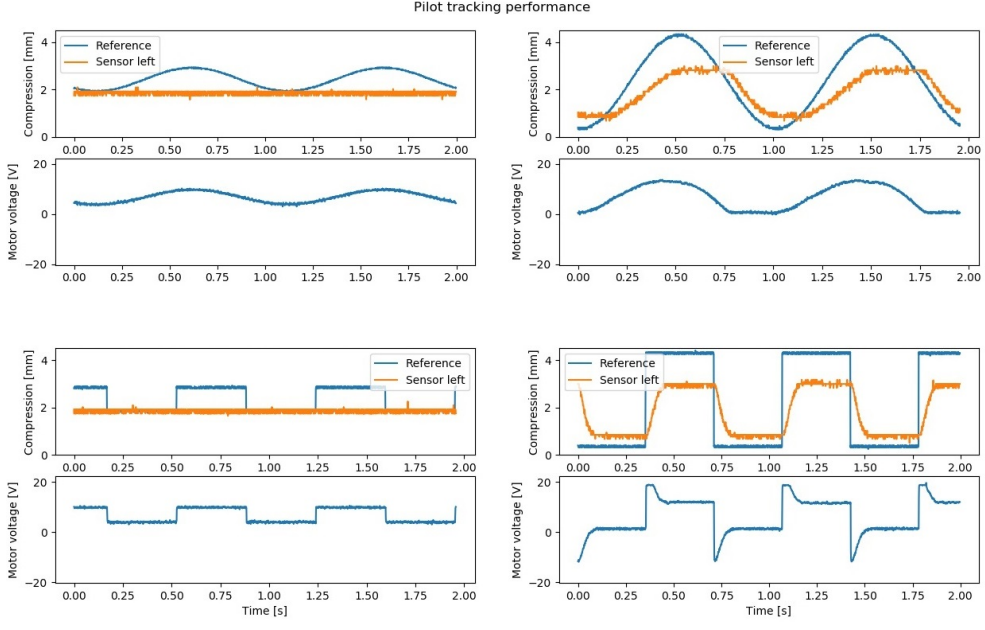


Figure 60: Tracking performance for different reference signals with a $K_p = 5\text{V/mm}$.

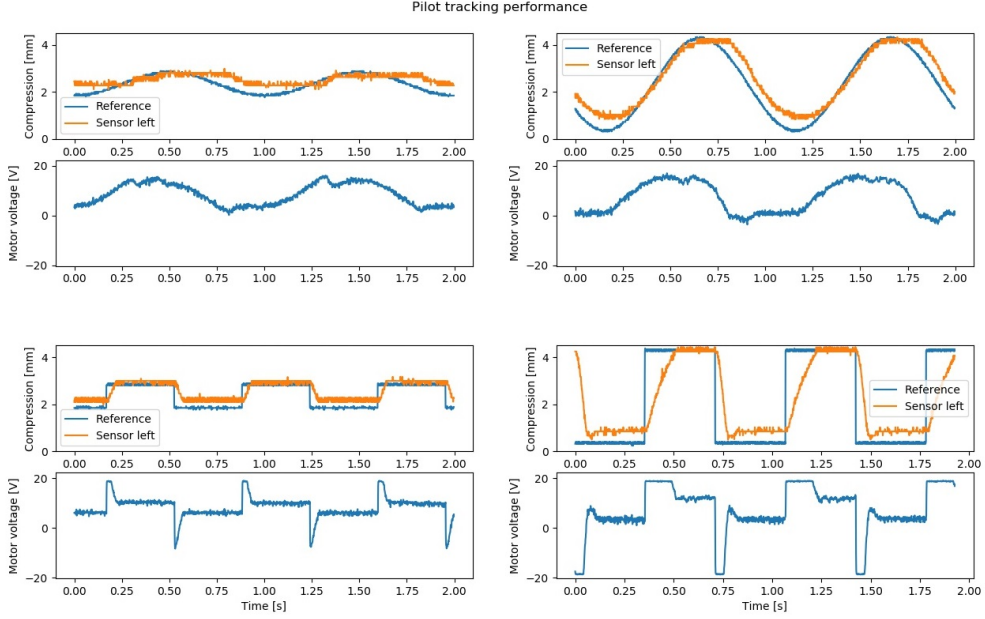


Figure 61: Tracking performance for different reference signals with a $K_p = 15\text{V/mm}$.

sine wave tracking performance in figure 61. The square wave confirms this delay only for small to medium compression references (ie. up to 2mm).

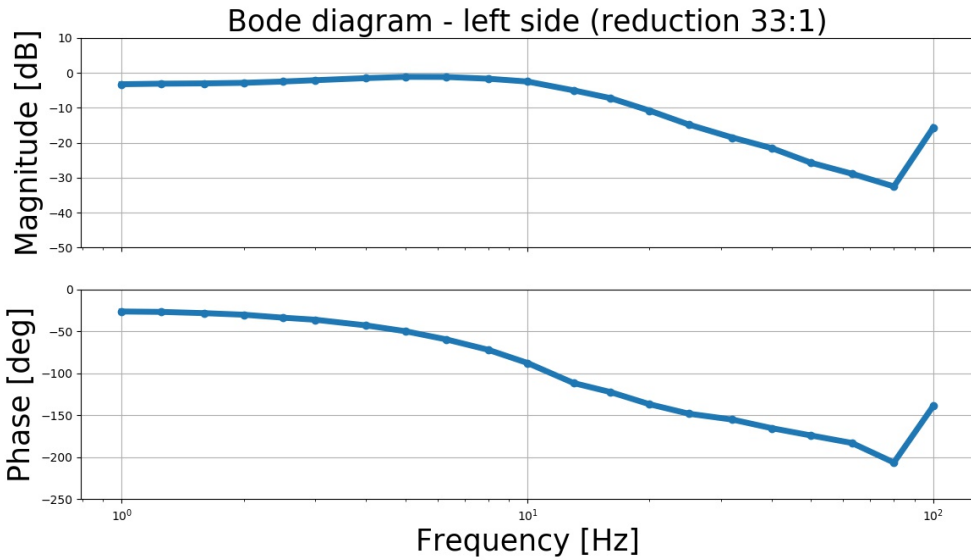


Figure 62: Left-hand side, Motor reduction ratio 33:1.

8.4 Discussion of P-Tracking

As explained in the previous testing set of the first controller, it has been discussed that the PID controller does not significantly increase the performance of the feedback. For this reason, only a P-controlled yoke console has been tested in this case.

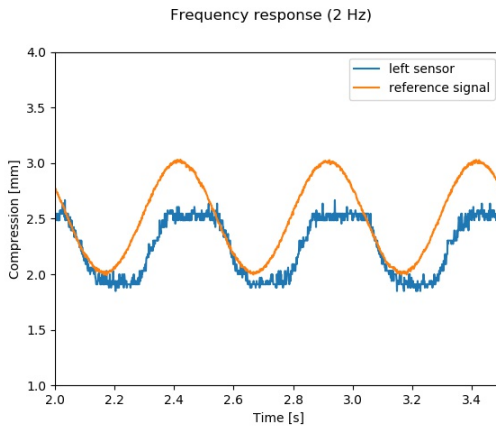


Figure 63: Tracking behavior of the P-controller ($K_P = 10V/mm$) for 2Hz.

In figure 63 a saturation behavior arises for very low frequencies. One could argue, that this stems from the fact that the reference value that has been fed into the system was too high and the motors' capacities have been saturated⁹. However, this does not apply here, since the maximum reference of 5mm has been measured as the steady-state displacement resulting from 20V motor input voltage. Therefore, it should theoretically be achievable. From this, one can conclude that there either is a non-repeatability in the system, the system shows a non-linear behavior, or a

⁹Note, that for the frequency response analysis, a smaller reference signal has been used.

combination of both. Additionally, one can also argue that there is a significant difference between steady-state and dynamic operation for low frequencies.

Furthermore, due to the length of the springs, and since the compression procedure of the springs is not guided, it seems plausible to assume that the palm pad's movements are not completely perpendicular to the spring plate. In order to understand this issue, figure 64 can be studied. Therefore, the distance does not change linearly and the full compression cannot be achieved all the time. For the test setup a C-clamp has been used in order to block the palm pad. Since this produces only a punctual counterforce, this effect is magnified. In operational mode however, it is expected to have a more linear behavior, since the palms of the user can create a more uniformly distributed counterforce.

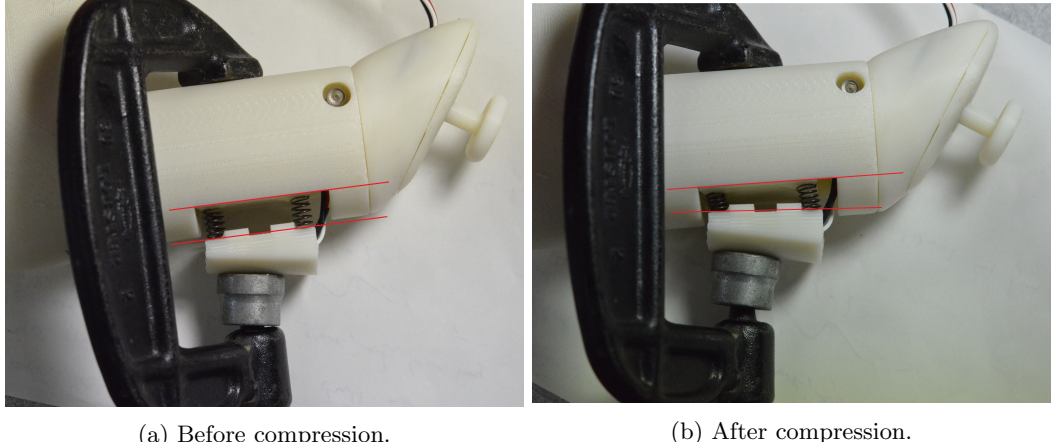


Figure 64: Indicated angles of palm pad with respect to spring plate to show the C-clamp effect.

In figure 63, it is visible, that the real compression is constantly slightly below the reference value. These findings have been confirmed in the Bode diagram from figure 62. This is due to the implementation of the P-only control scheme with no integral part that could remove the steady-state offset.

However, since the steady-state offset between reference and tracking is of less than 0.2mm (ie. 0.8N) it is negligible and therefore, an implementation of integral and derivative part does not seem necessary.

For the right-hand side, it is assumed that the tracking behavior stays similar and the gains shall be identical.

8.5 Hysteresis Effect

As it has already been mentioned, there is an expected hysteresis effect which causes a non-linearity and therefore also a latency in the system.

This hysteresis can be shown by simply plotting the input to output tracking for a linearly increasing reference. In theory, a perfect controller should have an identity function where $x = x_{ref}$, the output matches the input. However, for this system this is not the case. In fact, there is a hysteresis effect which does not map a single x value to a given x_{ref} value. The effect of this can be seen in figure 65.

From figure 65, one can see the counter-clock wise rotation of the hysteresis, which is an indicator for the phase lag. In figure 65a the measured distance reaches values below 0mm which is caused by non-perfect threshold identification of the photoreceptor values, and has no impact on the performance at this point.

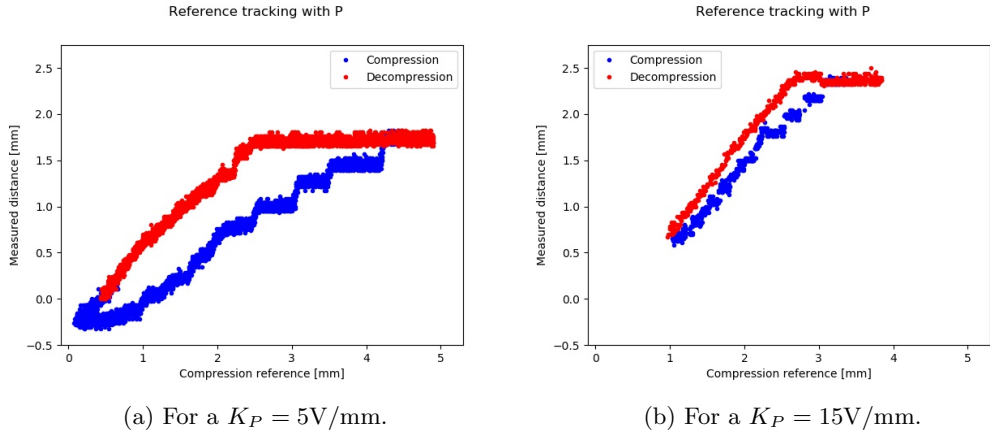


Figure 65: The hysteresis effect for input-output tracking performance of different gains.

Another key conclusion that can be drawn from figure 65b is, that the tracking is almost perfect when decompressing the springs (almost identity function). While in the other direction (compression), there is a slight offset, for example when 3mm is given as a reference, only 2.5mm can be achieved. This shows that a gain value of 15V/mm leads to a better tracking of the reference value, at least for the decompression direction. Additionally, there is a horizontal line visible for references between 3mm and 3.8mm.

This horizontal line seems to be the maximal achievable compression for this setup. This is where an increase in voltage does not result in a change in compression of the springs. Also, when testing, the voltage for high compression references (ie. 3.7 - 3.8mm) has been saturated at 20V, yet again indicating the maximum achievable compression.

In the case where the weaker gain has been tested, the tracking performance is worse. The de-compression slope is not optimal and neither is the one for compression. Already at mid-distance references, the output is far from what it should be. Also, with a weaker gain, the hysteresis effect seems to have a bigger impact.

Another effect that can be observed, is that the compression happens step-wise. It is assumed that this is due to the friction present between the rotational L and the cam, or the friction in the reduction gear. Strangely enough, this phenomenon is not visible in the other direction.

8.6 Other Non-Linearities

Apart from the hysteresis effect, there are other non-linearities present in the system. Based on the fact that the springs are decompressed more easily than compressed (due to the naturally occurring spring force, that tries to keep the compression at 0mm), the slope of the compression is less steep than the decompression and happens more slowly¹⁰. This will result in a skewed sine wave for a regular sine reference.

As a result, this impacts on the analysis, notably in the Bode-diagram. The sine interpolation of the measured distance is shifted to the right, due to the left-skewness.

This leads to an additional latency in the system. Even though this phenomenon is present in any reference signal, the psychological effect has not been taken into account in this work. It is expected though, that the slower compression will be felt as a normal delay.

¹⁰Even though this is linked to the hysteresis effect, they are not the same and another issue arises, which has to be treated individually.

In addition to that, the lever has been created using an 8mm thick poly-acetal (POM) plate. Even though this material shows excellent specific strength and specific stiffness properties[38], the material is deforming towards the direction of actuation. This non-infinite stiffness behavior induces further non-linearities in the system, that are difficult to cope with. The measured deflection at the distance of the spring plate in the cantilever-like rotational L is 1.5mm for 20N. These effects however, have not been taken into account in this work.

8.7 Motor Choice

For this yoke controller the motor with the lower reduction gear ratio has been used. This means that it is faster than the other motor in terms of tracking speed. Since the cut-off frequency from the frequency response analysis is already lower than in the previous controller, and given the fact that the output force is high enough (according to the requirement specifications in the beginning of this work), this motor seems more appropriate.

In fact, the cut-off frequency is very close to the maximum robot communication speed. To guarantee that the actuation system is not the bottleneck of the control speed, one can consider motors with even lower reduction ratios.

8.8 Performance Evaluation

The yoke controller has also been tested on the real robot. The key design difference from the first controller is the fact that the motor cannot decompress the springs faster than their natural decompression speed. When a negative voltage is applied to the motor, the rotation cam will just rotate the other way, until it is blocked by the structure of the controller. However, if one wants to increase the speed of this controller, and especially not introduce a latency if the rotation cam has traveled all the way back, for instance, a pre-load is recommended. From now on this latency will be referred to as the initial build-up latency.

8.8.1 Latency

For now, one can neglect the build-up latency, as the rotation cam stays in contact with the lever during current feedback operation with non-zero feedback (the crawler currents are never really zero).

In this operation mode, the same analysis has been done as for the previous controller. Figure 66 shows the reaction and latencies of the real robot current, the desired spring compression and the real measured compression with respect to the joystick commands. The color coding is the same as in figure 45. This time however, it seemed more difficult to find the right points in time, since the signal to noise ratio of the measured spring compression has decreased.

However, the latencies can still be analyzed. Again, the robot needs a long time to start up after the initial forward commands. 0.4s after sending the signal, the robot's current starts to increase. This is only detected and used as a feedback 0.7s after the commands have been sent. Almost 0.93s later the distance sensors measure a compression of the springs. This delay is partially due to the build-up latency that has been described earlier.

When the stopping signal is sent, the user feels a drop in feedback force with a delay of roughly 0.6s. For completeness, the entire data can be seen in table 8.

The mechanical delay, measured between the moment when the desired compression is received, to the moment where the compression is measured, is of roughly 0.3s. This seems to be much bigger than in the previous controller and is not satisfying the performance requirements. To be able to make a conclusion however, it is suggested to further analyze this delay, since only 5 data points could be measured.

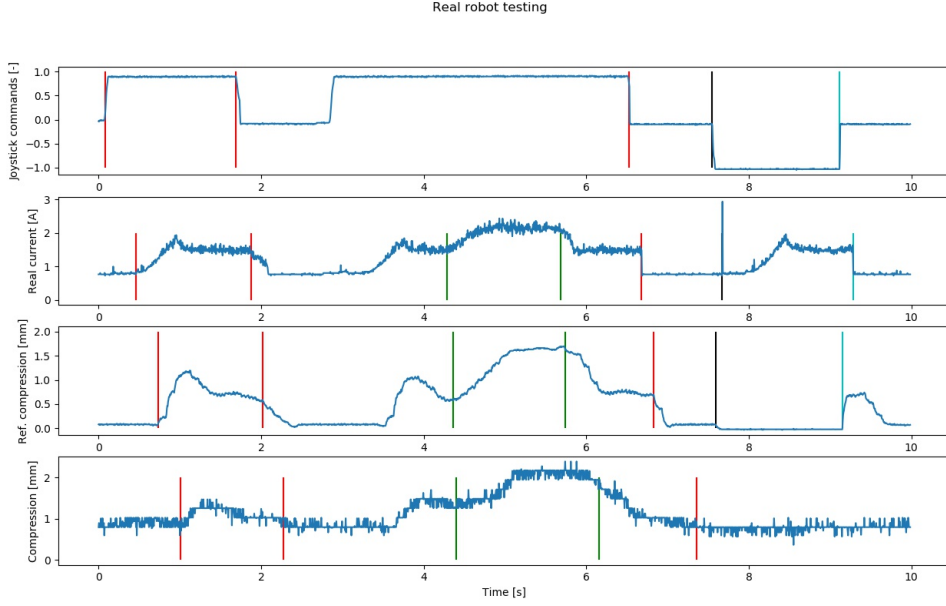


Figure 66: Command and behavior of Topy robot with P-controlled yoke controller.

	Start	Stop	Ext. force	No force	Stop	Back	Stop	Control
Joy-stick commands sent	0.08	1.69	-	-	6.53	7.55	9.11	P
Measured current in robot	0.46	1.88	4.29	5.68	6.68	7.67	9.28	P
Desired compression	0.73	2.02	4.36	5.74	6.83	7.59	9.15	P
Measured compression	1.01	2.27	4.4	6.16	7.36	-	-	P

Table 8: Latency table for sending joystick commands, current measured on the real robot, desired compression and measured compression. All values indicated in [s].

8.8.2 Transparency and Intuitiveness

When using the controller on the real robot, the time delay between sending the commands and feeling the feedback becomes non-negligible. Even though the feedback is perpendicular to the user, and the controller fits the hands and palms of the user smoothly, the feedback does not feel very intuitive.

When the build-up latency is neglected however, the system is perceived to be very transparent. The current can be felt in the user's palms, which gives an intuitive knowledge of the energy used by the robot.

8.8.3 Stability

In terms of stability there is no problem. The controller stayed stable in all tested situations and can resist shock or changes in the counteracting force of the user. As expected for this SEA type and implementation, stability is not an issue.

8.8.4 General Performance

The controller works, but the felt feedback is not intuitive, due to the initial time-delay that deteriorates the user experience. However, the design of the controller is visually more appealing and geometrically more appropriate for the desired tasks.

When tuning the sensor thresholds however, it is possible to remove the build-up effect and introduce a small constant feedback force even for a 0N force reference. In this setup, the controller feels very natural and the user receives the 2 degree of freedom information about the robot's state in an intuitive manner.

This controller has traded off speed of the actuation system in favor of high output force and therefore the latency has increased as well. For a better experience it is recommended to either implement a feedforward method to overcome the latency issues and create a pseudo-feedback, or to change some parameters in the system. For one, the springs can be switched out to a set of lower equivalent stiffness. Or the necessary stroke can be reduced by replacing the 10mm long springs by springs of 5mm in length, while doubling the spring constant. Alternatively, the motor can be changed to have a lower reduction ratio and higher control speed. Also, it is recommended to pre-load the rotation cam and link it to the lever, to fully get rid of the build-up latency effects.

8.9 Unity Simulation

When testing this controller in the Unity simulation, almost the same procedure has been used as in the previous testing part. The controller was held by the operator who navigated the robot in the simulated environment. Again the latency has been analyzed, in the assumption that all the latencies in this system come from the controller side and that the communication delay over the serial link can be neglected. Later, the transparency and intuitiveness of the controller have been evaluated.

8.9.1 Latency

In order to evaluate the latency of the mechanical setup coupled to the Arduino, the robot has been navigated in the landscape of the Unity simulation. The evaluated test case scenario is represented in figure 67.

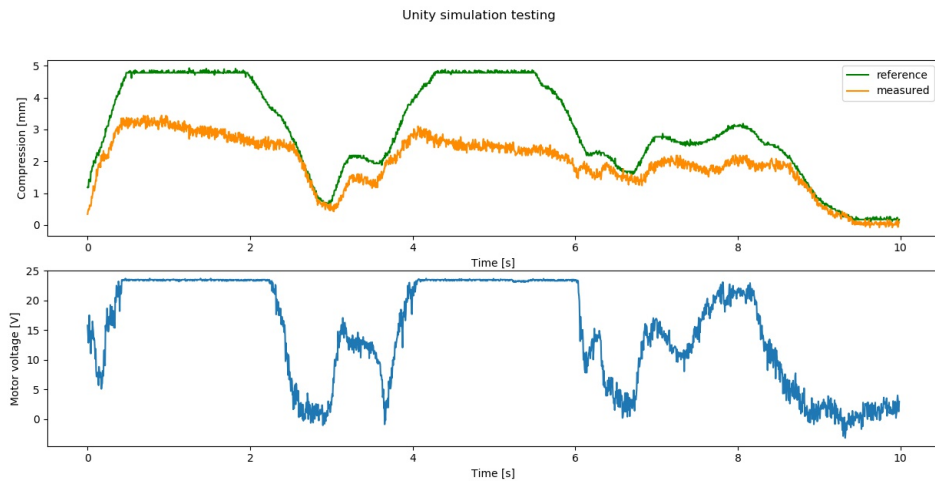


Figure 67: Command and feedback in Unity with P-controlled ($K_P = 10V/mm$) yoke controller (handheld).

When evaluating the test cases, it has been found, that the latency (between voltage level and spring compression) is of roughly 90ms.

Similar to the game controller, it has been observed that for a steady motor voltage, the compression oscillates. This is due to the fact that the user cannot provide an overall constant reaction force and

changes the grip from time to time. This makes it harder to evaluate the tracking performance of the controller.

8.9.2 C-Clamp-Blocked Unity Test

One of the weaknesses of the previous simulation-based testing was that the operator's hand behaves not only like a spring damping system, but also the hand's stiffness and damping coefficient can be varied by changing the grip. Tests have shown that it is nearly impossible to maintain an invariantly tight grip on the stimulator. Therefore, the environment has a significant impact on the tracking performance of the controller.

In order to remove this chaotic factor, the operator's hand has been replaced by a C-clamp blocking the palm pad. This results in a uniformly counteracting force and the performance of the controller can be tested individually. The test setup can be seen in figure 68.

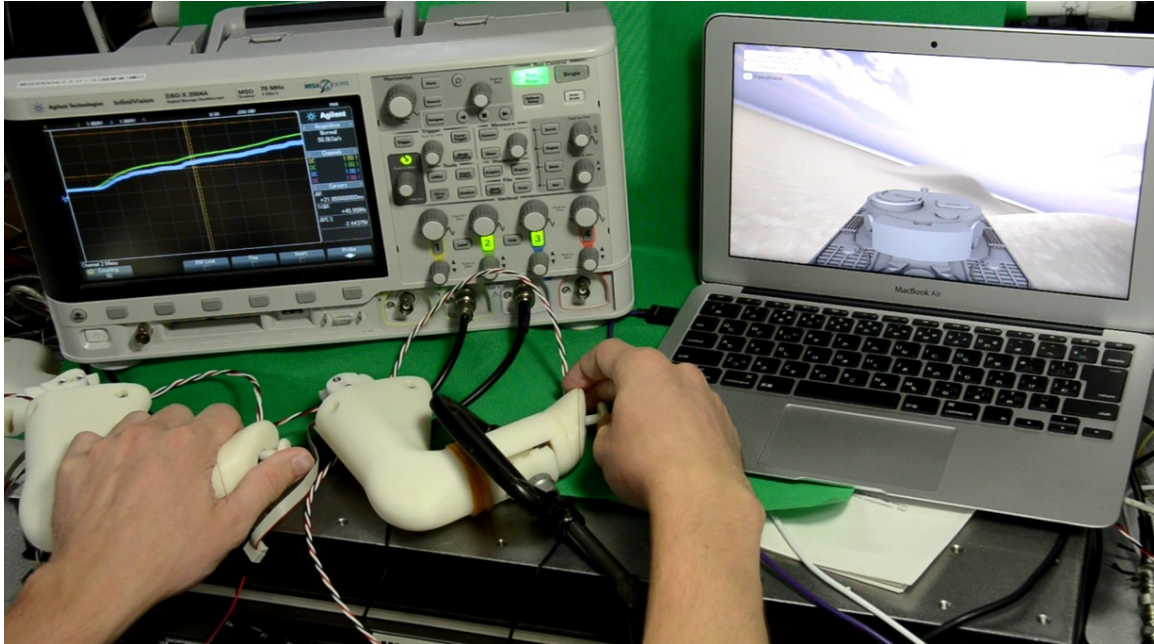


Figure 68: Unity test setup with C-clamp-blocked yoke controller.

This setup has been used to test compression and decompression, as well as oscillation references in the simulation and the results can be seen in figure 69.

In this graph it is visible, that the tracking performance is much better than when holding the controller in the hand. This shows that the gain has been chosen correctly in theory. Furthermore, one can conclude, that the unpredictability of the environment makes the output force difficult to control.

8.9.3 Unity Performance Evaluation

When using the controller in the Unity simulation, it has been shown that the right direction of the feedback is important for the feeling of the application. The perpendicular feedback and the high force fidelity (up to a high output force) give a good overall feeling. The feedback reference can be matched well enough, with only small oscillations. These are due to the fact that the user cannot maintain a constant grip throughout the testing time. This means that the output force changes, depending on the grip of the user.

The latency in this simulation-only test does not distort the transparency and the intuitiveness of

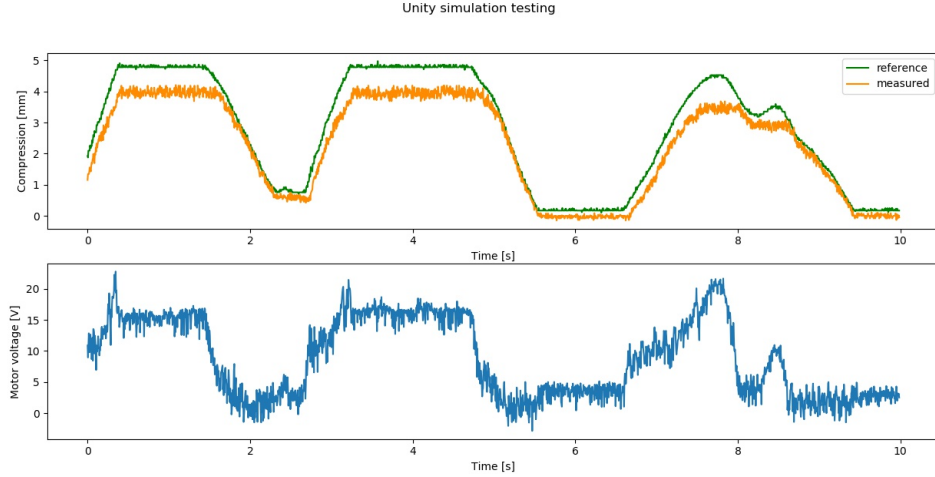


Figure 69: Command and feedback in Unity with P-controlled yoke controller (blocked by C-clamp).

the controller is quite good. The range of the output force could almost be fully exploited and the range again seems appropriate for the purpose of this application.

8.10 Overall Evaluation of the Yoke Controller

Again, the controller has satisfied the performance requirements.

The Bode plot has shown that a delay of 80ms is present for low frequencies. Testing in the real-world however, shows a much bigger delay of 300ms. Nevertheless, the tracking performance evaluation, as well as the Unity simulation have suggested a lower response time of 80 and 90ms respectively. This discrepancy mainly stems from the build-up latency and it can be removed by adapting the thresholds or implementing a mechanical linkage between lever and cam.

Furthermore, the maximum achievable output force is much larger than in the VCM system and the changes in force feedback can be felt very smoothly (high force fidelity).

The geometry and shape of this controller is very intuitive and fits the hand well enough. In addition, the separated left- and right-hand side allow relatively free movements of both hands and arms of the user. In a future research, it might be interesting to make the controller wireless and battery-powered to have two completely separated portable controllers.

Again, the Topy robot's communication speed is lower than the systems control speed. However, the major issue is the previously described build-up latency. Even though it happens very rarely, the perceived maximal latency can increase drastically. It is recommended to avoid this by coupling the rotational L and the cam (pre-loading).

The choice of the motors seems to be appropriate.

Designator	Requirement	Achieved	Unit
Output force	> 10	18	[N]
Control speed	—	9	[full stroke/s]
Response delay	< 160	90	[ms]
Maximum size	$< 200 \times 150 \times 100$	$155 \times 155 \times 50$	[mm \times mm \times mm]
Maximum weight	< 0.6	0.5	[kg]

Table 9: Controller performance requirements and achieved performances.

9 Discussion

This chapter summarizes the main results from the design and testing phases of both controller models. It is complementing the discussions and evaluations that have already been mentioned in the testing sections.

9.1 Game Controller

The game controller has shown promising results, especially in terms of output force and control speed. The frequency response analysis shows that the PID control scheme performs only slightly better than the proportional one. Hence, when choosing between the proposed control schemes, a proportional controller is advisable.

For low frequencies up to the maximum robot communication frequency, acceptable tracking behavior has been observed. Given the fact that the controller's performance strongly depends on a variety of parameters, the system can be seen as rather complex. Thus, the PID tuning was done in an experimental trial and error manner, which yielded only suboptimal gains. For improving the performance, a more thorough gain parameter search is advisable.

The controller clearly behaves like a second order system and shows typical characteristics, such as an asymptotic phase lag of -180° .

When coupled to the Topy robot, the main part of the latency is due to the communication delay and the robot's internal speed control. The controller itself does only account for an average latency around 80ms. This latency analysis was based on visual identification of rising and falling edges, which was subject to the system's noise. Therefore, it is recommended to conduct a more in-depth analysis to precisely identify the controller's mechanically induced delay.

The overall feeling and transparency has been evaluated in a real-world scenario, as well as a simulated environment. In both cases, the controller was able to produce the desired feedback, albeit with the aforementioned delay. The user successfully feels the overcome obstacles on both sides, even though the feedback direction is not perfectly intuitive.

The stability of the controller was guaranteed for all of the test cases.

This implementation of SEAs shows that this actuation system is no bottleneck for the target application, and justifies using elastic elements. The initially stated requirements concerning output force, weight and speed could all be met.

9.2 Theoretical Model

The theoretical model has been used to identify a parameter that was difficult to measure. This was namely the combination of the springs' damping coefficient and the friction effects.

The P-controlled frequency response matches the analytically anticipated data. When integral and derivative parts are implemented in the control scheme however, the data differs from the analytical results.

This is due to the discretization process and the effect of the low-pass digital filter that has not been modeled.

The theoretical model has mainly been used to analyze the built controller. For future research, the mismatch between experimental and analytical data can be studied, in order to use the model as a tool for fast gain identification.

9.3 Yoke Controller

The yoke controller has a more intuitive design and feedback geometry. The output force is even higher, as it has traded off its control speed. The springs' lengths yield a rather large stroke which decreases the control speed. Furthermore, testing has shown that the build-up latency has a big impact on the performance and it is thus recommended to link the rotation cam to the rotational L. The tracking performance of the P-controller strongly depends on the gain and reference values.

However, a constant delay at low frequencies has been observed for all gains. The cam principle introduces non-negligible friction effects which causes very poor tracking behavior for small gains. Furthermore, the non-linear hysteresis effect has been studied. For small gains this effect is stronger. These and further discussed non-linearities in the system make it difficult to evaluate the controller. However, the frequency response analysis suggests that the series elastic actuation system can be fast enough in the target frequency range. A target-specific trade-off between speed and output force has to be made. For this controller it is suggested to opt for higher speed rather than output force.

The latency of this controller is dominated by the build-up effect. This can be overcome by the proposed mechanical solution. The pure mechanical latency of this controller is only marginally higher than for the game controller. However, a more thorough latency analysis is prudent.

The intuitiveness of the controller and provided feedback was given not only in terms of feedback direction, but also output force and force fidelity. Obstacles of different sizes could be distinguished successfully. The stability was guaranteed, due to the design of the feedback system. The intuitiveness was impaired in some scenarios, where the friction caused step-wise motion and therefore step-wise changing feedback. This controller met the performance requirements, too.

9.4 Identified Potential and Applications

From testing the two different controllers, the importance of the feedback direction has become clear. For the target application, where the feedback should act as a pushing force, a perpendicular force towards the user is more intuitive. However, one may find other applications, where the feedback direction of the first controller (ie. pushing the hands outwards) is more appropriate.

An example for this could be in a handheld controller for navigating a drone. By implementing haptic feedback one can inform the operator in an intuitive way about external forces such as wind or wind gusts. In that case a combination of several directions might even be considered.

This type of haptic feedback does not necessarily have to be implemented in a remote control for mobile robots. As a matter of fact, haptic feedback can be useful in a multitude of applications. These application fields can vary from the manufacturing domain, where handheld tools can yield important information about the object being handled, over maneuvering vehicles, for example in construction site vehicles, where the feedback can indicate how much the load in an excavator's shovel or forklift weighs.

This haptic feedback system could also be implemented in a steering wheel of a car, to warn the driver about objects being too close to the car, to overcome the lateral blind spots.

10 Conclusion

This work has shown that a haptic feedback controller based on series elastic actuators is, without question, accomplishable. The designed and tested controllers were successful, not only in terms of output force, but also in terms of control speed (response delay) requirements and transparency expectations.

Key elements in building an SEA-based haptic feedback controller have been analyzed and studied. Valuable insights have been gained throughout the iterative design and building phases of two different controllers. Based on this, design suggestions were discussed for future research projects in the same environment setting.

The controllers have been tested extensively and, albeit proven to work, weaknesses in design and control have been identified. To overcome these, individual solutions have been proposed.

For future research, it might be interesting to study the valid ranges from which the setup parameters can be chosen, in order to facilitate the design process. To create a full design framework, a more thorough testing is advisable.

Tokyo, 17th of August

2018



List of Figures

2	Trend of published papers containing the keywords ' <i>haptic feedback</i> '	1
3	Developed controller in previous research[11].	3
4	Target feedback force and reaction force indicated in user's palm.	4
5	Control scheme for the haptic feedback system.	8
6	Discarded idea: Car-jack.	8
7	Discarded idea: Linear actuator.	9
8	Discarded idea: Toothed bar.	9
9	Discarded idea: Wedge.	9
10	Discarded idea: Hydraulic or pneumatic.	10
11	Accepted idea: Centric shaft.	10
12	Accepted idea: Cam follower with eccentric shaft.	11
13	Initial schematic of the actuation design.	11
14	3D model and rendering of the game controller.	12
15	Actuation system with legend (and top cover removed).	12
16	Joystick to command conversion with indicated dead-zone.	13
17	Photoreceptor circuit.	13
18	Operational range of photoreceptors with springs at rest and in full compression.	14
19	Schematic of the spring system setup.	15
20	Printed and assembled game controller.	16
21	Simplified mechanical schematic of the actuation system with the stimulator (m_2).	17
22	Block diagram with two different transfer functions.	18
23	Complete block diagram relating the output Δx to the input Δx_{ref}	21
24	Bode plot comparison of experimental data of the P-controller and analytical transfer functions for different spring damping coefficients (b_{sp}).	22
25	Bode plot comparison of experimental data of the PID-controller and analytical transfer function for $b_{sp} = 100\text{Ns/m}$ and $b_{sp} = 300\text{Ns/m}$	23
26	Bode plot comparison of experimental data of the PID-controller and analytical transfer function for $b_{sp} = 100\text{Ns/m}$ and $b_{sp} = 300\text{Ns/m}$. The derivative gain is $K_D = 24.7\text{Vs/mm}$	24
27	Bode plot comparison of experimental data of the PI-controller and analytical transfer function for $b_{sp} = 100\text{Ns/m}$ and $b_{sp} = 300\text{Ns/m}$	25
28	Bode plot comparison of experimental data of the P-controller and analytical transfer function for different spring coefficients (k_{eq}).	26
29	Topy robot for real-world controller test setup.	27
30	Topy controller.	27
31	Hardware connection schematic.	28
32	Graphical user interface written in Processing.	29
33	Complete system scheme of the robot in its environment and the user.	29
34	Control scheme for the frequency response analysis.	32
35	Tracking behavior of the P-controller for different step response input.	32
36	Analytic unit step response of the P-controller.	33
37	Tracking behavior of the PI-controller for different step response input.	33
38	Analytic unit step response of the PI-controller.	34
39	Tracking behavior of the P-controller for different frequencies.	34
40	Bode diagrams for the two motors.	35
41	Bode plot for both motors with same reduction ratio, P-controlled.	36
42	Tracking behavior of the PID-controller (for gains see table 5) for different frequencies.	37
43	Bode plot for both motors with same reduction ratio, PID-controlled.	38
44	Tracking performance of PID game controller with different derivative filters.	39
45	Command and behavior of Topy robot with P-controlled game controller.	40
46	Command and behavior of Topy robot with PID-controlled game controller.	40

47	Unity simulation test setup.	42
48	Command and feedback in Unity with P-controlled game controller (handheld).	43
49	Command and feedback in Unity with P-controlled game controller (wall-blocked).	44
50	Command and feedback in Unity with PID-controlled game controller (handheld).	44
51	Command and feedback in Unity with PID-controlled game controller (wall-blocked).	45
52	First draft of the yoke controller.	48
53	Identified operational range for the photoreceptors in the yoke controller.	49
54	3D model of the left-hand side controller with a removed cover.	49
55	3D printed yoke controller assembled and with cover removed.	50
56	Joystick mount for the yoke controller.	50
57	The rotation cam element (black-side view).	51
58	The pilot controller in use.	51
59	Tracking behavior of the P-controller ($K_P = 10\text{V/mm}$) for different frequencies.	52
60	Tracking performance for different reference signals with a $K_p = 5\text{V/mm}$	53
61	Tracking performance for different reference signals with a $K_p = 15\text{V/mm}$	53
62	Left-hand side, Motor reduction ratio 33:1.	54
63	Tracking behavior of the P-controller ($K_P = 10\text{V/mm}$) for 2Hz.	54
64	Indicated angles of palm pad with respect to spring plate to show the C-clamp effect.	55
65	The hysteresis effect for input-output tracking performance of different gains.	56
66	Command and behavior of Topy robot with P-controlled yoke controller.	58
67	Command and feedback in Unity with P-controlled ($K_P = 10\text{V/mm}$) yoke controller (handheld).	59
68	Unity test setup with C-clamp-blocked yoke controller.	60
69	Command and feedback in Unity with P-controlled yoke controller (blocked by C-clamp).	61

List of Tables

1	Performance requirements of the controller.	5
2	Identified operational range for the photoreceptors in the game controller.	14
3	Setup parameters.	17
4	Software parameters.	28
5	Trial and error PID tuning.	37
6	Latency table for sending joystick commands, current measured on the real robot, desired compression and measured compression. All values indicated in [s].	41
7	Controller performance requirements and achieved performances.	45
8	Latency table for sending joystick commands, current measured on the real robot, desired compression and measured compression. All values indicated in [s].	58
9	Controller performance requirements and achieved performances.	61

References

- [1] Asada. Study on pseudo-haptic device using tactile stimulation. Prethesis, 2016.
- [2] Oxford Online Dictionaries. Definition of haptics. <https://en.oxforddictionaries.com/definition/haptic>, July 2018.
- [3] Mandayam A Srinivasan. What is haptics? *Laboratory for Human and Machine Haptics: The Touch Lab, Massachusetts Institute of Technology*, pages 1–11, 1995.
- [4] Vincent Hayward, Oliver R Astley, Manuel Cruz-Hernandez, Danny Grant, and Gabriel Robles-De-La-Torre. Haptic interfaces and devices. *Sensor Review*, 24(1):16–29, 2004.
- [5] Richard J Adams, Manuel R Moreyra, and Blake Hannaford. Stability and performance of haptic displays: Theory and experiments. In *Proceedings ASME international mechanical engineering congress and exhibition*, pages 227–234, 1998.
- [6] Dale A Lawrence. Stability and transparency in bilateral teleoperation. *IEEE transactions on robotics and automation*, 9(5):624–637, 1993.
- [7] Septimiu E Salcudean, Ming Zhu, Wen-Hong Zhu, and Keyvan Hashtroodi-Zaad. Transparent bilateral teleoperation under position and rate control. *The International Journal of Robotics Research*, 19(12):1185–1202, 2000.
- [8] Göran Anders Viking Christiansson. *Hard master, soft slave haptic teleoperation*. PhD thesis, TU Delft, Delft University of Technology, 2007.
- [9] Nima Enayati, Elena De Momi, and Giancarlo Ferrigno. Haptics in robot-assisted surgery: challenges and benefits. *IEEE reviews in biomedical engineering*, 9:49–65, 2016.
- [10] Yamamoto A. Asada T., Nakamura T. Investigation on substitution of force feedback using pressure stimulation to palm. In *Haptics Symposium*, 2016.
- [11] Taku Nakamura, Shota Nemoto, Takumi Ito, and Akio Yamamoto. Substituted force feedback using palm pressurization for a handheld controller. In *International AsiaHaptics conference*, pages 197–199. Springer, 2016.
- [12] Panagiotis Agrafiotis, Anastasios Doulamis, George Athanasiou, and Angelos Amditis. Real time earthquake’s survivor detection using a miniaturized lwir camera. In *Proceedings of the 9th ACM International Conference on PErvasive Technologies Related to Assistive Environments*, page 21. ACM, 2016.
- [13] Mohamed Elgendi, Flavien Picon, Nadia Magnenat-Thalmann, and Derek Abbott. Arm movement speed assessment via a kinect camera: a preliminary study in healthy subjects. *Biomedical engineering online*, 13(1):88, 2014.
- [14] Linda van den Bedem, Ron Hendrix, Nick Rosielle, Maarten Steinbuch, and Henk Nijmeijer. Design of a minimally invasive surgical teleoperated master-slave system with haptic feedback. In *Mechatronics and Automation, 2009. ICMA 2009. International Conference on*, pages 60–65. IEEE, 2009.
- [15] Mahdi Tavakoli, RV Patel, and Mehrdad Moallem. Design issues in a haptics-based master-slave system for minimally invasive surgery. In *Robotics and Automation, 2004. Proceedings. ICRA’04. 2004 IEEE International Conference on*, volume 1, pages 371–376. IEEE, 2004.
- [16] Ilana Nisky, Assaf Pressman, Carla M Pugh, Ferdinando A Mussa-Ivaldi, and Amir Karniel. Perception and action in teleoperated needle insertion. *IEEE transactions on haptics*, 4(3):155–166, 2011.

- [17] Carlos Bermejo and Pan Hui. A survey on haptic technologies for mobile augmented reality. *arXiv preprint arXiv:1709.00698*, 2017.
- [18] Shoichi Hasegawa, Ishikawa Toshiaki, Naoki Hashimoto, Marc Salvati, Hironori Mitake, Yasuharu Koike, and Makoto Sato. Human-scale haptic interaction with a reactive virtual human in a real-time physics simulator. *Computers in Entertainment (CIE)*, 4(3):9, 2006.
- [19] Winfred Mugge, Irene A Kuling, Eli Brenner, and Jeroen BJ Smeets. Haptic guidance needs to be intuitive not just informative to improve human motor accuracy. *PloS one*, 11(3):e0150912, 2016.
- [20] Domenico Prattichizzo, Claudio Pacchierotti, and Giulio Rosati. Cutaneous force feedback as a sensory subtraction technique in haptics. *IEEE Transactions on Haptics*, 5(4):289–300, 2012.
- [21] Ryan E Schoonmaker and Caroline GL Cao. Vibrotactile force feedback system for minimally invasive surgical procedures. In *Systems, Man and Cybernetics, 2006. SMC'06. IEEE International Conference on*, volume 3, pages 2464–2469. IEEE, 2006.
- [22] Arash Ajoudani, Sasha B Godfrey, Matteo Bianchi, Manuel G Catalano, Giorgio Grioli, Nikos Tsagarakis, and Antonio Bicchi. Exploring teleimpedance and tactile feedback for intuitive control of the pisa/iit softhand. *IEEE transactions on haptics*, 7(2):203–215, 2014.
- [23] Jacques Foottit, Dave Brown, Stefan Marks, and Andy M Connor. An intuitive tangible game controller. In *Proceedings of the 2014 Conference on Interactive Entertainment*, pages 1–7. ACM, 2014.
- [24] Kouta Minamizawa, Souichiro Fukamachi, Hiroyuki Kajimoto, Naoki Kawakami, and Susumu Tachi. Gravity grabber: wearable haptic display to present virtual mass sensation. In *ACM SIGGRAPH 2007 emerging technologies*, page 8. ACM, 2007.
- [25] Gill A Pratt and Matthew M Williamson. Series elastic actuators. In *Intelligent Robots and Systems 95.'Human Robot Interaction and Cooperative Robots', Proceedings. 1995 IEEE/RSJ International Conference on*, volume 1, pages 399–406. IEEE, 1995.
- [26] Jerry E Pratt and Benjamin T Krupp. Series elastic actuators for legged robots. In *Unmanned Ground Vehicle Technology Vi*, volume 5422, pages 135–145. International Society for Optics and Photonics, 2004.
- [27] Arnaldo Gomes Leal Junior, Rafael Milanezi de Andrade, and Antônio Bento Filho. Series elastic actuator: Design, analysis and comparison. In *Recent Advances in Robotic Systems*. InTech, 2016.
- [28] Wilian M dos Santos and Adriano AG Siqueira. Impedance control of a rotary series elastic actuator for knee rehabilitation. *IFAC Proceedings Volumes*, 47(3):4801–4806, 2014.
- [29] E Basafa, M Sheikholeslami, A Mirbagheri, F Farahmand, and GR Vossoughi. Design and implementation of series elastic actuators for a haptic laparoscopic device. In *Engineering in Medicine and Biology Society, 2009. EMBC 2009. Annual International Conference of the IEEE*, pages 6054–6057. IEEE, 2009.
- [30] Jakob Oblak and Zlatko Matjačić. Design of a series visco-elastic actuator for multi-purpose rehabilitation haptic device. *Journal of neuroengineering and rehabilitation*, 8(1):3, 2011.
- [31] Ata Otaran, Ozan Tokatli, and Volkan Patoglu. Hands-on learning with a series elastic educational robot. In *International Conference on Human Haptic Sensing and Touch Enabled Computer Applications*, pages 3–16. Springer, 2016.

- [32] Katherine J Kuchenbecker, June Gyu Park, and Gunter Niemeyer. Characterizing the human wrist for improved haptic interaction. In *ASME 2003 International Mechanical Engineering Congress and Exposition*, pages 591–598. American Society of Mechanical Engineers, 2003.
- [33] Jaebum Park, Nemanja Pažin, Jason Friedman, Vladimir M Zatsiorsky, and Mark L Latash. Mechanical properties of the human hand digits: Age-related differences. *Clinical Biomechanics*, 29(2):129–137, 2014.
- [34] John E Speich, Liang Shao, and Michael Goldfarb. Modeling the human hand as it interacts with a telemanipulation system. *Mechatronics*, 15(9):1127–1142, 2005.
- [35] Ken Dutton, Steve Thompson, and Bill Barraclough. *The art of control engineering*. Addison Wesley Harlow, 1997.
- [36] Ben Fry and Casey Reas. Processing. <https://www.processing.org/>, July 2018.
- [37] exnumerus. How to fit a sinewave, an example in python. <http://exnumerus.blogspot.com/2010/04/how-to-fit-sine-wave-example-in-python.html>, April 2010.
- [38] Christopher C Ibeh. *Thermoplastic materials: properties, manufacturing methods, and applications*. CRC Press, 2011.